

THREE-DIMENSIONAL COMPUTATIONAL
MODELING AND SIMULATION OF CELL
ROLLING AND DEFORMATION ON AN
ADHESIVE SURFACE IN SHEAR FLOW

BY VIJAY PAPPU

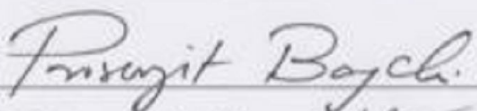
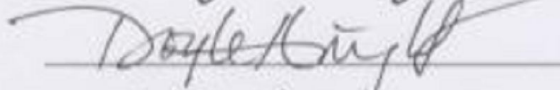
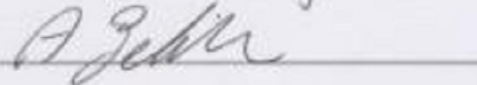
A thesis submitted to the
Graduate School—New Brunswick
Rutgers, The State University of New Jersey
in partial fulfillment of the requirements
for the degree of
Master of Science

Graduate Program in Mechanical and Aerospace Engineering

Written under the direction of

Prof. Prosenjit Bagchi

and approved by

New Brunswick, New Jersey

OCTOBER, 2008

ABSTRACT OF THE THESIS

Three-dimensional computational modeling and simulation of cell rolling and deformation on an adhesive surface in shear flow

by Vijay Pappu

Thesis Director: Prof. Prosenjit Bagchi

Three-dimensional computational modeling and simulations are presented on the rolling motion of a deformable cell on an adhesive surface in shear flow. The problem is motivated primarily by the adhesive rolling motion of white blood cells or leukocytes in response to inflammation in the body. The methodology is based on an immersed boundary method to predict cell deformation, and a Monte Carlo simulation to model the random formation and breakage of the adhesion bonds formed between a ligand-bearing cell and a receptor-coated surface. The multiscale and multiphysics modeling developed in this study allows us to resolve the complex coupling between the hydrodynamics, the deformation dynamics of

the cell, and the biophysics of the adhesion bonds. In the thesis, we address the sequence of events that are encountered in the multistep process of cell rolling, namely, the initial arrest of the cell, followed by its deformation and spreading on the substrate, and the subsequent quasi-steady rolling motion. We provide phase diagrams for cell adhesion/escape, and showed that the hydrodynamic lift, that exists on a deformable cell in the wall-bounded motion, plays a major role in the process. The experimentally observed ‘stop-and-go’ motion of the cells is predicted in our simulations. After providing results on the general adhesive rolling motion, we focus specifically on the rolling dynamics of the leukocytes, and study the effect of cell deformability, shear rate and cell concentration on the instantaneous and time-averaged rolling characteristics. We also study the biophysical characteristics of the adhesion bonds during the rolling process. Finally, we consider the effect of the adherent leukocytes on the surrounding flow in terms of the changes in tracer dispersion and the vascular flow resistance. Comparison with experimental measurements (in vitro and in vivo) is presented throughout the thesis.

Acknowledgements

Firstly, I would like to thank my advisor, Prof. Prosenjit Bagchi for his valuable guidance, support and encouragement throughout my Masters program. His teachings helped me gain a thorough understanding of concepts in theoretical and Computational Fluid Mechanics. He has been more than an advisor to me, guiding me through my obstacles and helping me stay focused on the work. His passion and dedication have helped to appreciate and develop interest in fluid mechanics. I would like to convey my gratitude to him for his excellent guidance.

Next, I would like to thank my family, especially my dad for his support and patience without which this would not have been possible today. His constant encouragement has helped me to overcome my lows and finish my study successfully.

Finally, I would like to thank all my friends at Rutgers University. In particular, I would like to thank my research group colleagues Kirit, Sai and Murthy for the valuable intellectual discussions, which helped me enormously. Further, I would also like to extend my thanks to Venkat, Pallab, Dhaval, Tushar, Jingru, Farnaz, Kellie and Megan for the enjoyable coffee breaks and the priceless lunch sessions.

Partial support from Busch grant from Rutgers University, funding from NSF

grant (BES-0603035), computational support from the National Center for Supercomputing Applications at Illinois and San Diego Supercomputing Center are also acknowledged.

Dedication

To my family

Table of Contents

Abstract	ii
Acknowledgements	iv
Dedication	vi
List of Tables	x
List of Figures	xi
1. Introduction	1
1.1. Blood	1
1.2. Leukocyte	1
1.3. Leukocyte Adhesion Cascade	3
1.4. Leukocyte Rolling Dynamics	4
1.5. Effect of Leukocyte Adhesion on Microcirculation	9
1.6. Challenges	11
1.7. Scope of the Thesis	11
2. Numerical Methodology	13
2.1. Flow Configuration and Simulation Technique	13
2.1.1. Problem setup	13

2.1.2.	Fluid-structure interaction	16
2.1.3.	Numerical treatment of membrane deformation	18
2.1.4.	Bond kinetics	19
2.1.5.	Random number generator	21
2.1.6.	Flow solver	22
2.1.7.	Interface tracking	23
2.1.8.	Dimensionless parameters	24
2.1.9.	Numerical resolution	25
2.2.	Validation	25
3.	Hydrodynamic Lift and Phase Diagram for Cell Capture/Escape	27
3.1.	Introduction	27
3.2.	Initial capture of a free-flowing cell	28
3.2.1.	Lateral migration and hydrodynamic lift	28
3.2.2.	Stochastic process in cell capture	33
3.2.3.	Phase diagram for cell capture/escape	44
3.2.4.	From capture to rolling	49
4.	Rolling Motion and Deformation of Leukocytes on Adhesive Sur-	
	faces in Simple Shear Flow	57
4.1.	Introduction	57
4.2.	Rolling dynamics	58
4.2.1.	Effect of nearby cells	70

4.3. Cell deformation	76
4.4. Biophysical Characteristics	80
4.4.1. Microvilli and bond dynamics	80
4.4.2. Effect of microvilli presentation	96
5. Effect of Leukocyte Adhesion on the Flow Pattern in Microves-	
sels	103
5.1. Introduction	103
5.1.1. Flow pattern	104
5.1.2. Flow resistance and fluid drag	107
6. Conclusions of Thesis and Directions of Future Work	119
6.1. Summary of the thesis	119
6.2. Future directions	123
References	125

List of Tables

2.1. Parameter values used in simulations.	20
--	----

List of Figures

1.1. Image showing a white blood cell (WBC) in an array of red blood cells (RBC). Image source: Leukocyte Adhesion Deficiency web-site.	2
1.2. Leukocyte Adhesion Cascade (LAC). The image shows steps involved in LAC: capture, rolling, slow rolling, firm adhesion, and transmigration. Image source: http://bme.virginia.edu/ley/ . . .	3
1.3. Experimentally observed ‘stop-and-go’ motion of three neutrophils rolling on P-selectin. Image Source: Schmidtke <i>et al.</i> [51].	5
1.4. (a) Schematic showing a rolling cell under the balance of the hydrodynamic force and the adhesive force of the bonds. (b) In-vitro side-view image of a neutrophil rolling on a P-selectin coated surface. (Dong <i>et al.</i> [12])	7
2.1. Three dimensional computational domain for simulation of adhesive rolling motion of deformable cells. The inset shows the schematic of one microvillus and selectin bonds.	14
2.2. (a) 3D cell showing the random distribution of the microvilli. (b) The log-normal distribution for assigning the initial unstretched lengths of microvilli.	15

2.3. The Eulerian and Lagrangian grids.	16
2.4. Sorting of random numbers into bins of 0.1.	22
2.5. Validation. Free-flowing velocity of a near-wall spherical cell as a function of shear rate. \square - Present results, — Goldman <i>et al.</i> [24].	26
3.1. Sequence showing the lateral migration of the cell in a linear shear flow. a) $Ca = 0.002$, b) $Ca = 0.2$. The flow is from left to right and $\dot{\gamma} = 370\text{s}^{-1}$. Here $t^* = t\dot{\gamma}$	30
3.2. Time variation of (a) lateral velocity, and (b) deformation index D , shown for varying $Ca = 0.02, 0.05, 0.1, 0.15$ and 0.2	32
3.3. Hydrodynamic drag ($-\diamond-$) and lift ($-\square-$) on a free-flowing cell as functions of Ca	34
3.4. Sequence showing the ‘capture’ of a free-flowing cell at $E_s = 0.3$ dyn/cm ($Ca = 0.02$). The flow is from left to right and $\dot{\gamma} = 370\text{s}^{-1}$.	35
3.5. Time history of axial velocity and number of bonds of the cell. The case is the same as shown in figure 3.4.	37
3.6. Sequence showing the ‘escape’ of a cell from the substrate. $\dot{\gamma} =$ 370s^{-1} , and $E_s = 0.03$ dyn/cm ($Ca = 0.2$). All biophysical param- eters are the same as in figure 3.4.	38
3.7. 2D slices showing the ‘tilting’ of the cell. a) $Ca = 0.002$, b) $Ca =$ 0.02 , c) $Ca = 0.2$	40

3.8.	(a) Axial displacement, and (b) axial velocity with time for ‘tilting’ cells upon initial arrest. The results are shown here for $Ca = 0.002$, and different ψ values as: — $\psi = 4$, — — — $\psi = 12$, — · — $\psi = 20$, — · — · $\psi = 80$, — — — — — $\psi = 200$	42
3.9.	Time T_s for the arrest of the cell as a function of (a) bond strength ψ for different Ca . — Δ — $Ca = 0.002$, — \diamond — $Ca = 0.02$, — \square — $Ca = 0.2$. (b) T_s as a function of Capillary number for different ψ . — \square — $\psi = 20$, — \diamond — $\psi = 40$, — Δ — $\psi = 80$	43
3.10.	Critical bond strength ψ_c for capture as a function of Ca for different capture probabilities P_c . — \square — ($\psi = \psi_L$) $P_c = 0\%$, — \circ — $P_c = 50\%$, — \diamond — ($\psi = \psi_U$) $P_c = 100\%$	45
3.11.	Phase diagram for cell capture/escape. Critical bond strength ψ_c as a function of Ca for different values of $\zeta = 0.1, 2.0$, and 5.0 . — \square — $P_c = 25\%$, — \diamond — $P_c = 75\%$. The lines are power fits through the data for each ζ	47
3.12.	Phase diagram for cell capture/escape. Critical bond strength ψ_c as a function of κ for $Ca = 0.2$. — \square — $P_c = 25\%$, — \diamond — $P_c = 75\%$	48
3.13.	Phase diagram for cell capture/escape. Critical bond strength ψ_c as a function of ζ for $\kappa = 0.5, 1$, and 10 . a) $Ca = 0.002$, b) $Ca = 0.2$. — \square — $P_c = 25\%$, — \diamond — $P_c = 75\%$	50

3.14. Time history of axial displacement and axial velocity of an adhesively rolling cell with $Ca = 0.002$ for different values of ψ . (a) $\psi = 90$, (b) $\psi = 440$. Also shown is the axial displacement and velocity of a free-flowing cell.	51
3.15. Time history of axial displacement and axial velocity of an adhesively rolling cell with $Ca = 0.02$ for different values of ψ . (a) $\psi = 220$, (b) $\psi = 370$. Also shown is the axial displacement and velocity of a free-flowing cell.	52
3.16. Average rolling velocity as a function of ψ for different Ca . $-\square-$ $Ca = 0.2$, $-\diamond-$ $Ca = 0.02$, $-\Delta-$ $Ca = 0.002$	53
3.17. Average rolling velocity as a function of ζ for different Ca . $-\square-$ $Ca = 0.002$, $-\diamond-$ $Ca = 0.02$, $-\Delta-$ $Ca = 0.2$	55
3.18. Maximum rolling velocity as a function of Ca	55
3.19. Qualitative phase diagram showing regions of escape, rolling and firm adhesion.	56
4.1. Sequence of a rolling leukocyte at $\dot{\gamma} = 500\text{s}^{-1}$ and $E_s = 2.6 \text{ dyn/cm}$. The shear flow, and the cell movement, are from left to right. The left panel shows sideview, and the right panel shows bottomview. Lagrangian mesh on the cell surface is also shown. In the bottomview, microvilli forming bonds are marked by numbers ‘1’, ‘2’ etc. The arrows indicate the location of tethering.	59

4.2.	Same as in figure 4.1 except $E_s = 0.3 \text{ dyn/cm}$. The arrows indicate the location of tethering.	61
4.3.	Rolling sequence at 100 s^{-1} shear rate and $E_s = 2.6 \text{ dyn/cm}$	62
4.4.	Rolling characteristics at $\dot{\gamma} = 100 \text{ s}^{-1}$, and $E_s = 2.6 \text{ dyn/cm}$. History of cell displacement (solid line) and instantaneous rolling velocity (dotted line). Also shown is the displacement(dashed line) of a free flowing cell under similar flowing environment.	63
4.5.	Effect of shear rate on the rolling dynamics. Axial displacement (left figure) and axial velocity (right figures) of a rolling leukocyte. A, B and C represent 100 s^{-1} , 300 s^{-1} , and 500 s^{-1} , respectively at a constant $E_s = 0.3 \text{ dyn/cm}$	65
4.6.	Effect of membrane stiffness on rolling dynamics. Axial displacement (left figure) and axial velocity (right figures) of a rolling leukocyte. A, B and C represent $E_s = 2.6, 0.9$, and 0.3 dyn/cm , respectively, at a constant $\dot{\gamma} = 500 \text{ s}^{-1}$	66
4.7.	Sideway (a) displacement and (b)velocity of a rolling leukocyte for $\dot{\gamma} = 500 \text{ s}^{-1}$, and $E_s = 2.6 \text{ dyn/cm}$. The case shown is the same as in figure 4.6A.	67
4.8.	Effect of membrane stiffness on the sideway motion at constant $\dot{\gamma} = 100 \text{ s}^{-1}$. (a) $E_s = 0.3 \text{ dyn/cm}$, (b) $E_s = 2.6 \text{ dyn/cm}$	69

4.9.	Average rolling velocity as a function of shear rate and membrane stiffness. Present results: $-\circ-$ $E_s = 0.3$, $-\Delta-$ $E_s = 0.9$, $-\diamond-$ $E_s = 2.6$ dyn/cm. Experimental results: - - - Kim & Sarelius [8]. . .	70
4.10.	(a) Average pause time, (b) Average step size as functions of shear rate and membrane stiffness. $-\diamond-$ $E_s = 2.6$, $-\Delta-$ $E_s = 0.9$, and $-\circ-$ $E_s = 0.3$ dyn/cm. \bullet represent in vitro data of Smith <i>et al.</i> [10].	71
4.11.	RMS velocity fluctuation of (a) axial and (b) sideways motion. $-\circ-$ $E_s = 0.3$, $-\Delta-$ $E_s = 0.9$, and $-\diamond-$ $E_s = 2.6$ dyn/cm.	72
4.12.	Effect of neighbouring cells on the rolling characteristics. Here $\dot{\gamma} = 300\text{s}^{-1}$ and $E_s = 2.6$ dyn/cm. Solid line: cell trajectory. Dotted line: instantaneous velocity. (a) 3 cells/100 μm , and (b) 6 cells/100 μm	74
4.13.	Same as figure 4.12 but $E_s = 0.3$ dyn/cm. (a) 1 cell/100 μm , and (b) 6 cells/100 μm	75
4.14.	(a) Average rolling velocity as obtained from the simulations as a function of number of adherent cells/100 micron and E_s . $-\circ-$ $E_s = 2.6$, $-\Delta-$ $E_s = 0.9$, and $-\diamond-$ $E_s = 0.3$ dyn/cm. In (b), symbols are the simulation results, and dash lines represent $V = A - B/r$ curves, where A and B are chosen to match the results (following King <i>et al.</i> [78]). The values are $A = 70, 25, 10$, and $B = 1300, 285, 100$, for $E_s = 2.6, 0.9, 0.3$ dyn/cm, respectively. . .	77

4.15. History of cell deformation index (L/H) (solid line) and contact area (dotted line) for a cell rolling at $\dot{\gamma} = 100\text{s}^{-1}$, and $E_s = 2.6$ dyn/cm. This case is the same as shown in figure 4.4.	79
4.16. Mean contact area and deformation index (L/H) as functions of shear rate and E_s . Solid lines with symbols are the present results: $-\circ-$ $E_s = 2.6$, $-\Delta-$ $E_s = 0.9$, and $-\diamond-$ $E_s = 0.3$ dyn/cm. Dash lines without symbols are in vivo measurements of Firrell & Lipowsky [22] (indicated by FL in the figure), and filled circles are computational results from Jadhav <i>et al.</i> [35] for $E_s = 0.3$ dyn/cm.	81
4.17. Effect of cell concentration on cell deformation for a cell with $E_s = 2.6$ dyn/cm. Solid line: contact area. Dotted line: deformation index. $\dot{\gamma} = 300\text{s}^{-1}$. (a) 3 cells/100 μm , and (b) 6 cells/100 μm . This cases are similar to that shown in figure 4.12.	82
4.18. Same as figure 4.17 but $E_s = 0.3$ dyn/cm. (a) 1 cell/100 μm , and (b) 6 cells/100 μm	83
4.19. Time-averaged contact area and deformation index (L/H) as functions of number of adherent cells/100 micron.	84
4.20. History of number of bonds (dotted line) and tethered microvilli (solid line). (a) $\dot{\gamma} = 100\text{s}^{-1}$, $E_s = 2.6$ dyn/cm, (b) $\dot{\gamma} = 100\text{s}^{-1}$, $E_s = 0.3$ dyn/cm, and (c) $\dot{\gamma} = 300\text{s}^{-1}$, $E_s = 0.3$ dyn/cm.	86

4.21. (a) Force history of a few microvilli, and (b) force history of a few bonds within a particular microvillus. In (a), microvilli are indicated by number '1', '2' etc. In (b) arrows indicate step increase in a bond force in response to breaking of another bond.	88
4.22. Average number of total bound microvilli (open bars) and tethered microvilli (solid bars) as functions of shear rate and cell compliance.	90
4.23. Average total bonds (solid lines) and stretched bonds (dash lines). -□- $E_s = 2.6$ and -○- $E_s = 0.3$ dyn/cm.	92
4.24. Average peak force on (A) microvilli and (B) bond. -□- $E_s = 2.6$ and -○- $E_s = 0.3$ dyn/cm.	94
4.25. Average total adhesion force as a function of shear rate for different membrane stiffness. -□- $E_s = 2.6$ and -○- $E_s = 0.3$ dyn/cm. . . .	95
4.26. (a) Distribution of adhesion force among all bound microvilli in the cell/substrate contact area, and (b) distribution of bound microvilli over the cell surface. The arrows indicate three microvilli forming tethers.	97
4.27. Effect of microvilli presentation on the average velocity as a function of (a) shear rate at a constant $E_s = 2.6$ dyn/cm, and (b) membrane stiffness at a constant shear rate of 300s^{-1} . — $N_{mv} = 21$, and - - - - $N_{mv} = 155$	99

4.28. Effect of microvilli presentation on step size as a function of (a) shear rate at a constant $E_s = 2.6$ dyn/cm, and (b) membrane stiffness at a constant shear rate of 300s^{-1} . — $N_{mv} = 21$, and - - - $N_{mv} = 155$	100
4.29. Effect of microvilli presentation on the RMS fluctuation of axial velocity as a function of (a) shear rate at a constant $E_s = 2.6$ dyn/cm, and (b) membrane stiffness at a constant shear rate of 300s^{-1} . — $N_{mv} = 21$, and - - - - $N_{mv} = 155$	101
5.1. Streamlines in $16\text{ }\mu\text{m}$ channel for (a) one and (b) six adherent cells per $100\text{ }\mu\text{m}$ channel length. Average deflection angle of tracers as a function of (c) channel height, (d) number of adherent cells and shear rate, and (e) E_s . In (c) two curves represent data obtained by considering all tracer particles in the whole vessel, and by considering those flowing through the mid-plane passing through the centers of the cells. In (d) two curves represent two different shear rates 100 and 500s^{-1}	106

- 5.2. Mean fluid velocity across the channel as a function of (A) number of adherent cells, (B) E_s , (C) shear rate, and (D) channel height. Dash line is the parabolic velocity in absence of the cells, and solid lines are the results with the cells. The arrows indicate the direction in which the relevant parameter increases. In (A) the number of cells increases as 1, 2.5, 5, 10 per 100 μm length in a 10 μm channel at 300s^{-1} shear rate and $E_s = 0.9 \text{ dyn/cm}$. In (B) E_s increases as 0.05, 0.15, 0.3, 0.9 dyn/cm in a 10 μm channel at 300s^{-1} shear rate. In (C) shear rate increases as 50, 100, 300, 500s^{-1} . In (D) channel height increases as 10, 16, and 25 μm . . . 108
- 5.3. Instantaneous fluid drag (dotted line, left axis), and relative flow resistance (solid line, right axis) for a representative case of 6 WBC/100 μm length of a 16 μm channel and $E_s = 2.6 \text{ dyn/cm}$. . 109

5.4. Relative resistance R_W/R_0 in 10, 16 and 25 μm channels for various number of adherent cells per 100 μm length. The solid line is the result from Chapman & Cokelet [69] (indicated by C & C here and in subsequent figures), the dash line is the in vivo result of House & Lipowsky [50] (indicated by H & L here and in subsequent figures). The symbols represent the present result. Multiple values of R_W/R_0 for a given number of adherent cells are due to the variation in shear rate, E_s and rolling velocity. Here R_W/R_0 is the ratio of the flow resistance with and without the adherent leukocytes. Data from all computation are shown to emphasize the recurring theme of the paper, that is, R_W/R_0 is dependent not only on the number of adherent cells, but also on shear rate, E_s and rolling velocity.	111
5.5. Effect of E_s , number of adherent cells, shear rate, and rolling velocity on R_W/R_0 . The channel height is 10 μm . Dash lines without symbols are results of Chapman & Cokelet. Lines with symbols are the present results.	113

5.6.	Same as in figure 5.5 but for 16 μm , and 25 μm channels. Dash lines and dash-dot lines without symbols are results of Chapman & Cokelet, and in vivo measurements of House & Lipowsky, respectively. Lines with symbols are the present results: $-\Delta-$ 1 WBC, $-\square-$ 3 WBC, $-\diamond-$ 6 WBC in 16 μm vessel, $-\nabla-$ 8 WBC, and $-X-$ 4 WBC in 25 μm vessel, per 100 μm length.	115
5.7.	Fluid drag as a function of E_s , shear rate and rolling velocity for different number of adherent cells in a 10 μm channel. $-\nabla-$ 1 WBC, $-\square-$ 5 WBC, and $-\diamond-$ 10 WBC per 100 μm length.	116

Chapter 1

Introduction

1.1 Blood

Blood is a multiphase suspension primarily consisting of red blood cells (erythrocytes), white blood cells (leukocytes), and platelets (thrombocytes). The blood cells are suspended in a liquid called plasma. The plasma mostly contains water and also has small quantities of dissolved proteins, glucose, mineral ions, hormones and carbon dioxide. By volume, the red blood cells constitute about 45% of whole blood, the plasma constitutes about 55%, and the white blood cells constitute a minute volume. The primary function of the erythrocytes is to carry oxygen, while that of the leukocytes is to take part in immune response. The platelets are responsible for blood clotting.

1.2 Leukocyte

The structure of a white blood cell (WBC) or leukocyte is made of three components, namely, a cortical membrane, a lobular segmented nucleus, and the cytoplasm. The cortical membrane comprises of a lipid bilayer with a supporting filamentous network called cytoskeleton. The nucleus can be either single-

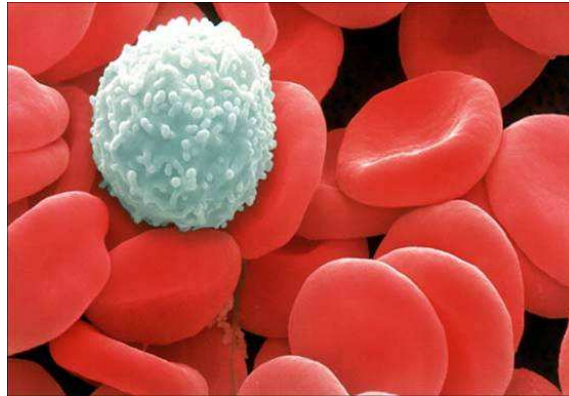


Figure 1.1: Image showing a white blood cell (WBC) in an array of red blood cells (RBC). Image source: Leukocyte Adhesion Deficiency website.

or multi-lobed. The cytoplasm is the predominant component of the cell and occupies about 80% of the total cell volume (Schmid-Schonbein *et al.* [1]). The constituents of the cytoplasm include water, granules, proteins, and solutes. Depending on the presence or absence of granules and the nuclei lobes, the leukocytes can be classified into neutrophils, eosinophils, basophils, lymphocytes, monocytes and macrophages.

A representative leukocyte is shown in figure 1.1. The protrusions on the surface of the leukocyte are called ‘microvilli’. The surface of the leukocyte is rough because the lipid bilayer has about 110% to 200% extra surface area stored in forms of ruffles and folds (Schmid-Schonbein *et al.* [1]; Lichtman and Kearney [2]; Evans and Kukan [3]; Ting-Beall *et al.* [4]). This excess area allows the leukocyte to undergo considerable deformation under an external force. In the undeformed state, the leukocyte is spherical in shape with a diameter of about 8 to 15 micron. The density of the cytoplasmic liquid of the leukocyte is similar

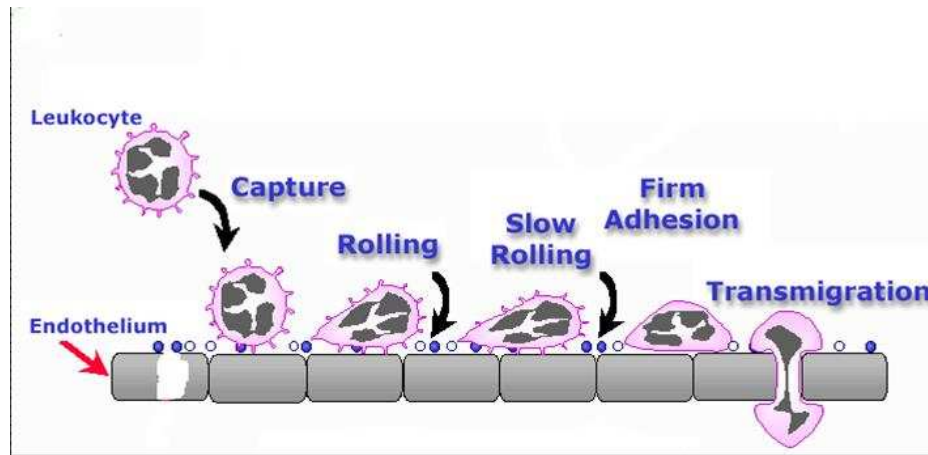


Figure 1.2: Leukocyte Adhesion Cascade (LAC). The image shows steps involved in LAC: capture, rolling, slow rolling, firm adhesion, and transmigration. Image source: <http://bme.virginia.edu/ley/>.

to that of the plasma (1.2 kg/m^3) while its viscosity is about 1000 times greater than the plasma viscosity ($\approx 1.2 \text{ cP}$).

1.3 Leukocyte Adhesion Cascade

Inflammation is a defense mechanism by the human body against a tissue damage or an injury. The primary objective of inflammation is to eradicate the irritant without spreading, and repair the surrounding tissue. One of the key inflammatory events includes leukocyte transmigration through the blood vessel walls, called vascular endothelium, and accumulation at the site of injury. This process, often called the Leukocyte Adhesion Cascade (figure 1.2), involves multiple steps that begin with the initial capture of the near-wall free-flowing leukocytes onto the endothelial walls, followed by the deformation and spreading of the leukocytes

on the substrate. The leukocytes then roll slowly on the wall, before they firmly adhere and transmigrate to the sites of inflammation.

The initial capture and rolling of the leukocytes onto the wall of a blood vessel are facilitated by a particular group of adhesion molecules called the ‘selectins’ (Lawrence & Springer [6]; Rinko *et al.* [7]; Kim & Sarelius [8]). Three common selectins that participate in leukocyte rolling are L-, P-, and E- selectins (Lawrence & Springer [6]; Alon *et al.* [9]). These selectins are distributed on the leukocyte surface and on the endothelium. The selectins bind to their counterparts called ‘ligands’ to form adhesive bonds. Ligands are also distributed over the cell surface and on the endothelium. P-selectin-glycoprotein ligand-1 (PSGL-1) is a common ligand that binds to all the three selectins. L-selectin and PSGL-1 molecules are expressed on leukocytes, whereas P-, and E-selectins are expressed on the activated endothelium. The selectin molecules have distinct but overlapping functions at each stage of leukocyte recruitment. L-selectin molecules are mainly involved in the initial capture of the leukocytes, while L-, P- and E-selectin molecules are involved in mediating cell rolling. Each of these stages is necessary for effective leukocyte recruitment.

1.4 Leukocyte Rolling Dynamics

After the initial capture and spreading of the cell on the substrate, the leukocyte rolls on the endothelial surface before transmigrating to the sites of inflammation. Rolling and adhesion of leukocytes require a balance of the hydrodynamic

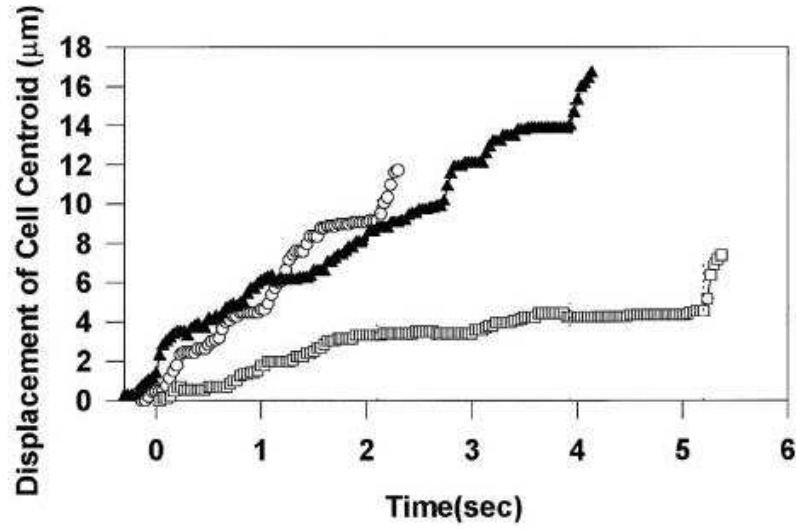


Figure 1.3: Experimentally observed ‘stop-and-go’ motion of three neutrophils rolling on P-selectin. Image Source: Schmidtke *et al.* [51].

dispersal force and the adhesion force between the cell and substrate. Generally, all the three selectin molecules (L-, P-, and E-) in coordination with their respective ligands, mediate cell rolling. Flow chamber studies have shown tethering and rolling of leukocytes over selectin-coated surfaces. The rolling phenomenon has been reconstituted in cell-free systems, where PSGL-1-bearing microspheres roll on P-selectin-coated substrates under dynamic flow conditions (Park *et al.* [11]; Yago *et al.* [13]; Rodgers *et al.* [15]). The ability of selectin-ligand pairs to mediate rolling interactions in shear flow is attributed to their fast association and dissociation rates. The selectin bonds form and break randomly. Analysis of leukocyte trajectory revealed that a rolling cell does not flow continuously, but rather moves in a ‘stop-and-go’ manner (Kim *et al.* [8]; Alon *et al.* [9]; Yago *et al.*

[13], Chen & Springer [14]) due to the random formation and breakage of receptor/ligand bonds. Cell motion is characterized by a series of steps during which the cell rolls, and pauses during which the cell is adherent (figure 1.3). L-selectin and PSGL-1 molecules are concentrated on the tips of microvilli which facilitate bond formation. Concentration of these molecules on the tips of microvilli suggests that the selectin bonds are likely to form in clusters, rather than distribute uniformly over the entire cell/substrate contact zone. Such a discrete distribution of adhesion molecules may also contribute to the ‘stop-and-go’ motion of leukocyte rolling.

The adhesive rolling motion of a leukocyte occurs under the balance of the hydrodynamic force acting on the cell, and the adhesive force of the bonds, as shown in the schematic in figure 1.4. Cell deformation may play a major role in the rolling process. While the circulating leukocytes maintain a spherical shape, adhesively rolling leukocytes are known to deform. In-vivo studies conducted by Damiano *et al.* [23], and in-vitro studies conducted by Dong *et al.* [12] showed that the rolling leukocytes deform into a ‘tear-drop’ shape (figure 1.4). The deformation is observed to increase with increasing shear rates. Cell deformation can stabilize cell rolling in several ways. The flat contact area upon initial capture allows the engagement of more microvilli. Adhesion via multiple microvilli would reduce the force on individual selectin bonds and prolong the bond lifetime. Cell deformation may also reduce the hydrodynamic drag, and hence the bond force. Recent experimental studies have indicated that leukocyte rolling

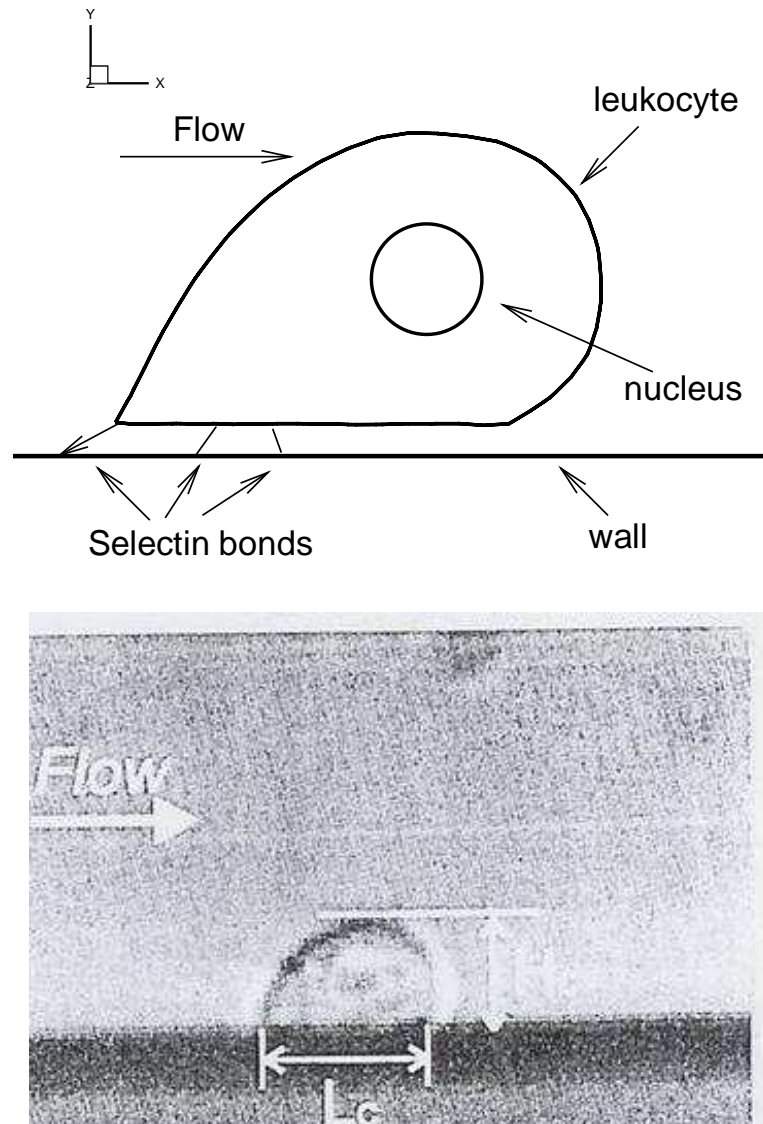


Figure 1.4: (a) Schematic showing a rolling cell under the balance of the hydrodynamic force and the adhesive force of the bonds. (b) In-vitro side-view image of a neutrophil rolling on a P-selectin coated surface. (Dong *et al.* [12])

is significantly slower and relatively smoother than that of microspheres coated with the same density of PSGL-1 molecules (Park *et al.* [11]; Yago *et al.* [13]). Also, formaldehyde-fixed neutrophils displayed reduced cell deformability and faster rolling on P-selectin-coated surfaces in shear flow compared to untreated neutrophils (Park *et al.* [11]). In contrast, increased neutrophil deformability resulted in decreased rolling velocities (McCarty *et al.* [18]).

Further, the microvilli, along with cell, are also known to elongate and form tethers during the rolling process. Schmidke and Diamond [51] performed high speed, high resolution videomicroscopy of flowing neutrophils interacting with P-selectin, and showed that thin membrane tethers were extracted from the cell surface during the rolling process. Shao *et al.* [53] conducted in-vitro studies on the deformation of microvilli under force and found that the microvillus can exist in two distinct regimes. Under small pulling forces, they behave as Hookean springs, while at higher forces, the cell membrane pulls away from the cytoskeleton allowing the microvilli to form long cylindrical membrane tethers with viscous properties. The microvilli elongation can be of the order of cell diameter. A long lever arm due to the microvillus elongation allows a greater component of bond force to resist the shear flow. Hence, the microvilli elongation is also hypothesized to further stabilize cell rolling.

Among several computational models, the adhesive dynamics simulation (ADS) pioneered by Hammer and co-workers made a significant contribution to the understanding of leukocyte rolling (Hammer *et al.* [25]; Chang *et al.* [26]; Chang

et al. [27]). In ADS, the leukocytes are modeled as rigid spheres, and the receptor/ligand interaction is simulated by stochastic Monte-Carlo simulation. Studies performed using ADS have facilitated in generating ‘state diagrams’, which show regions of firm adhesion, rolling adhesion and no adhesion. Recent works by the same group have incorporated microvilli deformation within the framework of ADS (Caputo & Hammer [29]), and showed that a minimum in rolling velocity occurs at an intermediate value of microvillus membrane viscosity. Deformation of an adherent leukocyte was considered in two-dimensions by Dong and co-investigators by modeling a leukocyte as a viscous liquid drop surrounded by an elastic ring (Dong *et al.* [12]; Dong & Lei [30]; Lei *et al.* [31]). N’Dri *et al.* [32] modeled leukocytes as 2D compound liquid drops to study the effect of cell nucleus on deformation. The role of viscoelasticity, and microvilli extension during leukocyte adhesion and rolling were considered in a recent 3D model developed by Khismatullin & Truskey [33,34]. Recently, Jadhav *et al.* [35] developed a 3D model for rolling leukocytes by coupling cell deformation with stochastic simulation of receptor/ligand interaction. Their model was able to replicate the ‘stop-and-go’ motion of leukocytes.

1.5 Effect of Leukocyte Adhesion on Microcirculation

Leukocyte adhesion to endothelium causes several changes in the local microvascular flow pattern (King *et al.* [74]; Thompson *et al.* [19]) . The protrusion of

an adherent leukocyte into the vascular lumen results into a decrease in the effective lumen area and leads to an increase in resistance to blood flow, and hence a decrease in volumetric blood flow rate. In vivo studies have shown significantly elevated flow resistance in post-capillary vessels due to adherent leukocytes. Using FMLP (formyl peptide)-mediated leukocyte-endothelium adhesion in cat mesentery, House & Lipowsky [50] observed up to 150% increase in flow resistance in vessels of 25 μm diameter. Adherent leukocytes also result in deflection of streamlines in microcirculation, and thus affect the flow of erythrocytes, platelets, and biomolecules in blood stream. King *et al.* [78] measured the deflection angle of tracer particles in presence of adherent leukocytes in vivo and showed that it increased with increasing leukocyte concentration. Reduced flow rate due to leukocyte adhesion may also lead to increased erythrocyte aggregation (Das *et al.* [16]).

Several investigators have developed theoretical models to predict the fluid drag on adherent leukocytes. Using a 2D model, Gaver & Kute [17] computed the fluid drag on a rigid hemisphere which served as a model for an adherent leukocyte, and showed that the fluid drag increased with decreasing vessel size. Brooks & Tozeren [63] considered 3D simulation of flow past an array of adherent cells which were modeled as rigid spheres, hemispheres, and inclined cones. The fluid drag was shown to decrease as the shape varied from a sphere to a cone. Their results, as well as those by Chapman & Cokelet [67-69], also showed that the fluid drag on individual cell decreased as the number of adherent leukocytes increased.

Reduction of the fluid drag acting on multiple adherent leukocytes in proximity has a significant bearing on the leukocyte rolling as the force exerted on each receptor/ligand bond is expected to decrease and the bond lifetime to increase which may result in smoother rolling of the cells. King *et al.* [78] have shown in vivo that the hydrodynamic interactions among nearby leukocytes affected the rolling velocity which decreased inversely with the cell-to-cell separation distance.

1.6 Challenges

Leukocyte rolling dynamics has been a subject of investigation in the past decade. The rolling adhesion involves a complex coupling between the bulk cell deformation (meso-scale), microvillus deformability (micro-scale), and receptor/ligand binding kinetics (nano-scale). Such a complex multiscale and multiphysics process makes it difficult for a theoretical analysis. As mentioned above, though several computational models have been developed to address this process, a complete 3D computational model which involves the cell deformation, the microvilli deformation, and the stochastic nature of bond formation is further needed. Such a tool would provide a detailed understanding of this complex, multiscale and multiphysics process.

1.7 Scope of the Thesis

The objective of this thesis is to develop computational models and simulations to investigate the adhesive rolling motion of the leukocytes. The framework is able to

consider a wide variety of problems, such as, the initial capture of the leukocytes onto the substrate, deformation and spreading of the leukocytes, and the effect of cell deformation and microvilli deformation on the rolling dynamics. In this thesis, we consider developing a fully three-dimensional computational method to address the multiscale and multiphysics process of cell rolling on adhesive surfaces in shear flow. The methodology is based on an immersed boundary method to predict cell deformation, and a stochastic Monte Carlo simulation to model the random formation and breaking of the adhesive bonds between the cell and the substrate. The computational methodology is presented in Chapter 2. Using the computational tool, we present the hydrodynamic lift and the phase diagram for the cell capture in Chapter 3. This is followed by a detailed discussion on the leukocyte rolling dynamics over adhesive surfaces in Chapter 4. The effect of rolling adhesion on the flow pattern is discussed in chapter 5. The conclusions and summary are given in Chapter 6.

Chapter 2

Numerical Methodology

2.1 Flow Configuration and Simulation Technique

2.1.1 Problem setup

We consider three-dimensional simulation of adhesive rolling motion of deformable cells (figure 2.1) in a channel. The channel is bounded by two infinite flat plates placed parallel to the X -axis in the XYZ coordinate system as shown. The height of the channel is H . In absence of the cells, the undisturbed flow \mathbf{u}_0 is either parabolic, driven by a constant pressure gradient dP/dX as

$$\mathbf{u}_0 = \left[\frac{1}{2\mu_0} \left(-\frac{dP}{dX} \right) (HY - Y^2) , \quad 0, \quad 0 \right], \quad (2.1)$$

or, a linear shear flow at zero pressure-gradient driven by the two walls of the channel as

$$\mathbf{u}_0 = [\dot{\gamma}Y, 0, 0], \quad (2.2)$$

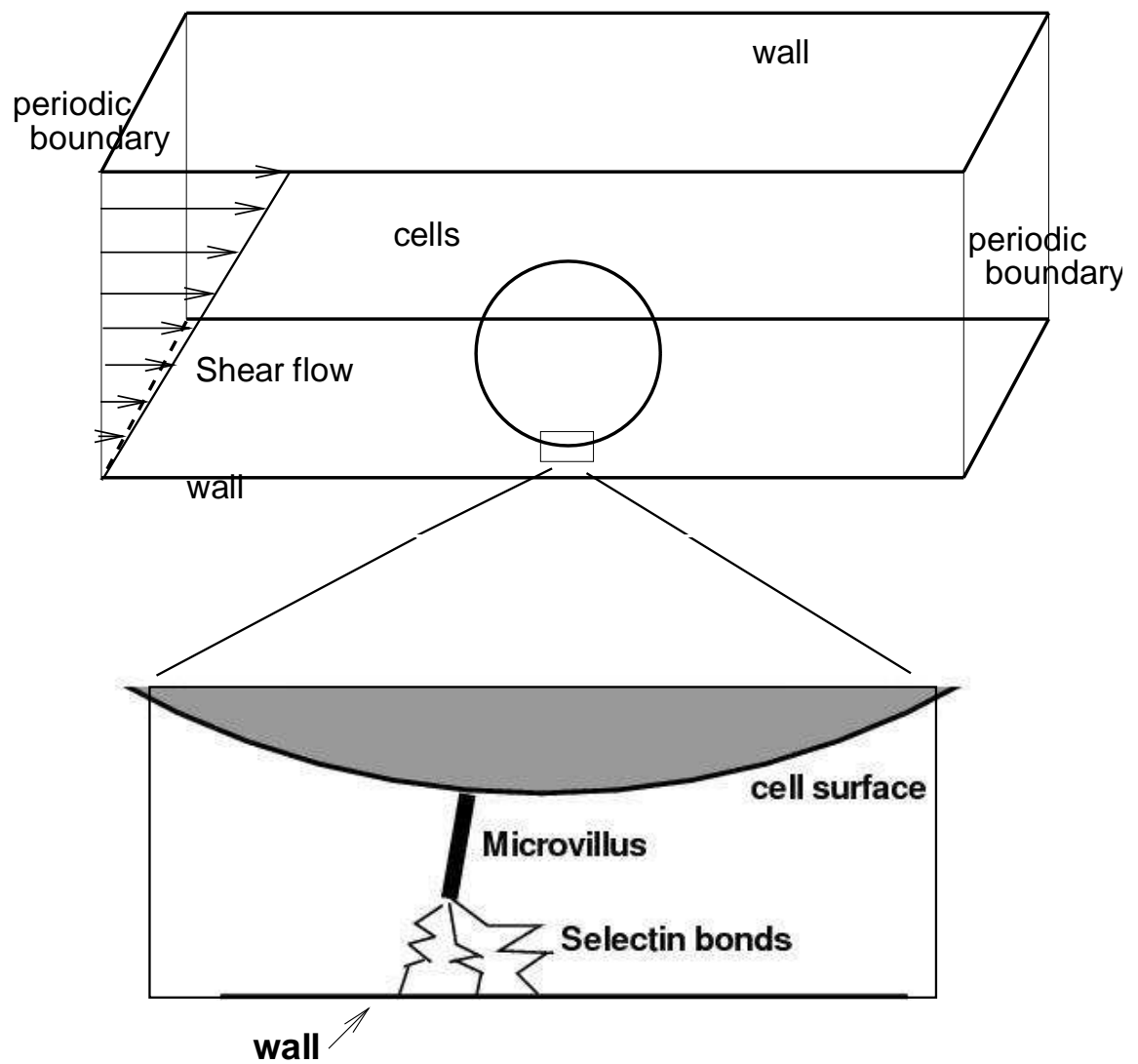


Figure 2.1: Three dimensional computational domain for simulation of adhesive rolling motion of deformable cells. The inset shows the schematic of one microvillus and selectin bonds.

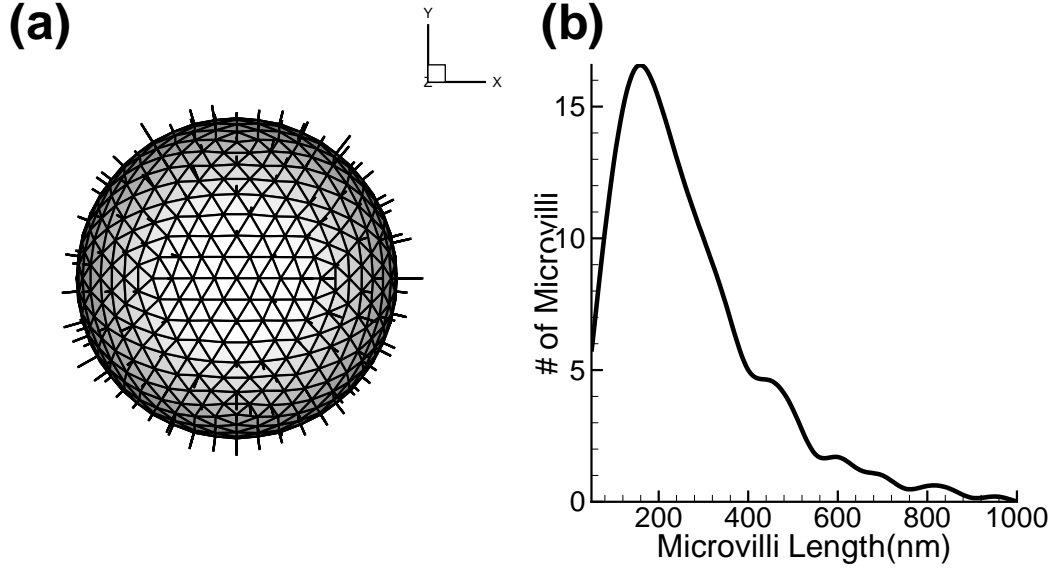


Figure 2.2: (a) 3D cell showing the random distribution of the microvilli. (b) The log-normal distribution for assigning the initial unstretched lengths of microvilli.

where $\dot{\gamma}$ is the shear rate. Here Z is the direction of vorticity of the undisturbed flow. The channel is assumed to be infinitely long in the X and Z directions. We use periodicity conditions in these directions to reduce the size of the computational domain. The initial shape of the cell is spherical with diameter $8 \mu\text{m}$. Microvilli are randomly distributed on the cell surface (figure 2.2a). Bonds are allowed to form in the microvilli tips (figure 2.1). We consider 3 different microvilli distributions, $N_{mv}=21, 155$ and 250 , where N_{mv} is the number of total microvilli. The initial unstretched lengths of the microvilli are assigned via 2 ways: all of them having uniform length of 350 nm , or through a log-normal (Bruehl *et al.* [20]) distribution as shown in figure 2.2b. The cells are released at $t = 0$ at $y_c/d = 0.66$, where y_c is the distance of the cell center from the wall.

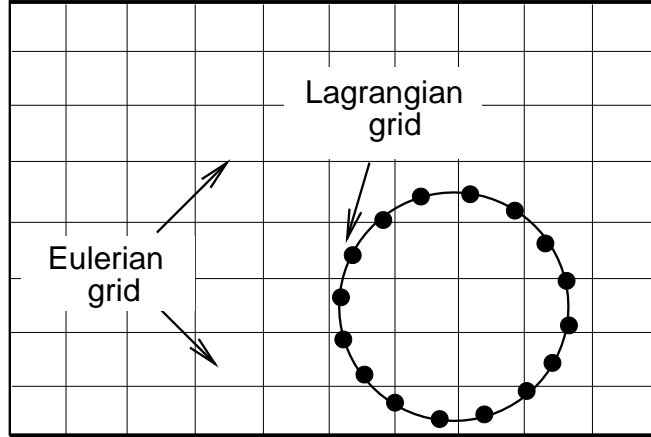


Figure 2.3: The Eulerian and Lagrangian grids.

2.1.2 Fluid-structure interaction

We model cells as capsules, that is liquid drops surrounded by infinitesimally thin elastic membranes. The simulation technique considered here is the front-tracking/immersed boundary method (Peskin *et al.* [37]; Tryggvason *et al.* [38]; Unverdi & Tryggvason [39]) for multiple fluids with different properties. The main idea of the front-tracking method is to use a single set of equations for both the fluids, inside and outside of the capsule. The fluid equations are solved on a fixed Eulerian grid, and the interface is tracked in a Lagrangian manner by a set of marker points (figure 2.3). The fluid motion is governed by the continuity and Navier-Stokes equations as:

$$\nabla \cdot \mathbf{u} = 0, \quad (2.3)$$

$$\rho \left[\frac{\partial \mathbf{u}}{\partial t} + \mathbf{u} \cdot \nabla \mathbf{u} \right] = -\nabla p + \nabla \cdot \mu (\nabla \mathbf{u} + (\nabla \mathbf{u})^T) \quad (2.4)$$

where \mathbf{u} is the fluid velocity, ρ is the density, p pressure, and μ is the viscosity. The cell surface is then recognized by a source-like term \mathbf{F} added to the r.h.s of equation 2.4. For a rolling cell in shear flow, the force on the cell surface can arise from two contributions: \mathbf{f}_e the elastic force due to cell deformation, and \mathbf{f}_a the adhesive force due to bond formation between the cell and the substrate. The source term \mathbf{F} is related to \mathbf{f}_e and \mathbf{f}_a as

$$\mathbf{F}(\mathbf{x}, t) = \int_{\partial S} [\mathbf{f}_e(\mathbf{x}', t) + \mathbf{f}_a(\mathbf{x}', t)] \delta(\mathbf{x} - \mathbf{x}') d\mathbf{x}'. \quad (2.5)$$

Here \mathbf{x} is a point in the flow domain, \mathbf{x}' is a point on the cell surface ∂S , and δ is the Delta function which vanishes everywhere except at the membrane. Models for computation of \mathbf{f}_e and \mathbf{f}_a are described later.

The δ function used in equation 2.5 is constructed by multiplying three 1D δ functions as

$$\delta(\mathbf{x} - \mathbf{x}') = \delta(x - x')\delta(y - y')\delta(z - z'). \quad (2.6)$$

For numerical implementation, a smooth representation of the δ -function is used as

$$\begin{aligned} D(\mathbf{x} - \mathbf{x}') &= \frac{1}{64\Delta^3} \prod_{i=1}^3 \left(1 + \cos \frac{\pi}{2\Delta} (x_i - x'_i) \right) \quad \text{for } |x_i - x'_i| \leq 2\Delta, \quad i = 1, 2, 3, \\ D(\mathbf{x} - \mathbf{x}') &= 0 \quad \text{otherwise,} \end{aligned} \quad (2.7)$$

where Δ is the Eulerian grid size (Unverdi & Tryggvason [39]). As a result, the membrane force varies smoothly over four Eulerian grid points surrounding the

interface. In discrete form, the integral in equation 2.5 can be written as

$$\mathbf{F}(\mathbf{x}_j) = \sum_i D(\mathbf{x}_j - \mathbf{x}'_i)(\mathbf{f}_a(\mathbf{x}'_i) + \mathbf{f}_e(\mathbf{x}'_i)) \quad (2.8)$$

where i and j represent Lagrangian and Eulerian points, respectively.

2.1.3 Numerical treatment of membrane deformation

The capsule membrane follows the neo-Hookean law for which the strain energy function is given by

$$W = \frac{E_s}{6}(\epsilon_1^2 + \epsilon_2^2 + \epsilon_1^{-2}\epsilon_2^{-2} - 3) \quad (2.9)$$

where ϵ_1 and ϵ_2 are the principal stretch ratios and E_s is the surface elastic modulus. We assume that the bending resistance of the membrane is negligible.

The deformation of the membrane is treated using a finite element model developed by Charrier *et al.* [43]; Shrivastava & Tang [44]), and later implemented by Eggleton & Popel [36] within the framework of immersed boundary method to consider large deformation of capsules. First, the membrane is discretized using flat triangular elements. The triangulated surface mesh needed for the simulations is obtained from the GNU Triangulated Surface (GTS) Library. GTS is an Open Source Free Software Library intended to provide a set of useful functions for scientists dealing with 3D computational surface meshes. The discretized surface for a sphere is shown in figure 2.2a. The main idea is that a general 3D deformation of the membrane can be reduced to a 2D problem by assuming that individual

triangular element on the membrane remains flat even after deformation. The forces acting on the three vertices of a triangular element are obtained by computing the displacements of the vertices of the deformed element with respect to the undeformed element. The details of the method can be found in Doddi [28] and Doddi & Bagchi [66].

2.1.4 Bond kinetics

Formation of receptor/ligand bonds between the cell and the substrate is simulated using stochastic Monte Carlo method (Hammer *et al.* [25]; Jadhav *et al.* [35]). Bonds are assumed to behave as stretched springs under force loading following a Hookean model [45]. The probability of formation of a new bond, and that of breakage of an existing bond, in a time interval Δt , are given by

$$P_f = 1 - \exp(-k_f \Delta t), \quad \text{and}, \quad (2.10)$$

$$P_r = 1 - \exp(-k_r \Delta t), \quad (2.11)$$

respectively, where k_f and k_r are the forward and reverse reaction rates which are computed as

$$k_f = k_f^0 \exp \left[-\frac{\sigma_{ts}(l - l_o)^2}{2K_B T} \right], \quad \text{and}, \quad (2.12)$$

$$k_r = k_r^0 \exp \left[\frac{(\sigma_b - \sigma_{ts})(l - l_o)^2}{2K_B T} \right], \quad (2.13)$$

Parameter	Value	Source
shear rate	$100 - 500\text{s}^{-1}$	
leukocyte diameter	$8\ \mu\text{m}$	
membrane stiffness (E_s)	$0.03 - 3.0\ \text{dyn/cm}$	[35]
number of microvillus (N_{mv})	21, 155, 250	[20] [21]
number of ligands	50/microvillus	[35]
receptor site density	$10 - 144/\mu\text{m}^2$	[10]
selectin bond length (l_0)	$0.1\mu\text{m}$	[58]
spring constant (σ_b)	$0.1 - 2.5\ \text{pN/nm}$	[58]
transition spring constant (σ_{ts})	$0.1 - 2.5\ \text{pN/nm}$	[10]
unstressed forward rate (k_f^0)	$2 - 200\text{s}^{-1}$	[59]
unstressed reverse rate (k_r^0)	$2 - 200\text{s}^{-1}$	[10]

Table 2.1: Parameter values used in simulations.

where k_f^0 and k_r^0 are the unstressed reaction rates, σ_b is the spring constant, σ_{ts} is the transition state spring constant, l and l_0 are the stretched and unstretched lengths of a bond, K_B is the Boltzmann constant, and T is the absolute temperature. Values of the parameters are given in Table 2.1. At a given time instance, two random numbers N_1 and N_2 , between 0 and 1, are generated. A new bond is allowed to form if $P_f > N_1$, and an existing bond is allowed to break if $P_r > N_2$ (Hammer *et al.* [25]; Jadhav *et al.* [35]). Force in each bond f_b is then obtained as

$$f_b = \sigma_b(l - l_0). \quad (2.14)$$

The adhesion force \mathbf{f}_a is the vector sum of the forces arising from all bonds formed in a microvillus tip.

2.1.5 Random number generator

The stochastic process requires the generation of random numbers to update the number of bonds after every time step. The random numbers are generated using a built-in random number generator in FORTRAN. The syntax for generating them is

$$\text{CALL SURAND/DURAND } (S, n, \mathbf{x})$$

where SURAND and DURAND generate short and long precision real random numbers respectively, S is the initial value used to generate the random numbers, n is the number of random numbers to be generated and \mathbf{x} is the vector of length n containing the random numbers between 0 and 1. These subroutines use the multiplicative congruential method to generate the random numbers with a user specified value of S . The value of S is specified between 1.0 and 2147483647.0.

Different sets of random numbers are generated for comparison with the forward and the reverse rate probabilities. The values of S for comparison with the forward rate probability are specified as functions of the number of ligands available on each microvillus. For comparison with the reverse rate probability, the random number is generated using the value of S specified as a function of number of bonds existing at that time step. As an illustration, a set of 50 random numbers between 0 and 1 are generated using the random number generator with a user defined $S = 500000$. The random numbers are then sorted out into bins of 0.1 as shown in figure 2.4. The unbiasedness of the random numbers is tested by performing the Chi-Square test which gives a value of 'p' = 0.69.

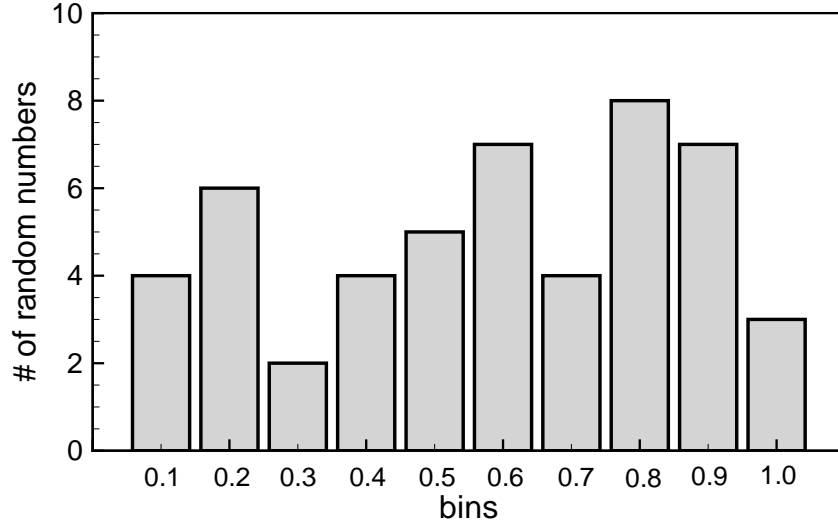


Figure 2.4: Sorting of random numbers into bins of 0.1.

2.1.6 Flow solver

The Navier-Stokes equations are discretized spatially using a second-order finite difference scheme, and temporally using a two-step time-split scheme. In this method the momentum equation is split into an advection–diffusion equation and a Poisson equation for the pressure. The body-force term is retained in the advection–diffusion equation. The nonlinear terms are treated explicitly using a second-order Adams–Bashforth scheme, and the viscous terms are treated semi-implicitly using the second-order Crank–Nicholson scheme. The resulting linear equations are inverted using an ADI (alternating direction implicit) scheme to yield a predicted velocity field. The Poisson equation is then solved to obtain pressure at the next time level. Using the new pressure, the velocity field is

corrected so that it satisfies the divergence-free condition. Details of the time-step scheme can be found in Doddi [28], and Bagchi & Doddi [66].

2.1.7 Interface tracking

The capsule membrane is tracked in a Lagrangian manner. After solving the Navier-Stokes equations, the velocity of the interface is computed at each time step, as

$$\mathbf{u}(\mathbf{x}') = \int_S \mathbf{u}(\mathbf{x}) \delta(\mathbf{x} - \mathbf{x}') d\mathbf{x}, \quad (2.15)$$

where S indicates the entire flow domain. Though the summation is over all Eulerian nodes, only the ‘local’ nodes contribute to the membrane velocity. The discrete form of the delta function used here is the same given by equation 2.6. In this way, a weighted interpolation of the Eulerian fluid velocity is performed which ensures that the continuity of velocity across the membrane is satisfied. The Lagrangian points on the membrane are then advected as

$$\frac{d\mathbf{x}'}{dt} = \mathbf{u}(\mathbf{x}'). \quad (2.16)$$

Numerically, the above equation is treated explicitly using the second-order Adams-Bashforth scheme as

$$\mathbf{x}'_{n+1} = \mathbf{x}'_n + \Delta t \left[\frac{3}{2} \mathbf{u}(\mathbf{x}'_n) - \frac{1}{2} \mathbf{u}(\mathbf{x}'_{n-1}) \right], \quad (2.17)$$

where $n, n + 1$, etc. are the time instances.

2.1.8 Dimensionless parameters

The shear rate of the undisturbed flow is given by $\dot{\gamma}$. The undeformed shape of the cell is spherical, and the diameter is denoted by d . The governing equations are made dimensionless using d as the characteristic length scale, $1/\dot{\gamma}$ as the time scale, and $\dot{\gamma}d$ as the velocity scale. The dimensionless time is denoted by t^* . The major dimensionless parameters are:

$$Ca = \mu\dot{\gamma}d/E_s, \quad (2.18)$$

$$\psi = \sigma_b l_0 / \rho \dot{\gamma}^2 d^4, \quad (2.19)$$

$$\zeta = (\sigma_b - \sigma_{ts})l_0^2 / 2K_B T, \quad \text{and}, \quad (2.20)$$

$$\kappa = k_f^0 / k_r^0 \quad (2.21)$$

Here, Ca is the ratio of the viscous force to the elastic force of the capsule membrane and gives a measure of cell deformability. ψ is the ratio of the adhesive force to viscous force and gives a measure of the bond strength. ζ is the the ratio of the elastic energy in the bond to thermal fluctuation energy and is an estimate of the inverse of bond lifetime. κ is the ratio of unstressed reaction rates and indicates the relative rate of bond formation. The inertia effect is considered small as the Reynolds number defined as $Re = \rho\dot{\gamma}d^2/\mu \approx 0(10^{-2})$.

2.1.9 Numerical resolution

Typical Eulerian resolution used in this study is $40 \times 40 \times 40$ to $80 \times 80 \times 80$, and Lagrangian resolution used is 1280–5120 triangular elements. Dimensionless timestep used in the simulation is 10^{-3} .

2.2 Validation

A detailed validation of the immersed boundary method, in the context of capsule deformation, is provided in Doddi [28], and Doddi & Bagchi [66]. Here we provide further validation of the free motion of a sphere near a plane wall in a linear shear flow. We release a spherical capsule of diameter $8 \mu\text{m}$ and high membrane stiffness of 3.0 dyn/cm near the planar wall at different shear rates. At steady state, the capsule flows at a height of $6.5 \mu\text{m}$ from the wall with a velocity which varies linearly with shear rate from $301 \mu\text{m/s}$ at 100s^{-1} to $1194 \mu\text{m/s}$ at 400s^{-1} . We compare our results with theoretical expressions provided by Goldman *et al.* [24], who calculated the velocity of a ‘hard’ sphere moving near a wall in a linear shear flow. The simulation results differ from the theoretical values within a range of 1.3% to 7.7%.

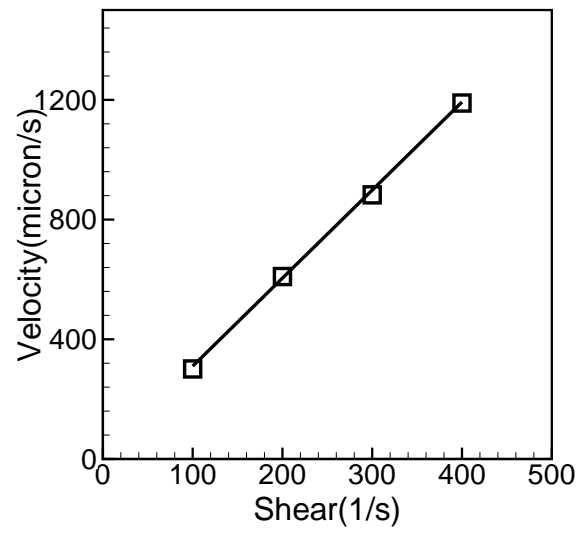


Figure 2.5: Validation. Free-flowing velocity of a near-wall spherical cell as a function of shear rate. \square - Present results, — Goldman *et al.* [24].

Chapter 3

Hydrodynamic Lift and Phase Diagram for Cell Capture/Escape

3.1 Introduction

As described in Chapter 1, the initial events in the inflammatory response by a leukocyte involve the following steps: 1) capture of a near-wall free-flowing leukocyte onto the wall of a blood vessel by the adhesive bonds (P-, E-, and L-selectins), 2) deformation and spreading of the leukocyte on the substrate, and 3) slow rolling motion of the leukocyte over the substrate in a ‘stop-and-go’ manner. These events involve a complex coupling between the hydrodynamics, the deformation dynamics of a cell, and the biophysics of the selectin bond kinetics. We use the numerical tool developed in Chapter 2 towards a detailed understanding of such a complex, multiscale and multiphysics process. In doing so, we choose a parametric space that is much broader than that relevant for leukocytes. As such, the results presented below are valid for various other particles (e.g. removal of adhered liquid drops and contaminants from a wall), and various other biological cells (e.g. stem cells and cancer cells) where deformation and receptor/ligand-like binding dictate the adhesive motion.

In the subsequent sections, we serially address the sequence of rolling events as mentioned above, namely 1) capture, 2) spreading, and 3) rolling.

3.2 Initial capture of a free-flowing cell

3.2.1 Lateral migration and hydrodynamic lift

We consider the near-wall motion of an initially spherical cell in a linear shear flow ($\mathbf{U} = \{\dot{\gamma}y, 0, 0\}$) as shown in the schematic given in figure 2.1. The typical shear rate $\dot{\gamma} = 370\text{s}^{-1}$, and the leukocyte diameter $d = 8\text{ }\mu\text{m}$. The Reynolds number $Re = \rho\dot{\gamma}d^2/\mu \approx 0(10^{-2})$; hence the effect of inertia can be neglected.

We release the cell at $t = 0$ at $y_c/d = 0.66$, where y_c is the distance of the cell center from the wall. In general, the force exerted by the fluid on a particle can be decomposed into two parts: a drag which is parallel to the wall (and hence, the undisturbed flow), and a lift which is perpendicular to the wall. As per the theory of viscous flows [48], the lift on a non-deformable spherical particle is zero in the absence of inertia. Thus, such a particle would move axially parallel to the wall for all time. This is essentially due to the linearity of the Stokes flow. If the particle is deformable, however, a hydrodynamic lift results due to the non-linearity of the kinematic condition at the fluid/particle interface. The lift then propels the particle away from the wall, and the particle is said to undergo a ‘lateral migration’. Such lateral migration has been observed experimentally and predicted numerically for liquid drops, and the red blood cells which are extremely deformable particles.

We hypothesize that the hydrodynamic lift plays a major role in the initial capture of a cell onto an adhesive surface. In order for a cell to adhere, the force of adhesion must overcome the lift. To elucidate the role of the hydrodynamic lift, we first consider a set of simulations where the lateral migration of a free-flowing deformable cell is considered. We define the deformability of the cell in terms of the Capillary number Ca given as $Ca = \mu\dot{\gamma}d/E_s$. The near-wall motion of the cell obtained from our simulations is shown in figure 3.1 for two different Ca of 0.002 and 0.2 at $\dot{\gamma} = 370\text{s}^{-1}$ using a few snapshots (top view and side view). With time, the cell moves axially in the flow direction, as well as laterally away from the wall. For $Ca = 0.002$, due to a higher membrane stiffness, the cell mostly maintains its spherical shape as seen in figures 3.1a and b.

Figures 3.1c and d show a similar sequence for a more deformable cell of $Ca = 0.2$. After the cell is released in the flow, it deforms very quickly (within $t^* < 1$, as shown) under the action of the imposed shear, and aligns itself at an angle with the direction of the flow. A higher curvature in the wall-facing part of the cell develops immediately after the release rendering an asymmetrical shape. But soon after, the cell attains a nearly ellipsoidal shape. Also shown is the top-view (figure 3.1d) which suggests that the cell shape is oblate spheroid, with the expanse in z -direction remaining unchanged during its evolution. Figure 3.1 suggests that the rate of deformation is significant during the initial transience. Once this initial transience is passed, the capsule shape, and its orientation with respect to the flow direction remain nearly steady as it migrates away from the

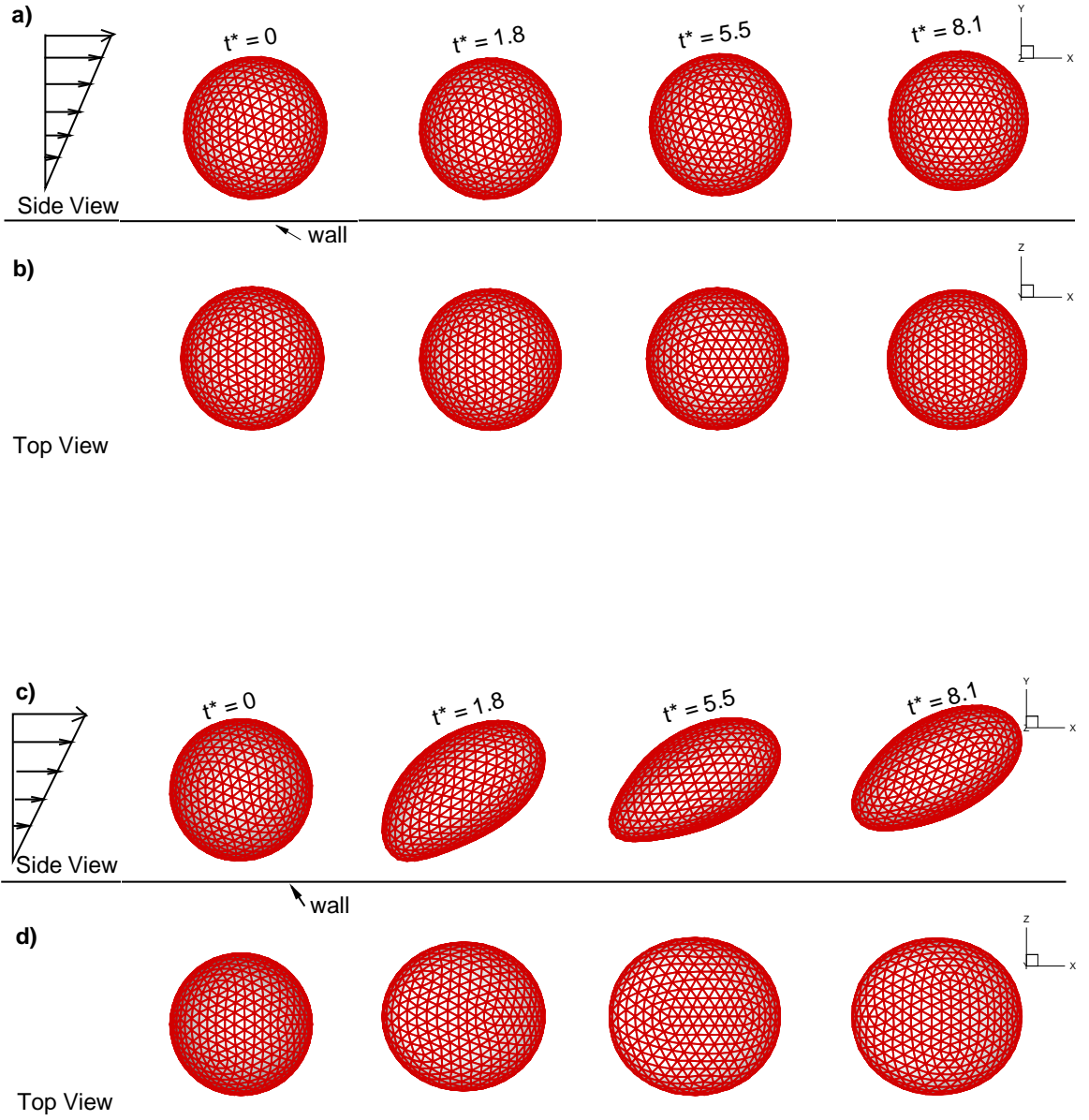


Figure 3.1: Sequence showing the lateral migration of the cell in a linear shear flow. a) $Ca = 0.002$, b) $Ca = 0.2$. The flow is from left to right and $\dot{\gamma} = 370\text{s}^{-1}$. Here $t^* = t\dot{\gamma}$.

wall. Thus the lateral migration process can be said to be quasi-steady. The quasi-steady nature of the capsule migration can be understood by comparing the characteristic migration time $T_y = d/V_y$, to the response time of the capsule shape $T_c = \mu d/E_s$. The capillary number Ca can be expressed as the ratio of T_c and the axial convection time $T_x = d/V_x$. Typically, $V_y \ll V_x$, hence $T_x/T_y \ll 1$. Since $Ca < 1$, we see that $T_c \ll T_y$. A detailed numerical study of such quasi-steady migration is presented in Doddi & Bagchi [66].

Analysis of several Ca cases suggests that the cell migrates continually away from the wall. In figure 3.2, we show the history of lateral velocity V_y and an instantaneous deformation index D . The index D is calculated as $(L_{\max} - L_{\perp})/(L_{\max} + L_{\perp})$ where L_{\max} is the maximum distance between two points on the capsule profile on (x, y) -plane passing through its centroid, and L_{\perp} is the distance between capsule membrane in the direction normal to L_{\max} in the same plane. For an ellipsoidal capsule, L_{\max} is the major axis, and L_{\perp} is the minor axis. As the flow starts, D attains its peak value within a short time implying that the capsule deforms quickly before it moves significantly in the lateral direction. The migration velocity V_y also reaches its maximum during the rapid initial transience. Subsequently, both V_y and D decrease very slowly which further illustrates the quasi-steady nature of the migration process. The slow decrease in V_y and D after attaining the maximum is due to the reduction in the wall effects as the capsule moves away. It is also noted in figures 3.2a and b that V_y and D are higher for higher Ca .

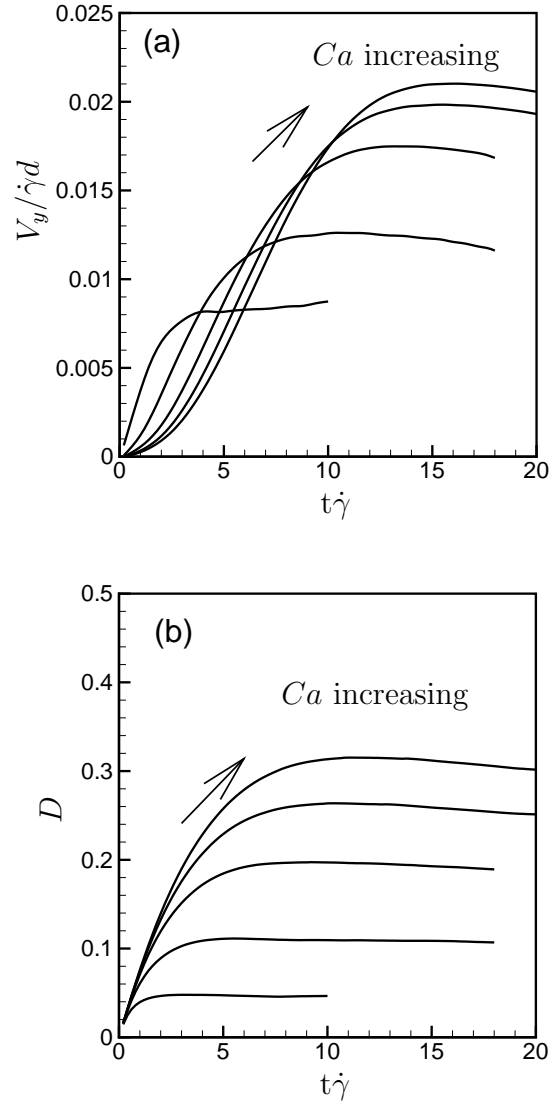


Figure 3.2: Time variation of (a) lateral velocity, and (b) deformation index D , shown for varying $Ca = 0.02, 0.05, 0.1, 0.15$ and 0.2 .

In order for a cell to get arrested onto the substrate, the adhesion force of a bond must balance the hydrodynamic lift. The lift can be estimated from the migration velocity by the use of the Stokes law $F = 3\pi d\mu(U - V)$ where U is the undisturbed fluid velocity at the instantaneous location of the cell centroid, and V is the cell velocity. We note that this relation is valid for a rigid spherical particle. Mathematical relations exist in the literature for the Stokes drag on ellipsoidal particles. We have verified, using our simulations, that for the shapes shown in figure 3.1, these improved relations do not predict significantly different hydrodynamic forces than those predicted by the Stokes law for spherical particles. Then, the lift becomes $F_L = 3\pi d\mu V_y$, which is shown in figure 3.3 in dimensionless form $(F_L/\dot{\gamma}d^2\mu)$, and as a function of Ca . The data in this figure correspond to the maximum of the numerically obtained lift. The hydrodynamic lift increases with increasing Ca . Also shown is the drag F_D as a function of Ca obtained using the slip velocity as $F_D = 3\pi d\mu|U - V|$. Unlike the lift, the drag decreases with increasing Ca , as the slip velocity reduces and the cell becomes more ‘streamlined’.

3.2.2 Stochastic process in cell capture

In normal flow conditions, the leukocytes are deformable in nature. The hydrodynamic lift on the leukocytes is non-zero, and hence causes them to migrate away from the surface. Adhesion occurs under a balance of the hydrodynamic lift force arising from the deformability of the cell, and the adhesive force between the cell and the wall. In order to initiate the capture of a flowing cell, the cell

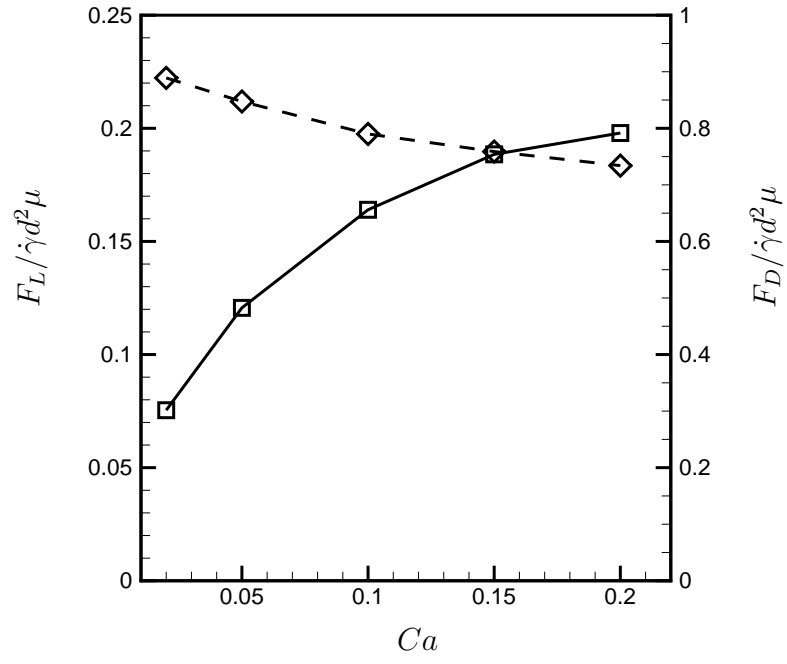


Figure 3.3: Hydrodynamic drag ($-\diamond-$) and lift ($-\square-$) on a free-flowing cell as functions of Ca .

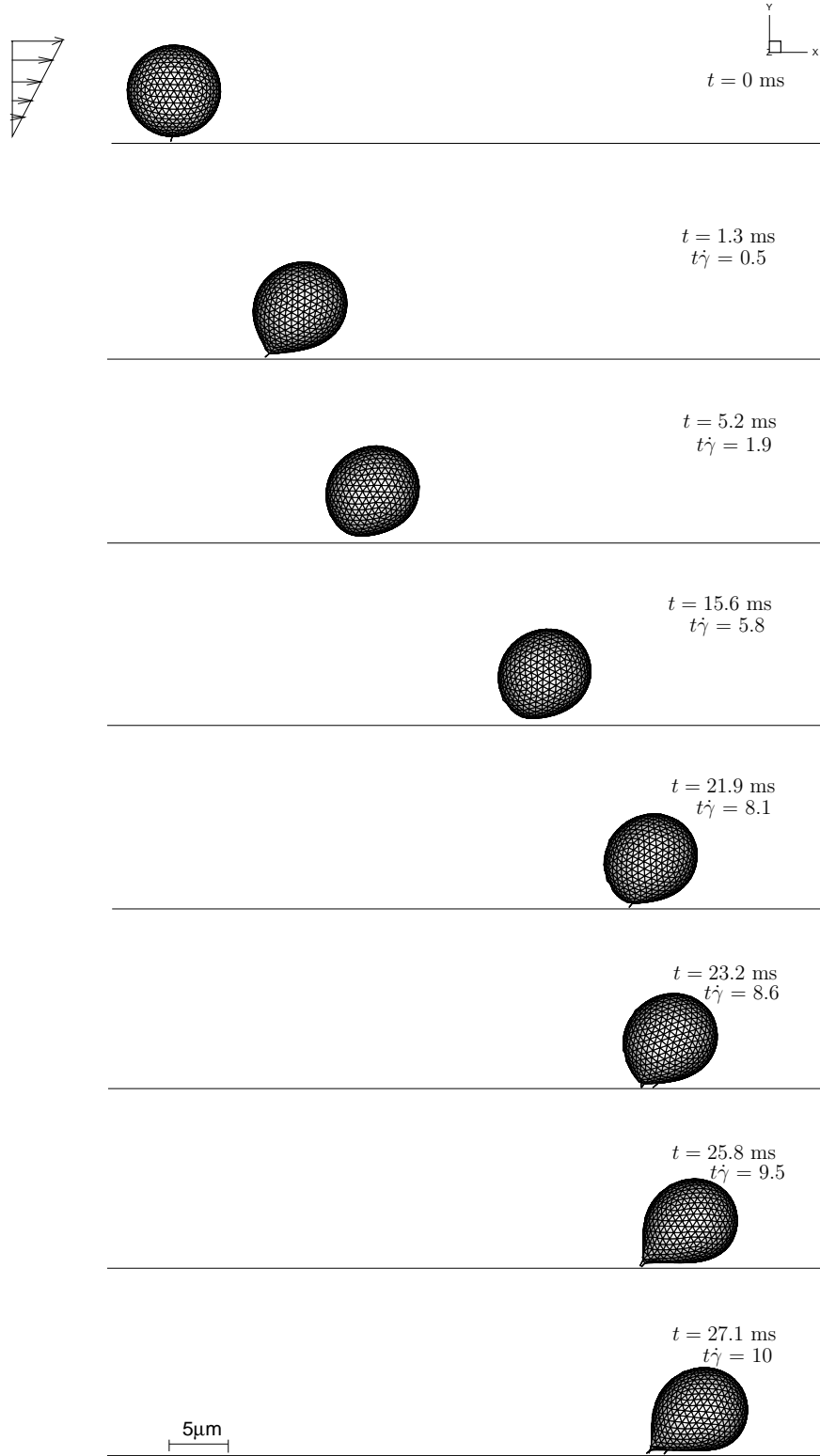


Figure 3.4: Sequence showing the ‘capture’ of a free-flowing cell at $E_s = 0.3$ dyn/cm ($Ca = 0.02$). The flow is from left to right and $\dot{\gamma} = 370\text{s}^{-1}$.

surface must be close enough to the receptor-coated surface. Further, the chemical reaction between the ligands and the receptors must be fast enough so that a bond can be formed before the cell can ‘escape’. Thus one can expect a complex relationship between cell deformability, bond strength, and bond lifetime that determines the arrest of a flowing cell. Once the cell is arrested, it either rolls slowly over the surface in a quasi-steady manner, or firmly adheres, or may detach from the surface, depending on the balance of the hydrodynamic lift, adhesion force, and bond lifetime.

We now turn on the receptor/ligand interaction kinetics in our model, and repeat the simulations of cell motion to study the initial capture events. Figure 3.4 shows the sequence of the capture of a free-flowing cell with $Ca = 0.02$. The time history of dimensionless axial velocity and the number of bonds is shown for the same case in figure 3.5. Also shown is the axial velocity of a free-flowing cell. At $t\dot{\gamma} = 0$, the cell forms one bond with the surface and its velocity temporarily reduces to 0.36 (figure 3.5) from the velocity of the free-flowing cell (≈ 0.6). The cell quickly deforms, forms a cusp in its rear end, and rotates clockwise due to the fluid torque. Due to the stochastic nature of the process, and the high fluid force, at $t\dot{\gamma} = 1.0$, the bond breaks, causing the cell to resume its motion. The cell drifts away from the wall due to the hydrodynamic lift, and the rear-end cusp is smoothed out. The cell continues to form very short-lived bonds due to the stochastic process, and the cell velocity fluctuates with time as seen in figure 3.5. For $t\dot{\gamma} > 8$, multiple bonds form, and the cell velocity drops significantly. Further

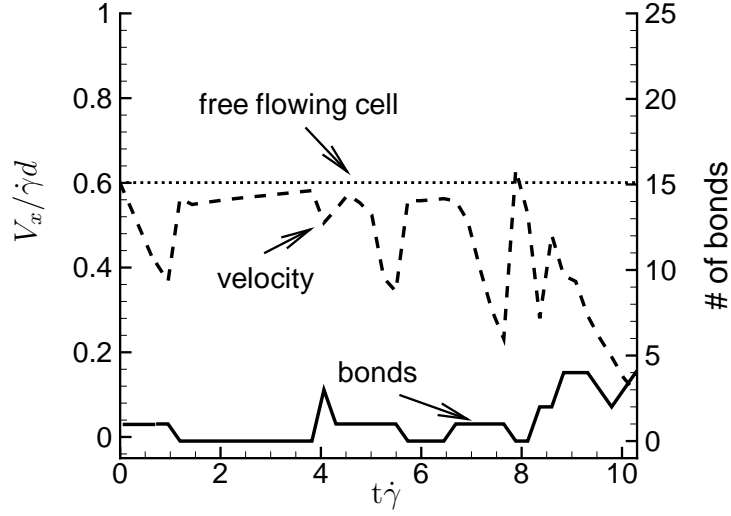


Figure 3.5: Time history of axial velocity and number of bonds of the cell. The case is the same as shown in figure 3.4.

continuation of the simulation showed that the cell no longer can leave the wall.

Another example is shown in figure 3.6 where a more deformable cell at $E_s = 0.03$ dyn/cm ($Ca = 0.2$) is considered. All other biophysical parameters remain the same as shown in figure 3.4. After the release, due to higher Ca , the cell deforms more in this case. Formation of a bond results in the development of a sharp cusp near the rear-end of the cell. The rear-end elongates further and the cell tilts clockwise due to hydrodynamic torque. However, due to the stochastic nature of the process, the bond breaks at $t = 16.8$ ms ($t\dot{\gamma} = 6.2$). Since the cell is more deformable, the higher hydrodynamic lift causes a significant ‘stretching’ of the bond and hence accelerates the bond breakage. Once the bond breaks, the higher lift force propels the cell quickly away from the wall preventing any further receptor/ligand interaction and hence new bond formation.

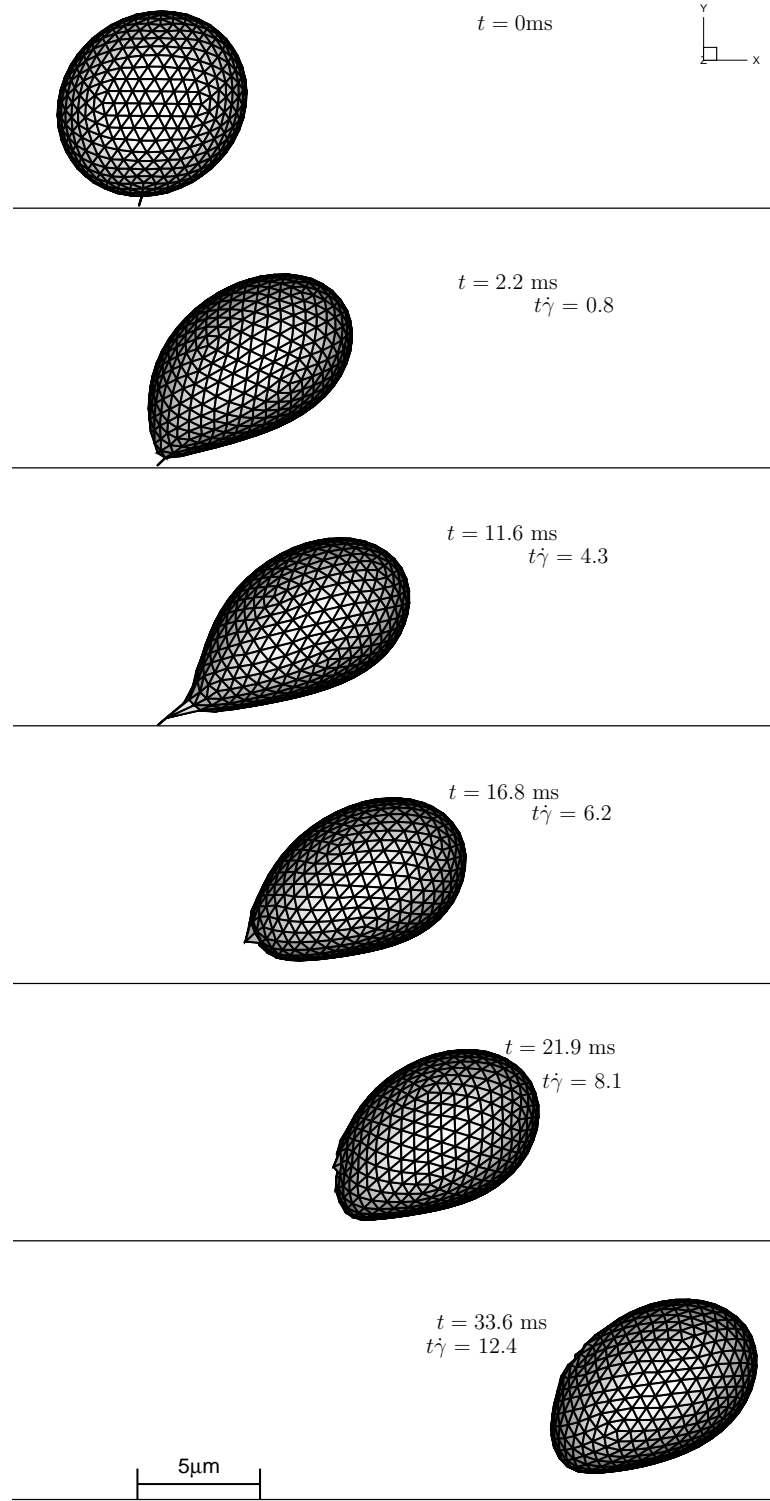


Figure 3.6: Sequence showing the ‘escape’ of a cell from the substrate. $\dot{\gamma} = 370\text{s}^{-1}$, and $E_s = 0.03\text{ dyn/cm}$ ($Ca = 0.2$). All biophysical parameters are the same as in figure 3.4.

In order for a cell to arrest onto the surface, the bond should sustain until the cell deforms, rotates and flattens onto the surface. The bond strength should also be high enough to balance the hydrodynamic force on the cell. Figures 3.4 and 3.6 suggest the coupling between the hydrodynamic lift, lifetime of a bond, and the cell deformability. The hydrodynamic shear causes the cell to first elongate roughly along the extensional direction of the flow. The initial bond acts like an ‘anchor’. The non-zero hydrodynamic torque about this anchor results in the clockwise tilting of the cell. As the cell tilts, interaction with the wall makes a flat contact area, which then facilitates formation of more bonds, and eventual capture of the cell. If the initial bond breaks before the cell flattens onto the substrate, the cell will ‘escape’ provided the hydrodynamic lift is sufficiently high. Thus the life-time of the bond must be greater than the time taken by the cell to ‘tilt’ i.e., to make a finite contact area with the substrate. We now present the results on the ‘tilting’ of the cell onto the substrate upon the initial bond formation.

To facilitate the study of cell tilting we consider $k_f^0 \gg k_r^0$ in this set of numerical experiments, so that the initial bond has an infinite lifetime. Under this condition, the equation for the reverse reaction becomes irrelevant, and the only two parameters that determine the process are the Capillary number Ca and the dimensionless bond strength ψ ($\psi = \sigma_b l_0 / \rho \dot{\gamma}^2 d^4$). Figure 3.7 shows the 2D slices of the cell shapes during cell tilting for three cases, $Ca = 0.002, 0.02, 0.2$, and a constant $\psi = 200$. The slices are shown at equal time intervals of $t\dot{\gamma} = 0.24$. The hydrodynamic force acting on the cell is transmitted to the bond causing the latter

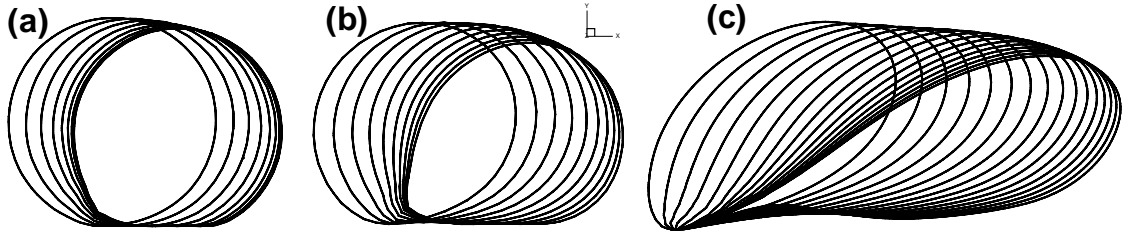


Figure 3.7: 2D slices showing the ‘tilting’ of the cell. a) $Ca = 0.002$, b) $Ca = 0.02$, c) $Ca = 0.2$.

to stretch. As the bond stretches, the cell motion is prevented due to the adhesion force. The cell translates, and the adhesion force increases until the horizontal component of the adhesion force is sufficient to balance the hydrodynamic drag acting on the cell. At this time, the forward motion of the cell stops. The cell then starts tilting clockwise towards the surface under the hydrodynamic torque. Eventually a steady state is reached when the cell surface in proximity of the bottom wall creates a flat contact area. A lubrication layer exists between the cell and the bottom plate. The vertical component of the adhesion force balances the hydrodynamic lift and the lubrication pressure. The contact area increases with increasing Ca . For all Ca , the final steady shape shows that the cell is tilted in the flow direction. For $Ca = 0.2$, the cell shape resembles a ‘tear-drop’ shape. Note that even at $Ca = 0.002$, for which virtually no deformation is expected for a free-flowing cell, the adherent cell shows significant deformation which is primarily caused by the wall (or, the lubrication pressure).

Numerical experiments have been performed for a wide range of dimensionless bond strength ψ from $O(1)$ to $O(10^2)$, and Ca from 0.002 to 0.2. Figure 3.8 shows

the axial (x) displacement and velocity of the cell center with time for various ψ , while Ca is kept constant at 0.002. The figure shows that the cell gradually slows down and comes to a rest under the action of the adhesion force.

As mentioned before, it is of interest to estimate the time T_s taken by the cell to flatten onto the surface and reach a steady state. Figure 3.9a shows the time T_s as a function of the dimensionless bond strength ψ for different Ca . The time T_s is calculated from figure 3.8 by noting the time when the fractional change in the x -displacement over a unit dimensionless time $t\dot{\gamma}$ first becomes less than 1%. As seen in figure 3.9a, the time T_s decreases very rapidly with increasing ψ for small values of ψ , but then becomes nearly constant for larger ψ . At lower values of ψ the cell takes longer time to come to rest due to larger elongation of the bond. At higher ψ , bond elongation is less and the time T_s is determined by Ca alone. Further, the time T_s as a function of Ca for various dimensionless bond strengths ψ is shown in figure 3.9b. Here T_s appears to vary linearly with Ca with two different slopes for $Ca < 0.1$ and $Ca > 0.1$. The explanation of such linear variation is not clear to us; however, the reason for the increased slope at higher Ca can be explained using the results on the hydrodynamic lift. The more deformable a cell is, the higher is the hydrodynamic lift that propels the cell rapidly away from the wall. Hence, when arrested, a deformable cell would require longer time to settle onto the surface.

These results depict that it is ‘easier’ to capture a rigid cell than a deformable cell due to higher hydrodynamic lift, and hence larger tilting time T_s . The lifetime

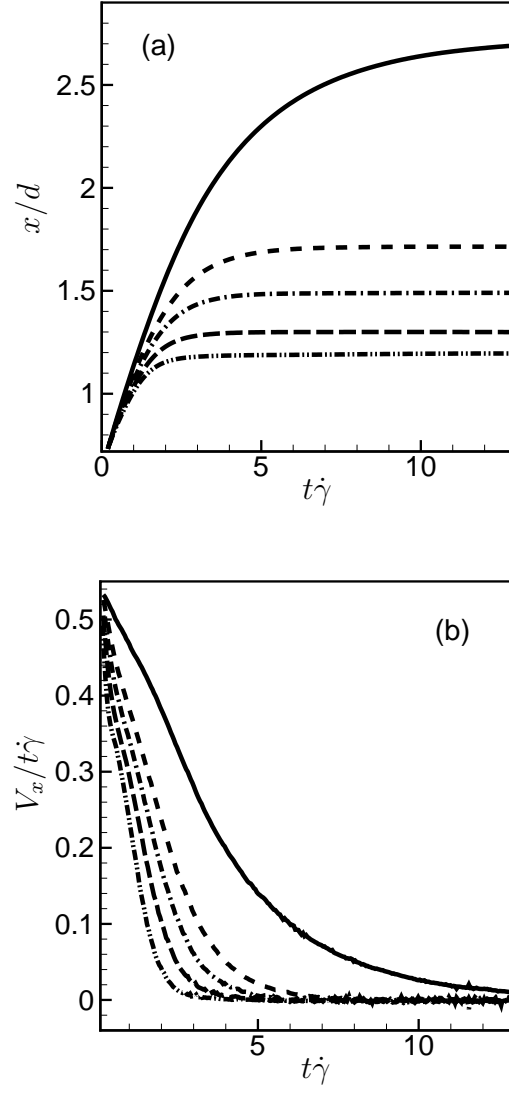


Figure 3.8: (a) Axial displacement, and (b) axial velocity with time for ‘tilting’ cells upon initial arrest. The results are shown here for $Ca = 0.002$, and different ψ values as: — $\psi = 4$, - - - - $\psi = 12$, - · - · - $\psi = 20$, - · - - · - $\psi = 80$, - - - - - $\psi = 200$.

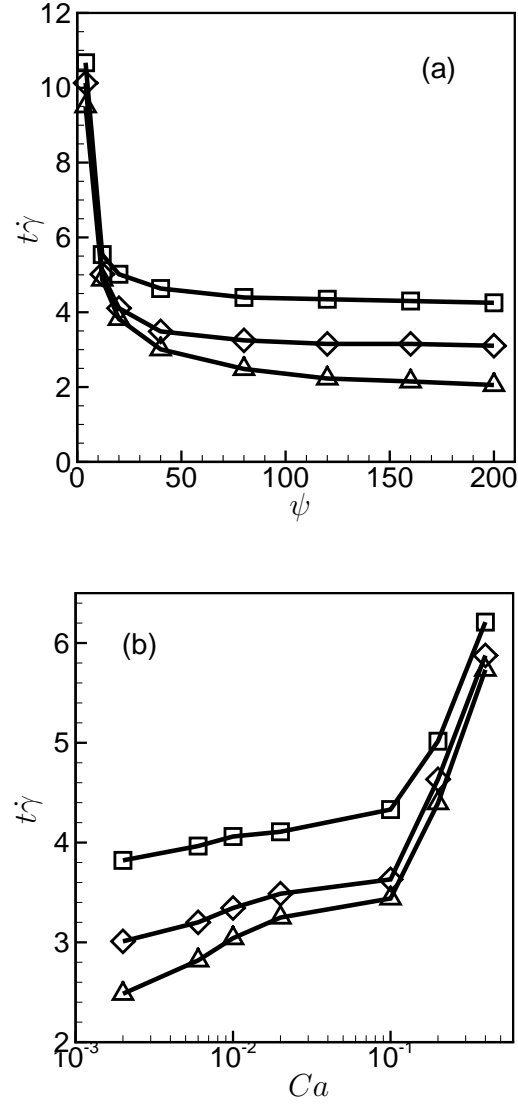


Figure 3.9: Time T_s for the arrest of the cell as a function of (a) bond strength ψ for different Ca . $-\Delta-$ $Ca = 0.002$, $-\diamond-$ $Ca = 0.02$, $-\square-$ $Ca = 0.2$. (b) T_s as a function of Capillary number for different ψ . $-\square-$ $\psi = 20$, $-\diamond-$ $\psi = 40$, $-\Delta-$ $\psi = 80$.

of the initial bond T_b must be greater than T_s for the cell to be captured.

3.2.3 Phase diagram for cell capture/escape

We have, so far demonstrated that the binding/unbinding of a near-wall free-flowing cell onto an adhesive substrate depends on a complex relation between cell deformability, and the biophysical properties of the receptor/ligand kinetics. We have performed extensive numerical experiments by varying cell deformability and receptor/ligand properties over a wide range. These results allow us to generate ‘phase diagrams’ that can serve as maps for cell capture/escape. Recall that the four major non-dimensional parameters are: the Capillary number $Ca = \mu\dot{\gamma}d/E_s$, the dimensionless bond strength $\psi = \sigma_b l_0 / \rho \dot{\gamma}^2 d^4$, $\zeta = (\sigma_b - \sigma_{ts}) l_0^2 / 2K_B T$ which is an estimate of the inverse of bond lifetime, and $\kappa = k_f^0 / k_r^0$, which is the ratio of unstressed reaction rates. In the phase diagram, we present ‘critical bond strength’ ψ_c , that would be required to capture a cell onto the substrate, as a function of Ca , ζ , and κ . Since the process is stochastic, a single numerical experiment for specific parametric values of ψ , Ca , ζ , and κ may not tell us about the nature of cell capture/escape. Thus, we perform N number of simulations for a given parametric set of Ca , ζ , ψ , and κ , and observe if the cell is captured or not. If the cell is captured for N_c number of times, we say that the probability of capture is $P_c = (N_c/N) \times 100\%$. As an illustration, consider three different cells with $Ca = 0.002, 0.02$ and 0.2 as shown in figure 3.10. We keep ζ and κ fixed at 0.5 and 1 , respectively. We perform $N = 4$ simulations for varying bond strength

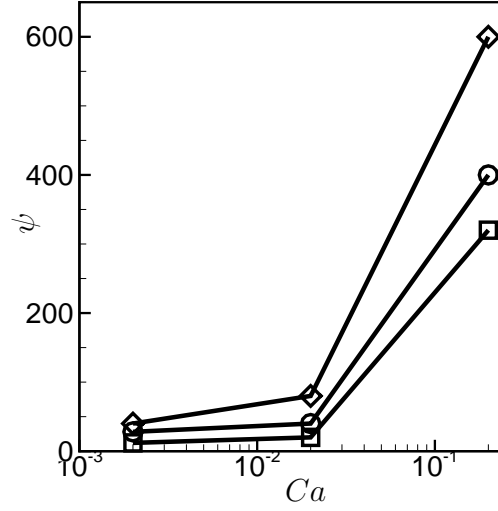


Figure 3.10: Critical bond strength ψ_c for capture as a function of Ca for different capture probabilities P_c . $-\square-$ ($\psi = \psi_L$) $P_c = 0\%$, $-\circ-$ $P_c = 50\%$, $-\diamond-$ ($\psi = \psi_U$) $P_c = 100\%$.

ψ as $\psi_L \leq \psi \leq \psi_U$ in steps of $\Delta\psi = (\psi_U - \psi_L) / 3$. Here ψ_L is the lower limit of the bond strength for which none of the experiments resulted in cell capture; thus $P_c = 0\%$. On the other hand, ψ_U is the upper limit of ψ for which all of the experiments resulted in cell capture; hence $P_c = 100\%$. For $\psi_L < \psi < \psi_U$, P_c would lie between 0 and 100%. Figure 3.10 shows the critical bond strength ψ_c as a function of Ca for $P_c = 0, 50$ and 100% . Higher the critical bond strength ψ_c , higher is the probability P_c of capture. In the phase diagrams presented below, we show the data for $P_c = 25\%$ and 75% .

Figure 3.11 shows the critical bond strength ψ_c at $P_c = 25\%$ and 75% as a function of Ca for different ζ values of 0.1, 2.0 and 5.0 for a constant $\kappa = 1$. The critical bond strength shows a non-linear increase with Ca . This is due to the higher hydrodynamic lift on a more deformable cell. This confirms our previous

conclusion that a less deformable cell is easier to capture onto a substrate than a more deformable cell. Note that the hydrodynamic drag decreases, but the lift increases, as Ca increases (figure 3.3). The fact that ψ_c increases with Ca also confirms our hypothesis that the hydrodynamic lift plays a more critical role in cell capture/escape than the drag.

Earlier in figure 3.3, it was shown that the lift F_L asymptotes with increasing Ca . In contrast, the critical bond strength ψ_c increases with faster rate with increasing Ca . There seems to be an apparent contradiction since the adhesion force should balance the hydrodynamic force (F_H), and both are expected to have a similar trend with respect to Ca . This apparent contradiction can be explained as follows. The force exerted on the bond is higher for higher Ca due to the higher hydrodynamic lift. For a weak bond (low σ_b and hence low ψ), such a high force causes a significant stretching of the bond (since $\sigma_b(l - l_0) \approx F_L$). Since $k_r \sim \exp[\zeta(l/l_0 - 1)^2]$, a higher stretching would cause k_r to shoot, and hence the bond would break before the cell can be captured. In contrast, for a strong bond (σ_b and ψ are high) the bond stretching is not very significant, and k_r does not shoot. Then, the bond can survive longer ($T_b > T_s$) than the time needed for the cell to flatten onto the substrate. It was shown earlier that T_s increases rapidly with increasing Ca for $Ca > 0.1$. Thus T_b needs to be sufficiently high; this requirement can be met only when ψ_c (and hence σ_b) is high. Thus while F_L saturates with increasing Ca , ψ_c rapidly grows due to the exponential dependence of k_r on $(l - l_0)^2$.

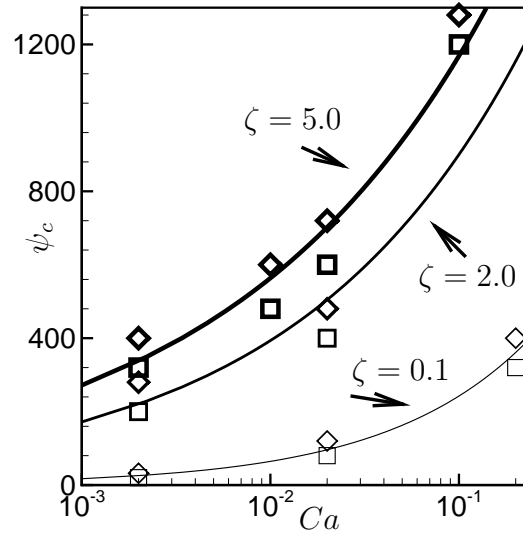


Figure 3.11: Phase diagram for cell capture/escape. Critical bond strength ψ_c as a function of Ca for different values of $\zeta = 0.1, 2.0$, and 5.0 . $-\square-$ $P_c = 25\%$, $-\diamond-$ $P_c = 75\%$. The lines are power fits through the data for each ζ .

Figure 3.11 also suggests the role of ζ in the capture/escape process. The critical bond strength ψ_c increases with increasing ζ . The arguments just given above can be used to explain this trend. As noted before, $1/\zeta$ is an estimate of the lifetime of a bond (T_b), since the reverse reaction rate $k_r \sim \exp[\zeta(l/l_0 - 1)^2]$. At higher ζ , the cell can be captured only if ψ_c is high enough so that $(l/l_0 - 1)^2$ is small, and k_r does not shoot up. This analysis brings out the importance of inclusion of the bond stretching in the study of adhesive motion. If the adhesive force were modeled simply by using a force potential that does not consider bond breakage due to stretching, it would not be possible to predict the rapid growth of ψ_c at higher Ca .

Figure 3.12 shows the variation in the critical bond strength with κ for a

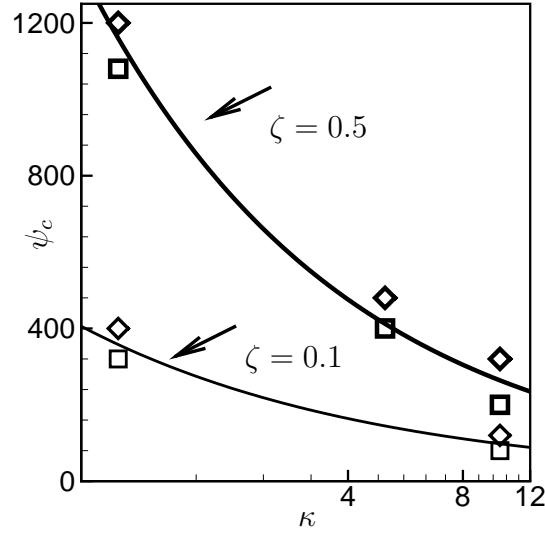


Figure 3.12: Phase diagram for cell capture/escape. Critical bond strength ψ_c as a function of κ for $Ca = 0.2$. $-\square-$ $P_c = 25\%$, $-\diamond-$ $P_c = 75\%$.

deformable cell of $Ca = 0.2$. Results for two values of $\zeta = 0.1$ and $\zeta = 0.5$ are shown here. The relative rate of bond formation increases with increasing values of κ . Thus, at high κ , multiple bonds are present. Hence, a smaller bond strength is sufficient to capture the cell at higher values of κ as seen in the figure. At lower values of ζ , the critical bond strength is weakly dependent on κ . This suggests that for more deformable cells, prolonged bond lifetime has a significantly greater importance on the capture of the cell.

Coupling between κ and ζ is discussed in figure 3.13 which shows ψ_c as a function of ζ for several values of κ for a rigid cell ($Ca = 0.002$) and a deformable cell ($Ca = 0.2$). Since a high value of κ implies the presence of multiple bonds, the cell may be captured even with a high value of ζ in such cases. Hence at high κ , ψ_c has a weak dependence on ζ . In contrast, ψ_c increases rapidly with

increasing ζ at low κ . The non-linear dependence of ψ_c on ζ is more prominent for the deformable cell for the reasons described above.

3.2.4 From capture to rolling

Now we continue the simulations beyond the initial capture. A cell, once arrested onto the substrate, either performs quasi-steady rolling motion, or becomes firmly adhered depending on the four parameters Ca , ψ , ζ and κ . Figures 3.14 and 3.15 show the rolling motion of the cells for different Ca and ψ . Here we plot instantaneous cell velocity and displacement. The stochastic nature of the rolling motion is evident in these figures by the fluctuating cell velocity. The fluctuating velocity arises due to random formation and breakage of the receptor/ligand bonds. The instantaneous velocity decreases when a large number of bonds exists simultaneously, and it shoots up when the number of bonds decreases. On the average, the cell velocity in adhesive rolling motion is less than the velocity of a free-flowing cell which is also shown in the figures.

Comparison of figures 3.14 and 3.15 suggests that fluctuation in velocity increases with decreasing Ca . The time-averaged velocity also increases with decreasing Ca . Further, the rolling velocity decreases with increasing ψ .

We have performed a large number of simulations to explore the rolling characteristics as a function of cell deformability and bond properties. The time-averaged rolling velocity V is shown in figure 3.16 as a function of ψ for various Ca . Here we keep $\zeta = 5.0$ and $\kappa = 1.0$. Recall that for a given Ca , the cell will

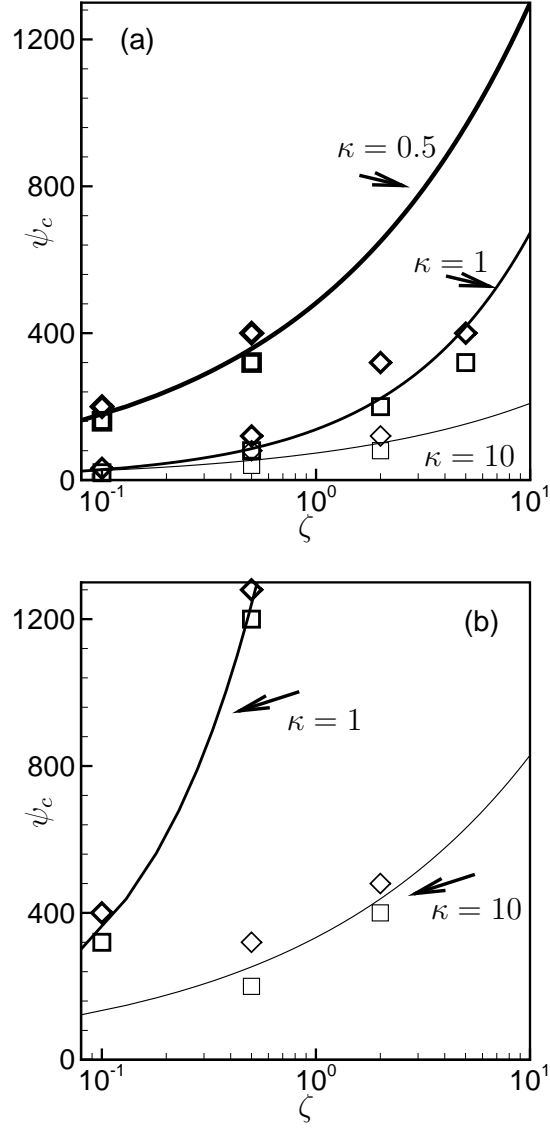


Figure 3.13: Phase diagram for cell capture/escape. Critical bond strength ψ_c as a function of ζ for $\kappa = 0.5, 1$, and 10 . a) $Ca = 0.002$, b) $Ca = 0.2$. $-\square-$ $P_c = 25\%$, $-\diamond-$ $P_c = 75\%$.

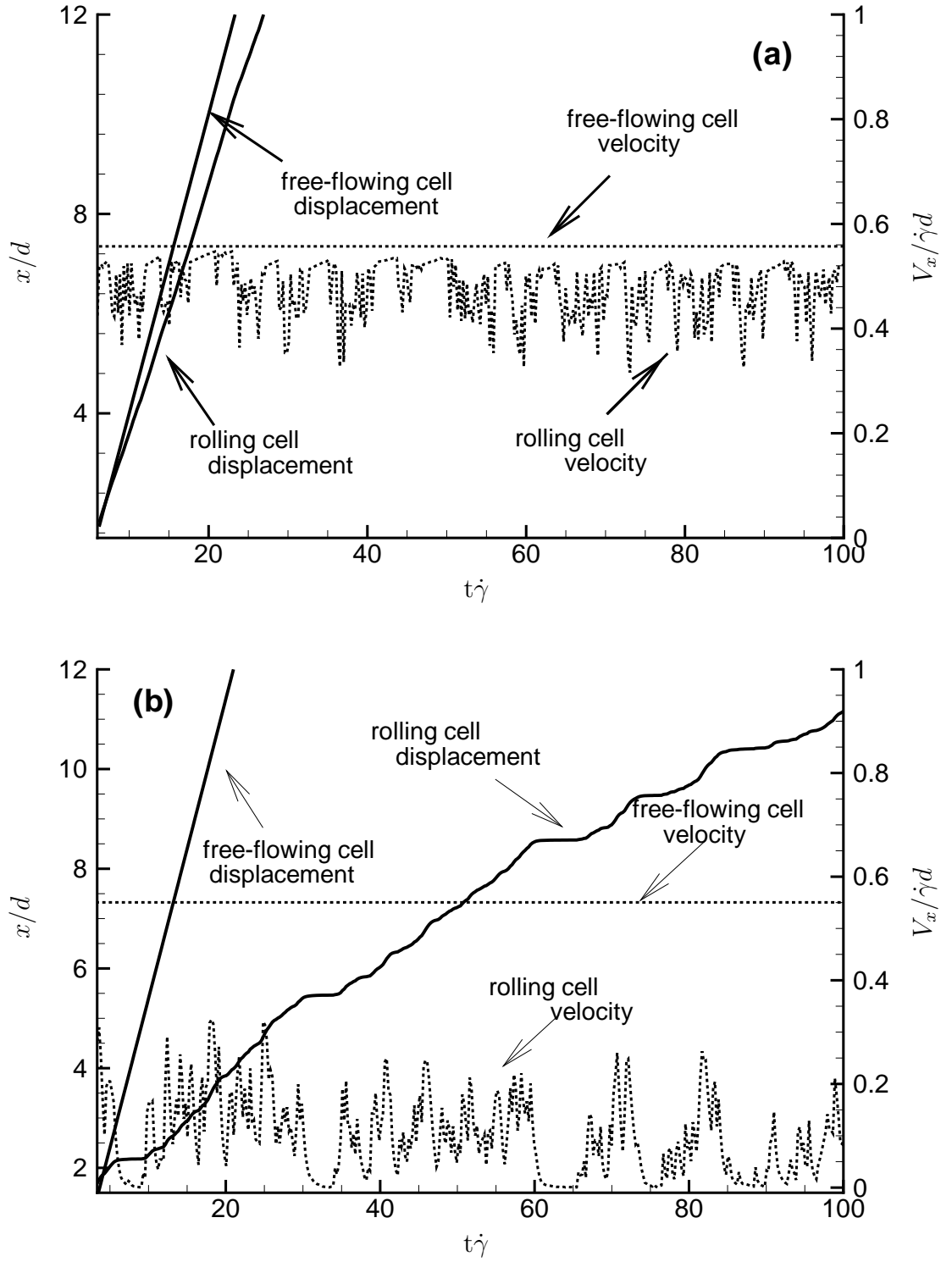


Figure 3.14: Time history of axial displacement and axial velocity of an adhesively rolling cell with $Ca = 0.002$ for different values of ψ . (a) $\psi = 90$, (b) $\psi = 440$. Also shown is the axial displacement and velocity of a free-flowing cell.

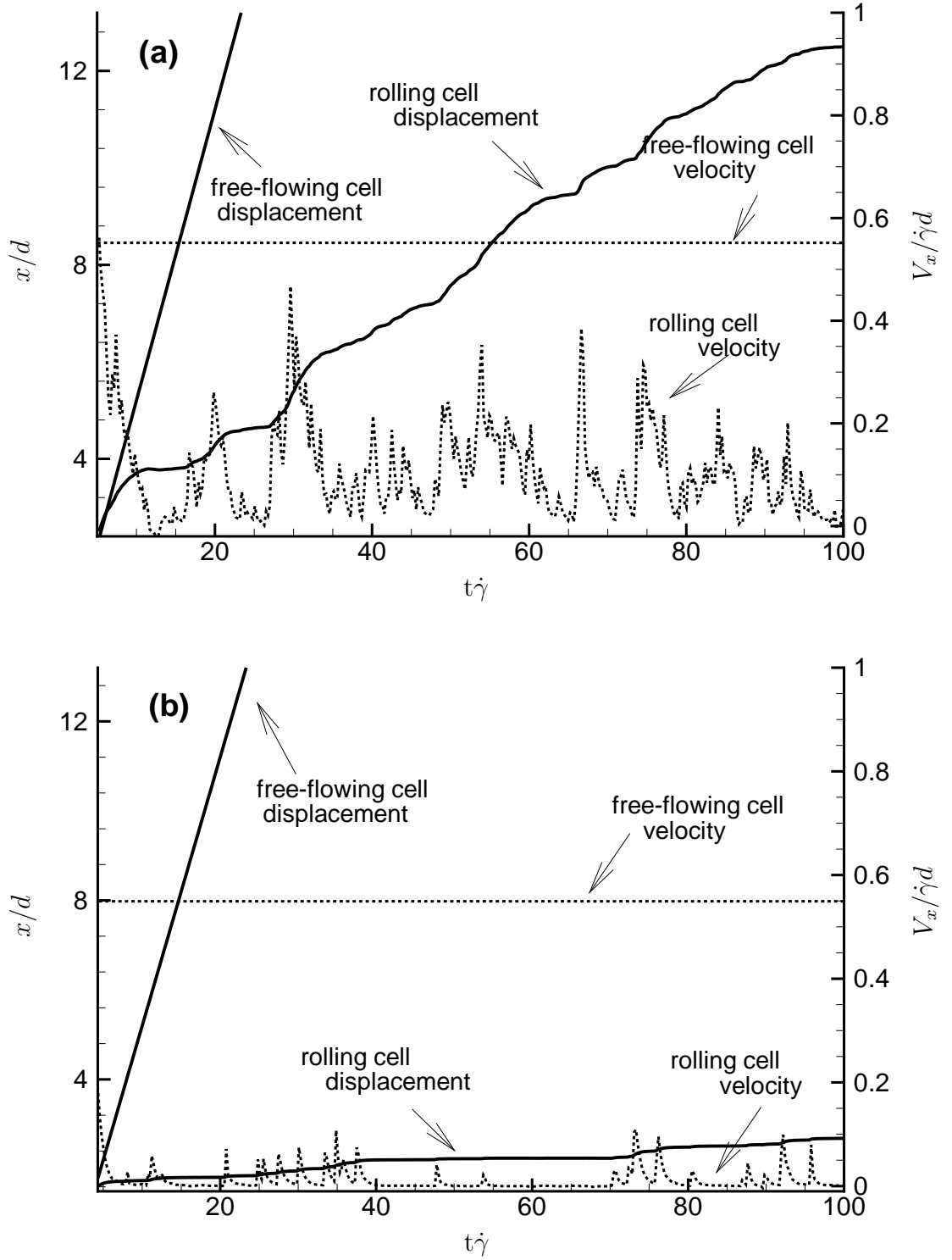


Figure 3.15: Time history of axial displacement and axial velocity of an adhesively rolling cell with $Ca = 0.02$ for different values of ψ . (a) $\psi = 220$, (b) $\psi = 370$. Also shown is the axial displacement and velocity of a free-flowing cell.

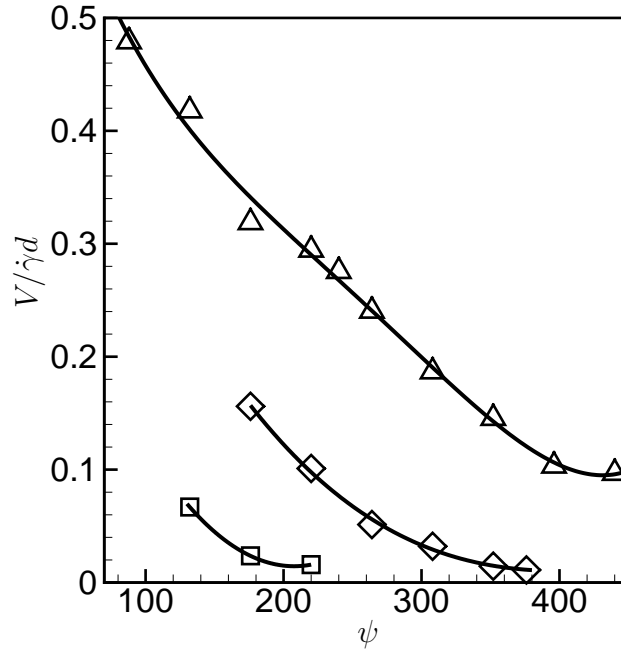


Figure 3.16: Average rolling velocity as a function of ψ for different Ca . $-\square-$ $Ca = 0.2$, $-\diamond-$ $Ca = 0.02$, $-\triangle-$ $Ca = 0.002$.

escape from the surface if ψ is low. In figure 3.16, the range of ψ indicates the range over which the rolling motion is observed. The lower limit of ψ is the one below which the cell escapes from the surface. The upper limit is the one above which no significant change in the rolling velocity is observed. Within this range, V first decreases with increasing ψ , and then appears to reach an asymptotic.

We note in figure 3.16 that the range of ψ over which the quasi-steady rolling motion is observed is quite large. The range decreases with increasing Ca . The lower limit of ψ increases with increasing Ca ; this is consistent with the phase diagrams presented earlier. The upper limit, in contrast, decreases with increasing Ca . Further, the asymptotic value of V at the upper limit of ψ decreases with increasing Ca . Indeed, $V/\dot{\gamma}d \approx 10^{-2}$ at the upper limit for higher Ca . Thus a

deformable cell slows down significantly at higher Ca . A relatively rigid cell, in contrast, can roll with higher asymptotic value of $V/\dot{\gamma}d$ (≈ 0.1 as evident in figure 3.16 for $Ca = 0.002$).

The result described above in figure 3.16 and the one presented earlier in figures 3.11 and 3.13 suggest that while a relatively rigid cell can be captured at a lower bond strength, it would require much higher bond strength to bring the cell to a complete stop (firm adhesion). In contrast, a more deformable cell can be captured only with a much stronger bond, but once captured the cell would come to a firm adhesion within a small range of ψ .

The dependence of the rolling velocity on ζ is considered in figure 3.17 for various Ca . Here ψ and κ are kept constants at 180 and 1, respectively. The rolling velocity increases with increasing ζ . As mentioned before, ζ gives an estimate of the inverse of the bond lifetime. Bonds break rapidly with increasing ζ resulting in reduced bond stretching, and hence reduced adhesion force, and higher rolling velocity. As noted earlier in figure 3.11, deformable cells (here $Ca = 0.2$ and 0.02) escape the wall at relatively lower values of ζ than the rigid cells ($Ca = 0.002$). This is due to the higher hydrodynamic lift force on the deformable cells. The rigid cells roll over a larger range of ζ . Figure 3.18 shows the maximum rolling velocity as a function of Ca that the cell attains before it lifts off the wall. Consistent with our previous discussion, the maximum rolling velocity decreases with increasing Ca .

The above results can be summarized as a qualitative phase diagram showing

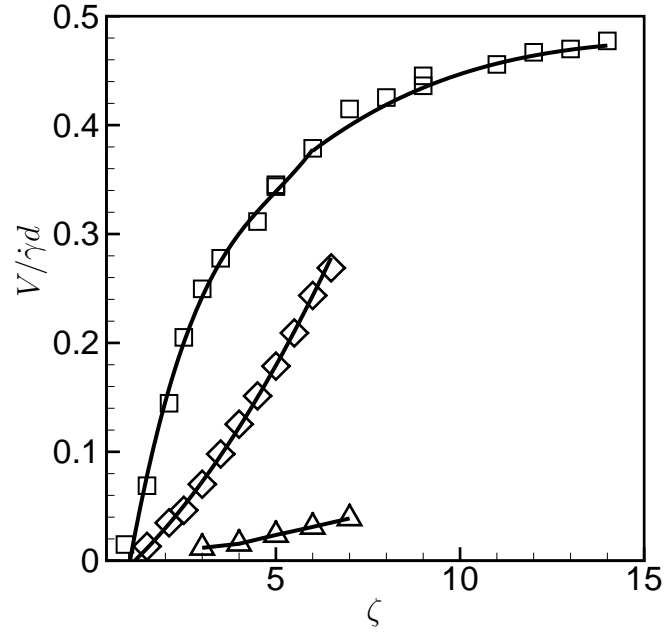


Figure 3.17: Average rolling velocity as a function of ζ for different Ca . \square — $Ca = 0.002$, \diamond — $Ca = 0.02$, \triangle — $Ca = 0.2$.

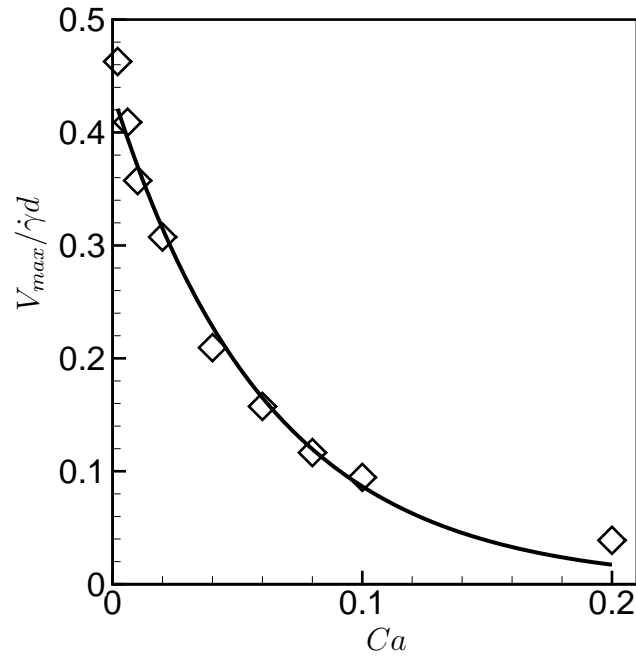


Figure 3.18: Maximum rolling velocity as a function of Ca .

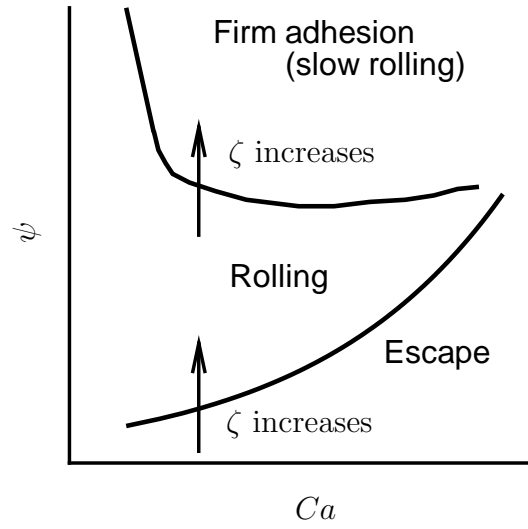


Figure 3.19: Qualitative phase diagram showing regions of escape, rolling and firm adhesion.

the three modes of motion: escape (free-flowing), adhesively rolling motion, and firm adhesion (slow rolling) as presented in figure 3.19. The boundaries between different regimes shift upward with increasing ζ .

Chapter 4

Rolling Motion and Deformation of Leukocytes on Adhesive Surfaces in Simple Shear Flow

4.1 Introduction

The adhesive motion of a wall-bounded cell was introduced in the last chapter. The results were presented over a large range of Ca , ψ , κ and ζ . The major result was that the cell performs rolling with a large range of rolling velocity $10^{-2} < V/\dot{\gamma}d < 1$. In this chapter, we focus on the rolling motion of leukocytes. Experiments show that the rolling velocities of leukocytes are typically in the range of $\approx 10 - 100 \mu\text{m/s}$; or $V/\dot{\gamma}d \sim 10^{-2}$. Thus we term this motion as ‘slow rolling’. Because of such small velocities, and due to its specific biological nature, we choose to present the results in dimensional form. We focus on P-selectin and PSGL-1 receptor/ligand pair. Hence the biophysical parameters are kept constant. We consider the variation of shear rate $\dot{\gamma}$ and the elastic modulus of the cell membrane E_s . In this chapter, we compare our numerical results on leukocyte rolling with many experimental measurements, both in vitro and in vivo. We also consider the effect of multiple leukocytes rolling simultaneously, as it is the case during inflammatory response in vivo.

4.2 Rolling dynamics

Snapshots of a rolling leukocyte obtained from a simulation at $\dot{\gamma} = 500\text{s}^{-1}$ and $E_s = 2.6 \text{ dyn/cm}$ are presented in figure 4.1. Shown here is a sequence of initial tethering, cell deformation, and tether breakage. In figure 4.1A, initial bonds are just formed on microvillus ‘1’. The cell shape is nearly spherical at this time. Upon initial tethering, the cell rotates clockwise due to the fluid torque (figure 4.1B). The rolling motion temporarily stops, and the cell deforms to make a flat contact area with the substrate (figure 4.1C). As a result, more microvilli become available for bond formation, such as microvillus ‘2’ in figure 4.1C. Subsequently, microvillus ‘1’ breaks, cell rolling commences, (figure 4.1D), and the contact area decreases. The cell is eventually tethered via microvillus ‘2’ (figure 4.1E). The contact area increases again, and microvilli ‘3’ and ‘4’ also become available for bond formation. Figure 4.1F shows the breakage of microvillus ‘2’ followed by cell rolling. In figure 4.1G, the cell is shown to tether again by microvillus ‘4’. This repeated process of bond formation and breakage continues, and the cell rolls in a ‘stop-and-go’ manner.

The rolling sequence of a more compliant cell ($E_s = 0.3 \text{ dyn/cm}$) is presented in figure 4.2. Figure 4.2A shows the initial arrest of the cell by tethering of microvillus ‘1’, followed by deformation of the cell into a ‘tear-drop’ shape in figures 4.2B–C. The contact area increases significantly, and four microvilli become available for bond formation. However, the cell is anchored only by microvillus

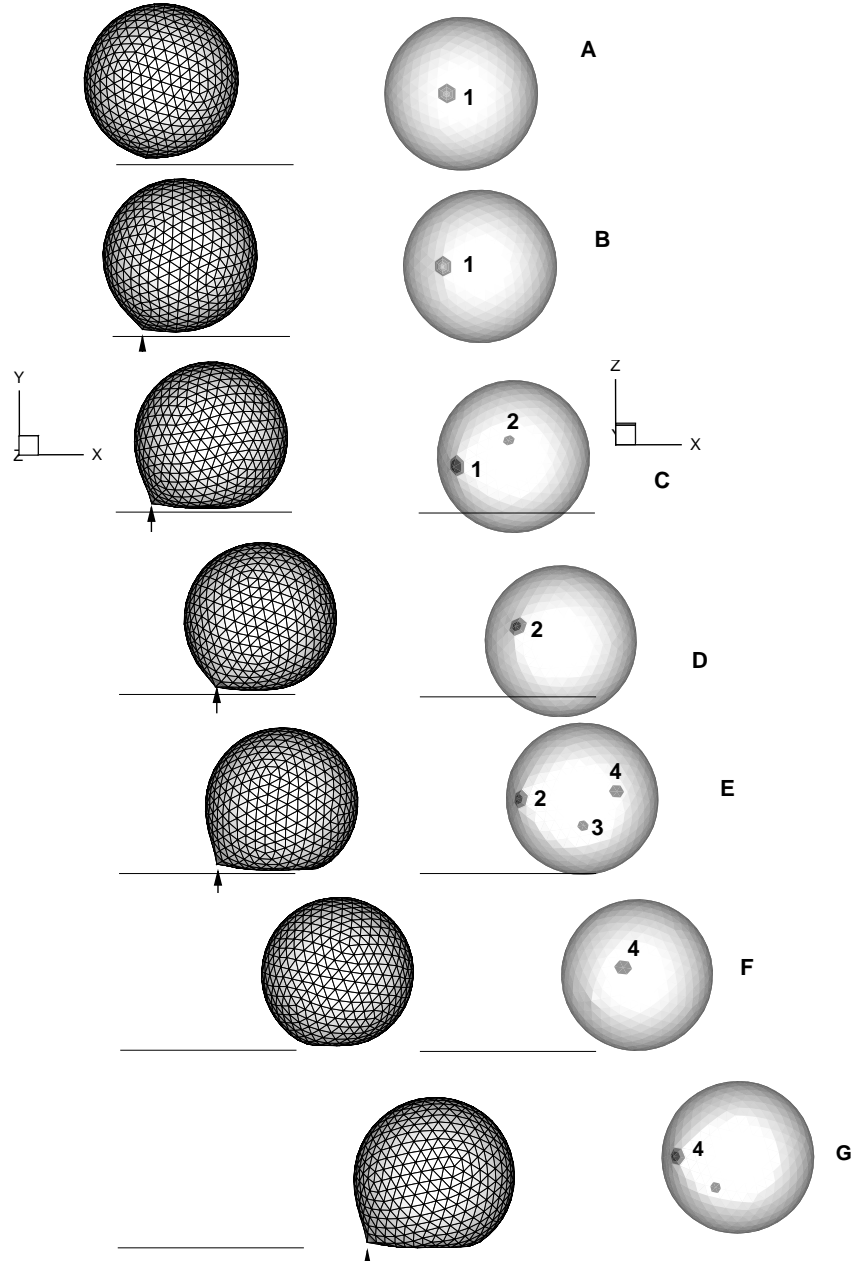


Figure 4.1: Sequence of a rolling leukocyte at $\dot{\gamma} = 500\text{s}^{-1}$ and $E_s = 2.6 \text{ dyn/cm}$. The shear flow, and the cell movement, are from left to right. The left panel shows sideview, and the right panel shows bottomview. Lagrangian mesh on the cell surface is also shown. In the bottomview, microvilli forming bonds are marked by numbers '1', '2' etc. The arrows indicate the location of tethering.

‘1’ located in the sharp corner formed at the trailing edge. In figure 4.2D, microvillus ‘1’ breaks, and the rear end of the cell retracts. Figures 4.2E and F show formation of a new tether via microvillus ‘2’, followed by cell spreading. Figures 4.1–4.2 show that during rolling adhesion, the cell shape deviates significantly from its spherical shape.

Further, a similar rolling sequence is shown for lower shear rate of 100s^{-1} in figure 4.3. The membrane stiffness of the cell is 2.6 dyn/cm . The cell again shows the characteristic ‘stop-and-go’ motion. Upon initially tethering, the cell is deformed leading to a flat contact area. At $t > 0.2\text{s}$, the tethered microvillus breaks, and the cell starts to roll. Subsequently, the cell is tethered again, and the cell spreads over the surface.

The ‘stop-and-go’ motion is further illustrated in figure 4.4 which shows cell displacement and velocity over time. As evident in figure 4.4a, the simulation is done for nearly 2.5s of leukocyte rolling. The cell motion is characterized by a series of steps during which the cell rolls, and pauses during which the cell is adherent. The stochastic nature of the cell motion is also evident by the fluctuations in cell velocity. Also shown in the figure is the displacement of a free-flowing cell for similar parameters which shows linear increase with time. The cell rolling velocity differs significantly from the free-flowing velocity. The ‘stop-and-go’ motion is due to formation and breaking of receptor/ligand bonds, and can only be predicted by stochastic simulation.

We show the role of shear rate and membrane stiffness in figures 4.5 and 4.6.

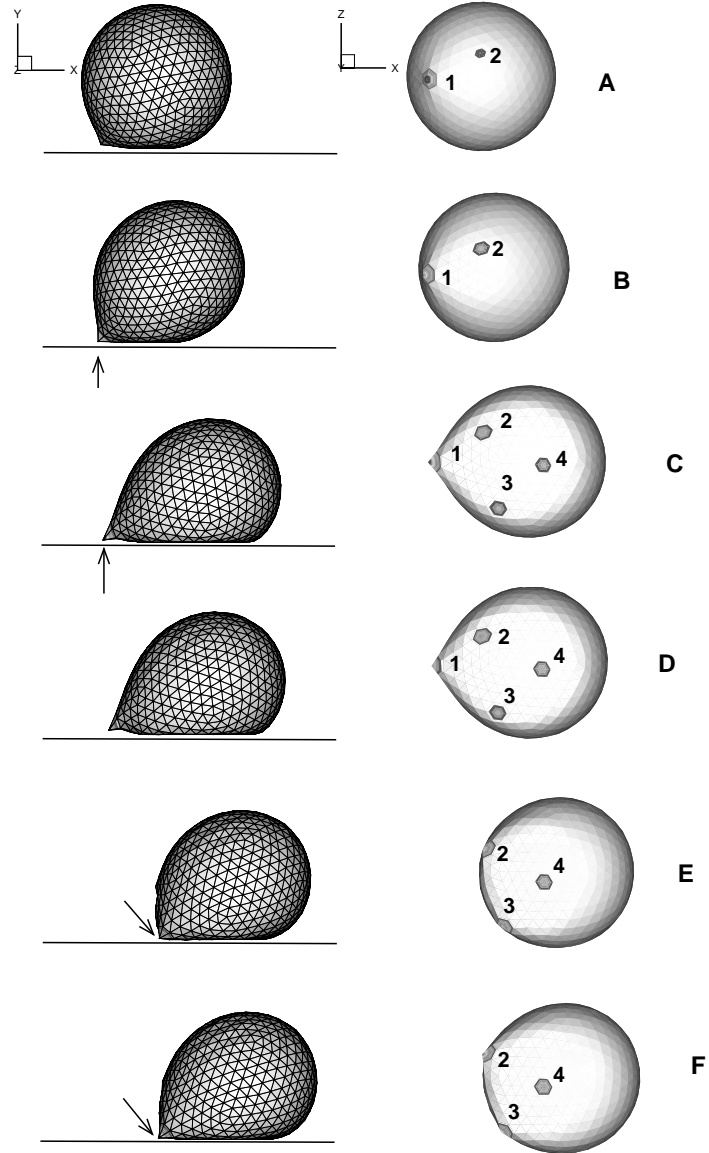


Figure 4.2: Same as in figure 4.1 except $E_s = 0.3\text{dyn/cm}$. The arrows indicate the location of tethering.

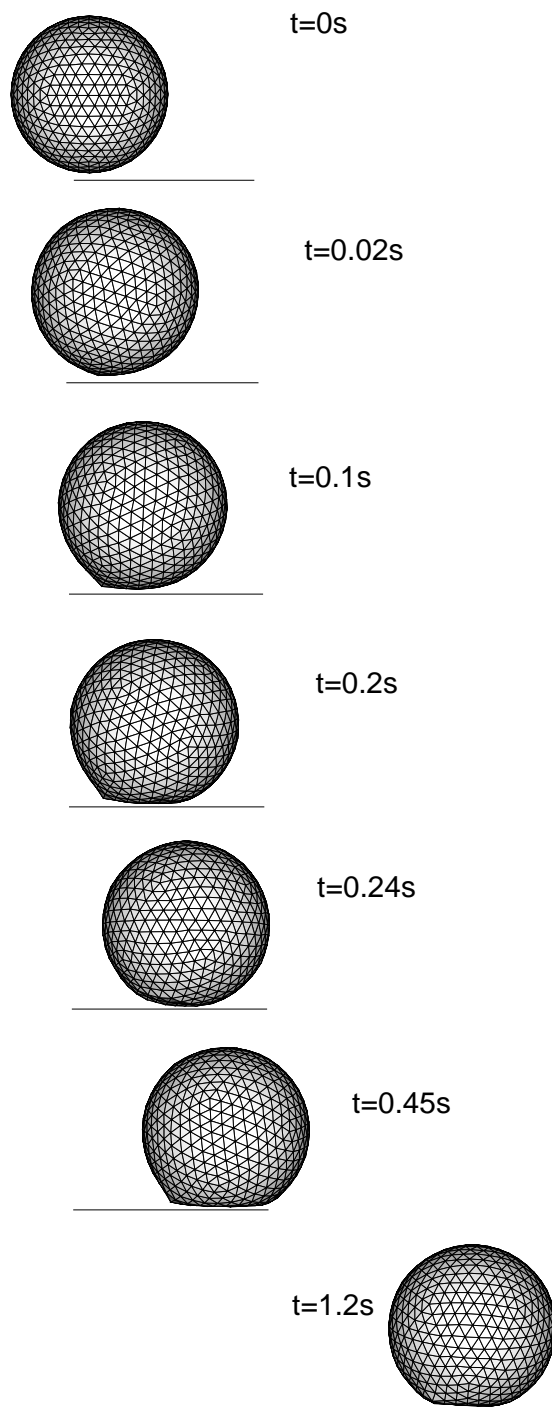


Figure 4.3: Rolling sequence at 100s^{-1} shear rate and $E_s = 2.6 \text{ dyn/cm}$.

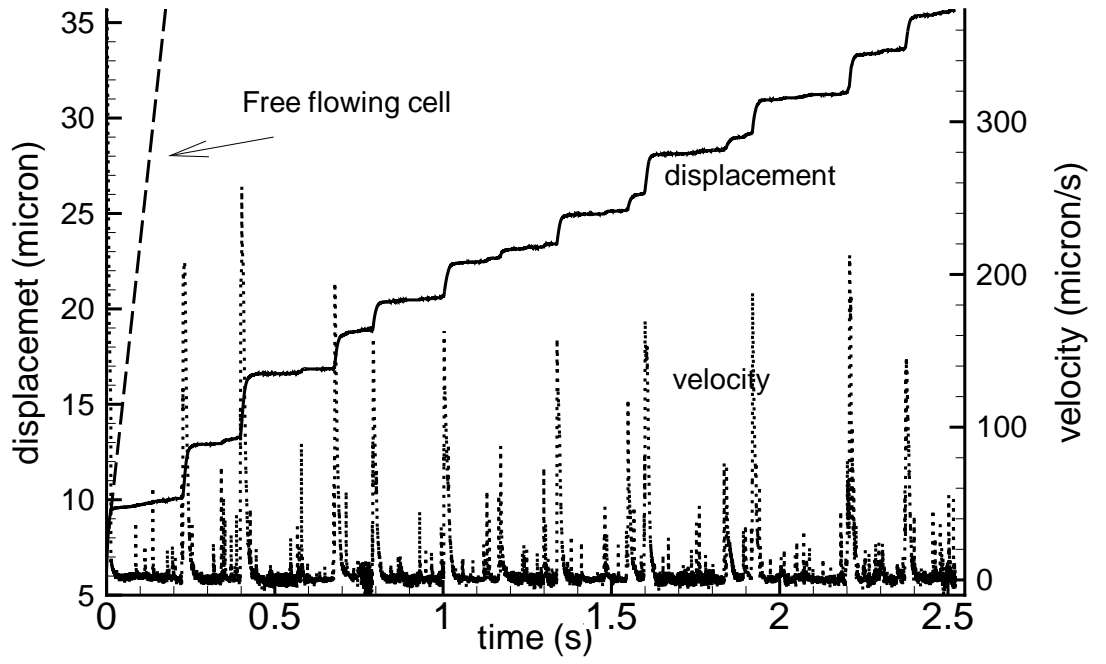


Figure 4.4: Rolling characteristics at $\dot{\gamma} = 100\text{s}^{-1}$, and $E_s = 2.6 \text{ dyn/cm}$. History of cell displacement (solid line) and instantaneous rolling velocity (dotted line). Also shown is the displacement(dashed line) of a free flowing cell under similar flowing environment.

Effect of varying shear rate at a constant $E_s = 0.3$ dyn/cm is illustrated in figure 4.5 which show shorter pause times and more frequent steps with increasing shear. The instantaneous rolling velocity corresponding to the trajectories is also shown in the same figure (right panel) which show increasing fluctuations with increasing shear rates.

Effect of varying membrane stiffness at a constant shear rate as illustrated in figure 4.6, which show decreasing step sizes and longer pause times with decreasing stiffness. The instantaneous rolling velocity is also shown (right panel). The fluctuations in velocity increase with increasing membrane stiffness. Together figures 4.5 and 4.6 imply that a leukocyte rolls less stably at higher shear rate and membrane stiffness.

Interestingly, our simulations predict that during the rolling motion, a leukocyte can undergo a significant sideways movement. Figure 4.7 shows the instantaneous lateral displacement and velocity of the cell at $\dot{\gamma} = 500\text{s}^{-1}$ and $E_s = 2.6$ dyn/cm. The sideways motion is purely due to the stochastic nature of bond formation, and discrete nature of microvilli presentation. A microvillus can form an initial tether that may be oriented at a non-parallel angle with the shear flow, causing the cell to move sideways once an earlier tether breaks. However, once the cell is tethered by the new microvillus, it quickly orients itself parallel to the flow.

The effect of membrane compliance on the sideways motion is shown in figure 4.8. Figure 4.8a shows the time history of lateral velocity for a cell with $E_s = 0.3$ dyn/cm and flowing at $\dot{\gamma} = 100\text{s}^{-1}$, while 4.8b shows a less deformable cell with

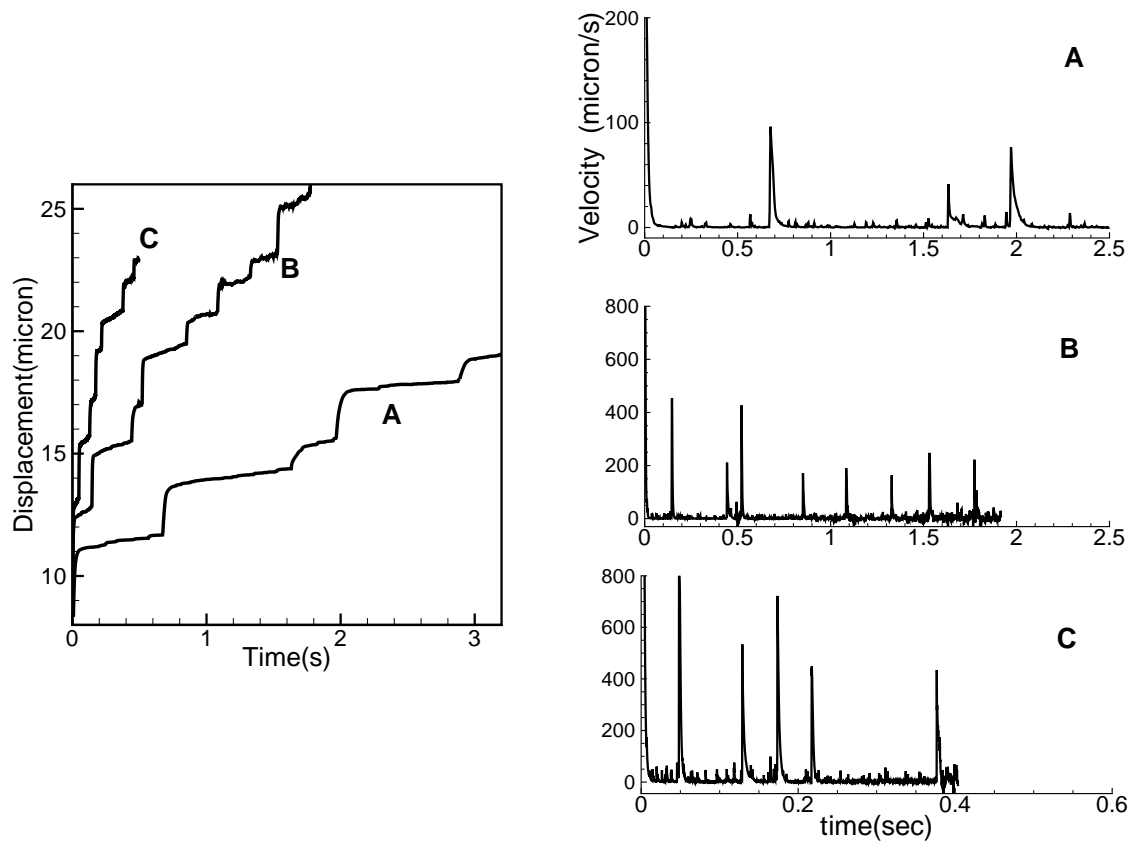


Figure 4.5: Effect of shear rate on the rolling dynamics. Axial displacement (left figure) and axial velocity (right figures) of a rolling leukocyte. A, B and C represent 100s⁻¹, 300s⁻¹, and 500s⁻¹, respectively at a constant $E_s = 0.3$ dyn/cm.

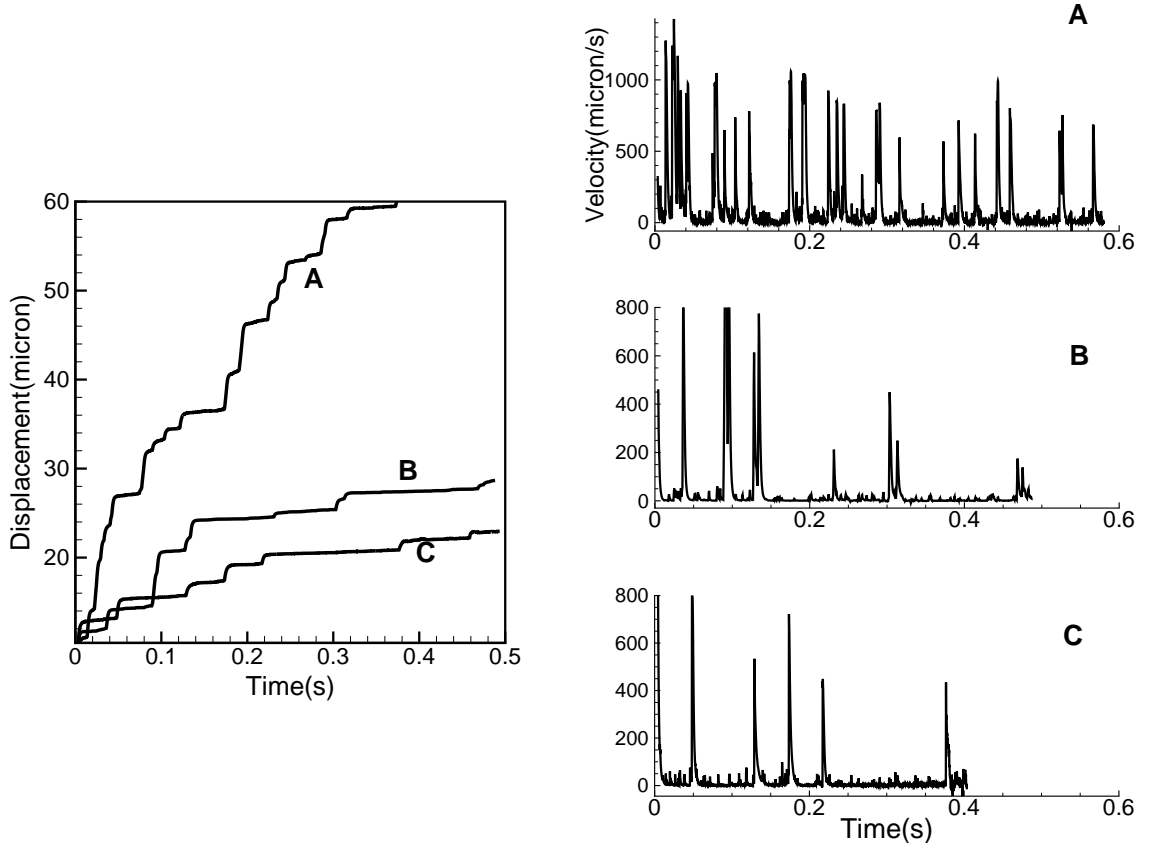


Figure 4.6: Effect of membrane stiffness on rolling dynamics. Axial displacement (left figure) and axial velocity (right figures) of a rolling leukocyte. A, B and C represent $E_s = 2.6$, 0.9 , and 0.3 dyn/cm, respectively, at a constant $\dot{\gamma} = 500\text{s}^{-1}$.

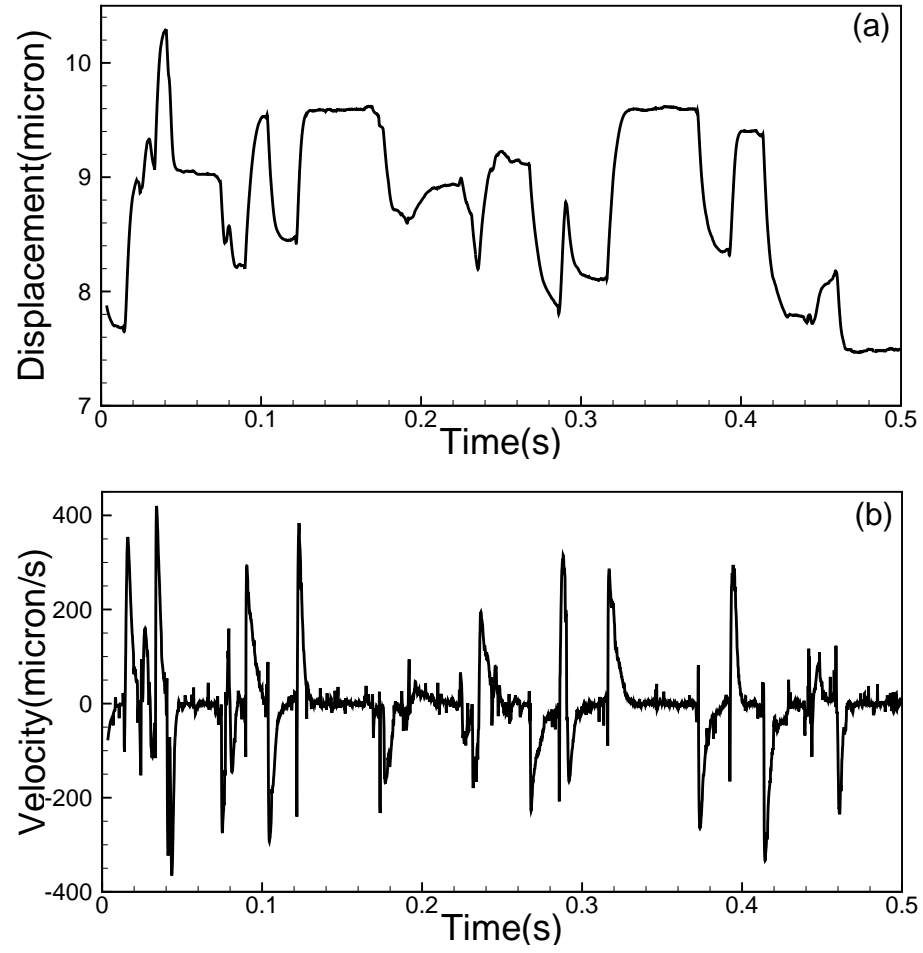


Figure 4.7: Sideway (a) displacement and (b) velocity of a rolling leukocyte for $\dot{\gamma} = 500 \text{ s}^{-1}$, and $E_s = 2.6 \text{ dyn/cm}$. The case shown is the same as in figure 4.6A.

$E_s = 2.6$ dyn/cm at the same shear. The fluctuations in the velocity for the compliant cell are significantly less. This again signifies the importance of cell deformation in stabilising cell rolling.

Time-averaged rolling velocity is shown in figure 4.9. Average rolling velocity varies from about 4 to 112 $\mu\text{m/s}$. It increases with increasing shear rate and increasing membrane stiffness. In the figure, we compare our results with experimental measurements of Kim and Sarelius [8] which show reasonable agreement.

The average pause time of a rolling leukocyte obtained from our simulations is shown in figure 4.10a. The average pause time varies between 0.04 and 0.6s. It strongly depends on the shear rate, and decreases with increasing shear rate. The pause time depends strongly on the membrane compliance at low shear rate, but weakly at higher shear rate. It increases with increasing membrane compliance. In figure 4.10a, we compare our computed pause times with the experimental data of Smith *et al.* [10], and find reasonable agreement. The average step size of a rolling leukocyte obtained from our simulations is shown in figure 4.10b. The step-size varies from about 1.8 to 4.2 μm . The step-size does not depend strongly on shear rate but has a much greater dependence on the membrane compliance.

As a quantification of the stochastic nature of cell rolling, we compute RMS (root-mean-square) of instantaneous rolling velocity in axial direction which is shown in figure 4.11a. The RMS of the axial velocity shows a strong dependence on shear rate and membrane stiffness. The RMS increases with increasing shear rate, and membrane stiffness. Figure 4.11b shows the RMS velocity in the lateral

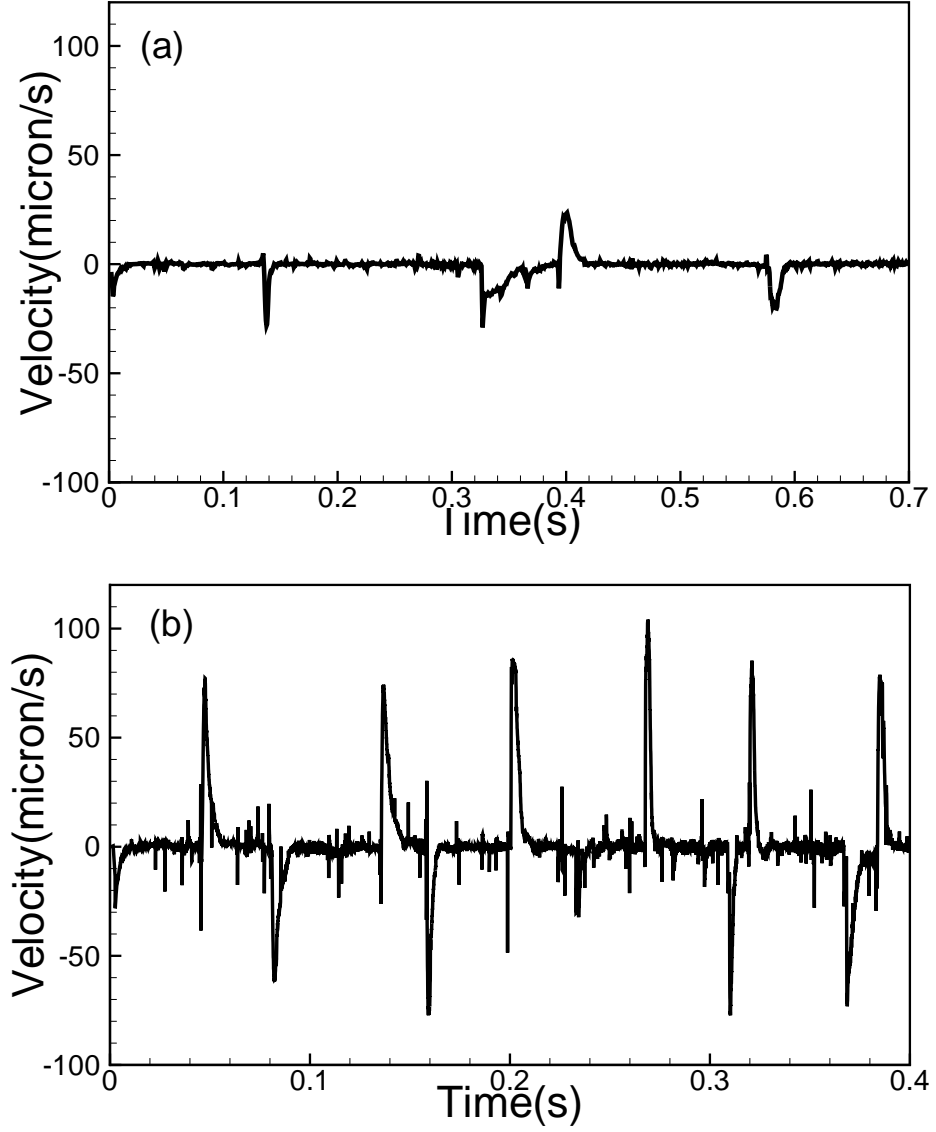


Figure 4.8: Effect of membrane stiffness on the sideways motion at constant $\dot{\gamma} = 100\text{s}^{-1}$. (a) $E_s = 0.3 \text{ dyn/cm}$, (b) $E_s = 2.6 \text{ dyn/cm}$.

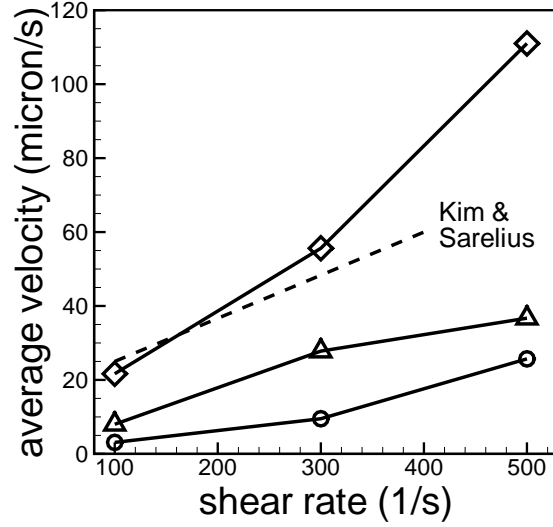


Figure 4.9: Average rolling velocity as a function of shear rate and membrane stiffness. Present results: \circ $E_s = 0.3$, \triangle $E_s = 0.9$, \diamond $E_s = 2.6$ dyn/cm. Experimental results: - - - Kim & Sarelius [8].

direction. The RMS velocity shows a similar trend as that of the axial velocity RMS and is comparable to, though lower than, that of the axial velocity.

4.2.1 Effect of nearby cells

In vivo experiments conducted by King *et al.* [78] showed that the rolling velocity was strongly dependent on the local concentration of leukocytes. We consider the effect of cell-to-cell separation distance on the rolling characteristics of deformable cells. All cells are assumed to roll simultaneously in the simulation by using the periodicity condition in the streamwise direction. In reality, the rolling motion would not be synchronized as done in the simulations. In figures 4.12 and 4.13, we show the cell trajectory and instantaneous velocity for four cases by varying

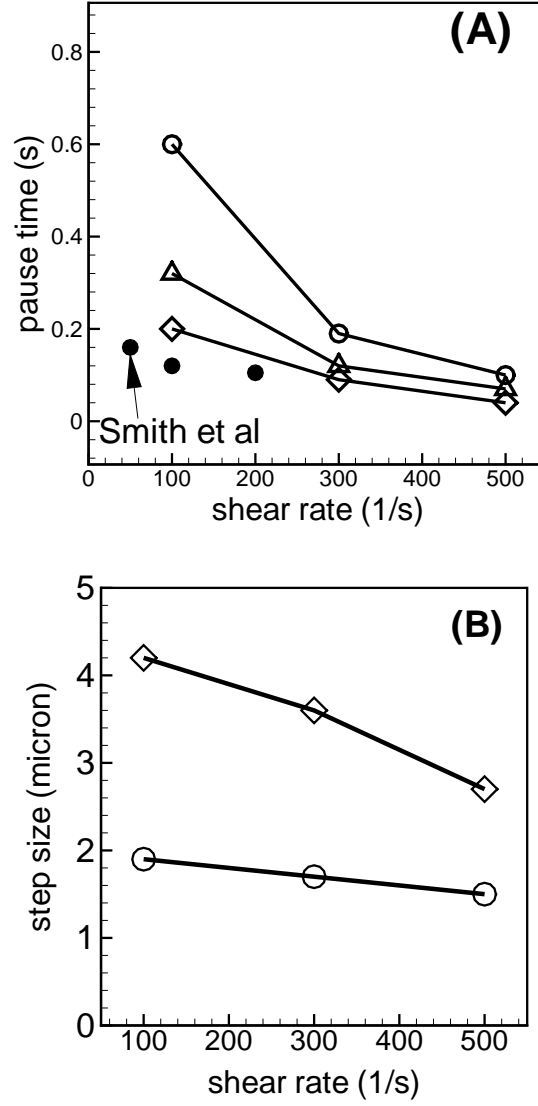


Figure 4.10: (a) Average pause time, (b) Average step size as functions of shear rate and membrane stiffness. $-\diamond-$ $E_s = 2.6$, $-\triangle-$ $E_s = 0.9$, and $-\circ-$ $E_s = 0.3$ dyn/cm. \bullet represent in vitro data of Smith *et al.* [10].

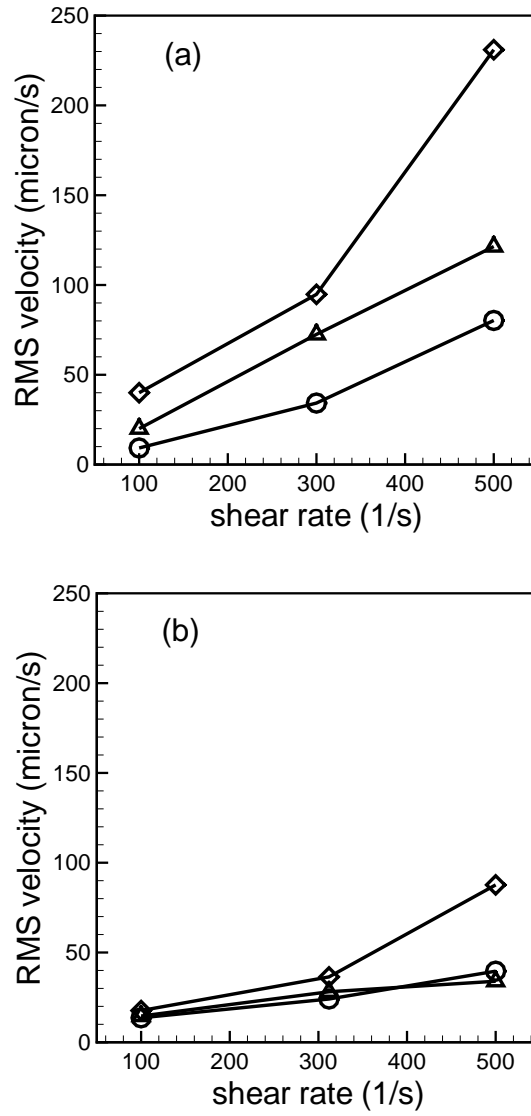


Figure 4.11: RMS velocity fluctuation of (a) axial and (b) sideways motion. \circ $E_s = 0.3$, Δ $E_s = 0.9$, and \diamond $E_s = 2.6$ dyn/cm.

the cell deformability and separation distance at $\dot{\gamma} = 300\text{s}^{-1}$. Figure 4.12 shows the effect of cell concentration for a cell with $E_s = 2.6 \text{ dyn/cm}$, while 4.13 shows the effect for a more compliant cell with $E_s = 0.3 \text{ dyn/cm}$. We note that the duration of these simulations varies from 1 to 2s of leukocyte rolling. Consistent with the results of King *et al.* [78], the distance traveled by the leukocytes is less in presence of nearby leukocytes. The velocity fluctuations for a compliant cell are significantly lower. Further, it is also observed that the fluctuations in rolling velocity decrease with increasing cell concentration.

Time-averaged rolling velocity as a function of cell deformability and number of adherent cells is shown in figure 4.14a for a shear rate of 300s^{-1} . We vary the number of rolling cells from 1 to 6, and also vary the cell deformability as $E_s = 2.6, 0.9$, and 0.3 dyn/cm . As expected, the rolling velocity decreases with increasing cell concentration, and cell deformability. For $E_s = 2.6 \text{ dyn/cm}$, the rolling velocity drops by a factor of 3.7 as the number of cells increases from 1 to 6 per $100\mu\text{m}$ channel length. The amount of decrease is consistent with the in vivo measurements of King *et al.* [78]. In contrast, for $E_s = 0.3 \text{ dyn/cm}$, the rolling velocity drops by only a factor of 1.6 for the same increase in cell concentration.

Further quantitative comparison of the rolling velocity with $-1/r$ behavior as observed by King *et al.* [78] is presented in figure 4.14b. In the figure, the average rolling velocities are shown by symbols. We also plot $A - B/r$ curves by choosing A and B to fit the data. For all three values of E_s , $-1/r$ decrease of the rolling velocity is observed. The values of A and B are mentioned in the figure.

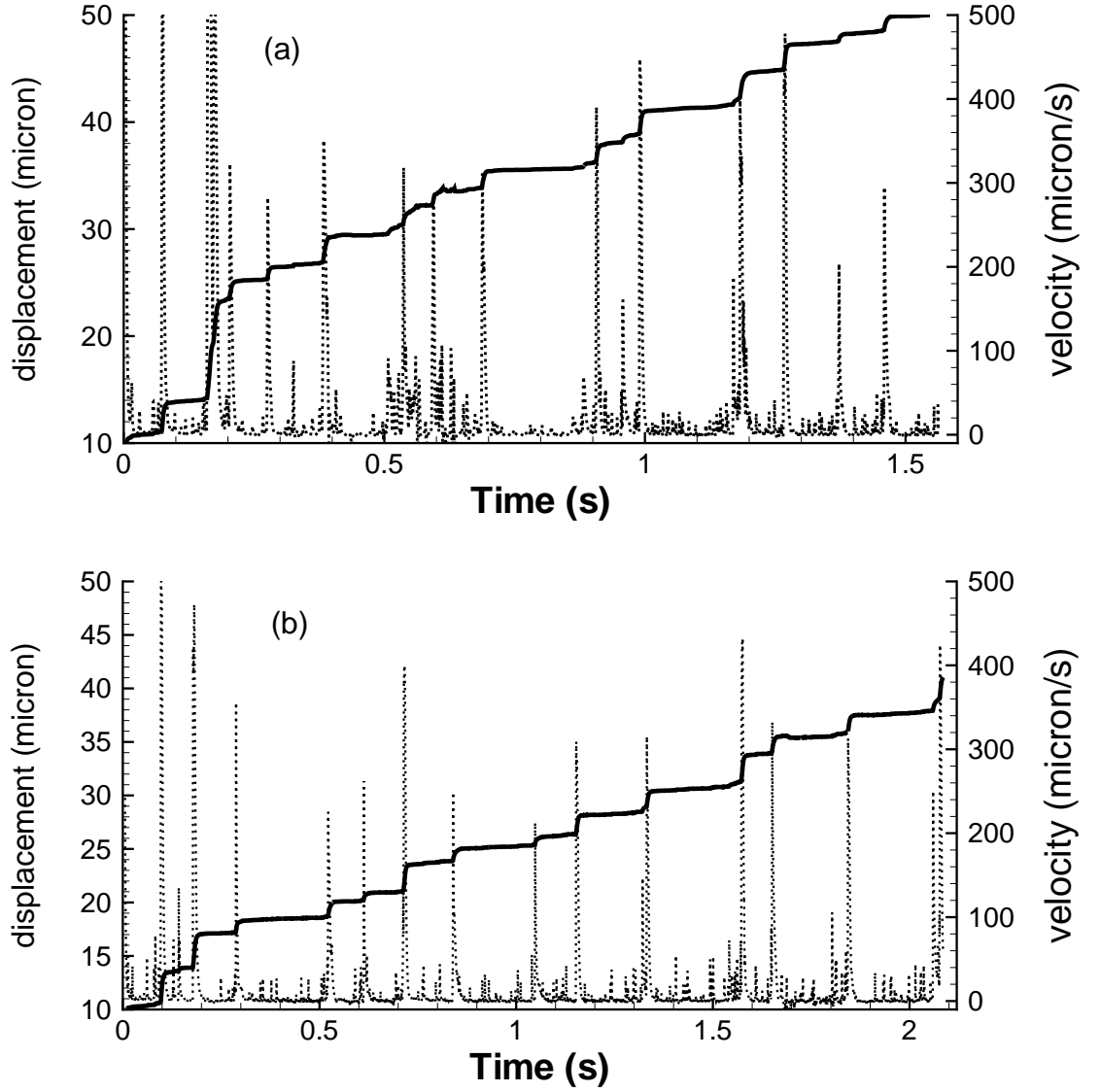


Figure 4.12: Effect of neighbouring cells on the rolling characteristics. Here $\dot{\gamma} = 300\text{s}^{-1}$ and $E_s = 2.6 \text{ dyn/cm}$. Solid line: cell trajectory. Dotted line: instantaneous velocity. (a) 3 cells/100 μm , and (b) 6 cells/100 μm .

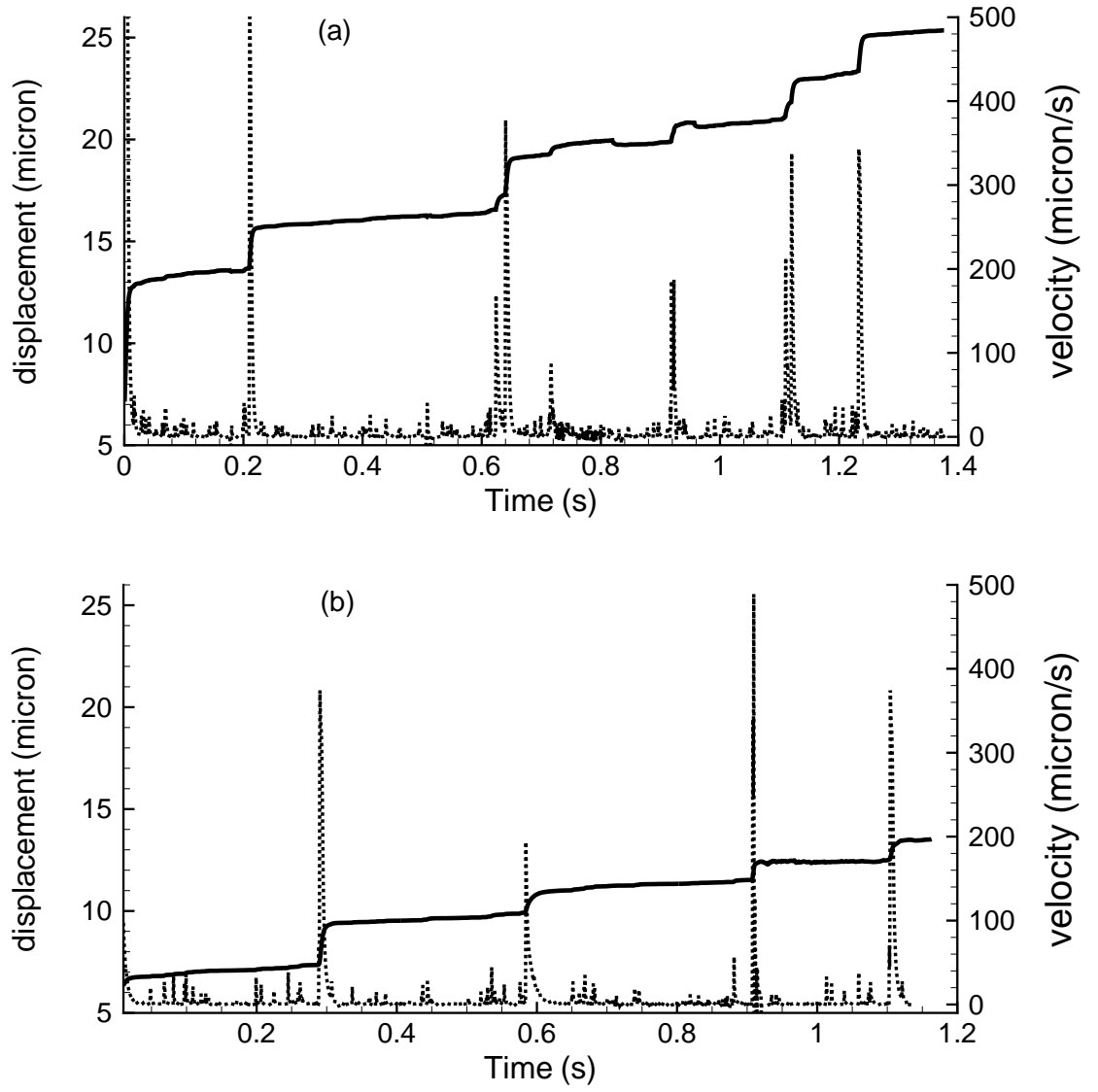


Figure 4.13: Same as figure 4.12 but $E_s = 0.3$ dyn/cm. (a) 1 cell/100 μm , and (b) 6 cells/100 μm .

Further, the effect of cell concentration on the stochastic nature of the process is measured. For $E_s = 2.6$ dyn/cm (rigid cells, figures 4.12), the variance in velocity fluctuations decreases from 655 to 256 $\mu\text{m}^2/\text{s}^2$ as the cell concentration increases from 3 to 6 per 100 μm vessel length; for $E_s = 0.3$ dyn/cm (compliant cells, figures 4.13), the variance drops from 196 to 89 $\mu\text{m}^2/\text{s}^2$ as the cell concentration increases from 1 to 6 per 100 μm vessel length. Thus for rigid cells, the effect of cell proximity is more significant.

The average pause times for the cases shown in figure 4.12 and 4.13 are 0.11s, 0.16s, 0.25s, and 0.28s respectively. This implies that the pause time increases with increasing cell deformability and leukocyte concentration. Again, the effect of separation distance is more prominent in case of rigid cells than compliant cells. The average step size for the above four cases are: 3.5, 2.4, 2.1, and 1.7 μm , which implies that the step size decreases with increasing cell concentration and cell compliance. Again, the change in step size w.r.t the cell concentration appears to be more in case of rigid cells than compliant cells.

4.3 Cell deformation

The cell deformation plays an important role in the rolling dynamics. As seen in figures (4.1, 4.2 and 4.3), the cell shape deviates significantly from its initial spherical shape. In order to quantify cell deformation, we measure a non dimensional parameter called the deformation index, L/H , where L is the end-to-end length along the flow direction, and H is the height of the cell. The higher the

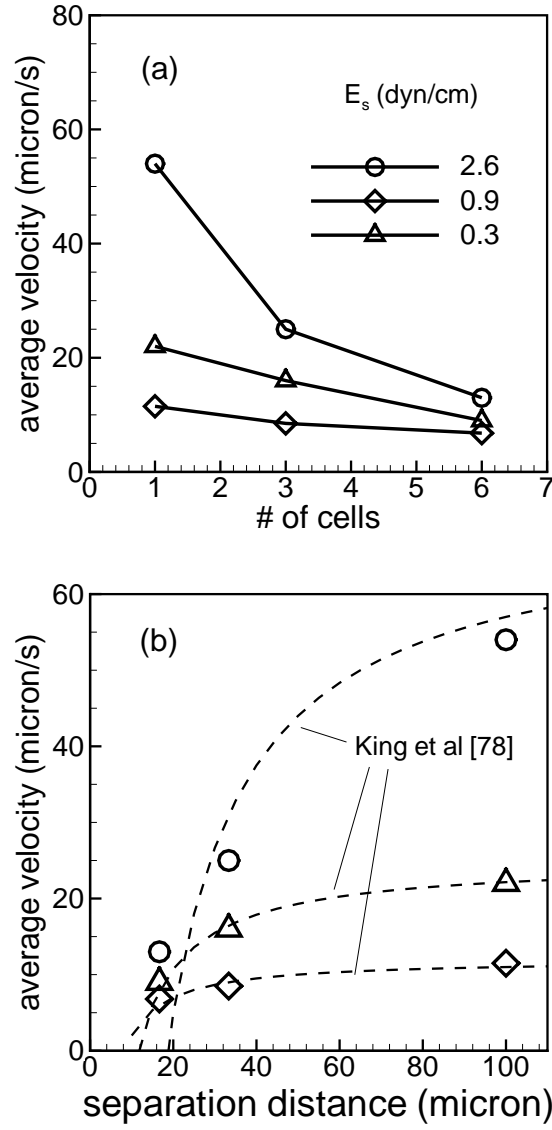


Figure 4.14: (a) Average rolling velocity as obtained from the simulations as a function of number of adherent cells/100 micron and E_s . \circ $E_s = 2.6$, Δ $E_s = 0.9$, and \diamond $E_s = 0.3$ dyn/cm. In (b), symbols are the simulation results, and dash lines represent $V = A - B/r$ curves, where A and B are chosen to match the results (following King *et al.* [78]). The values are $A = 70, 25, 10$, and $B = 1300, 285, 100$, for $E_s = 2.6, 0.9, 0.3$ dyn/cm, respectively.

value of the deformation index, greater is the deformation of the cell. Time history of deformation index is shown in figure 4.15. Also shown is the history of cell/substrate contact area. As the cell makes initial tether, L/H ratio and contact area increase sharply within 0.2s. Subsequently, during the rolling motion, instantaneous deformation index and contact area strongly vary with time. During the rolling motion, the contact area and deformation index increase when the cell is adherent, and decrease when the cell is rolling, in agreement with in vitro observation of Dong *et al.* [12]. Despite fluctuations, figure 4.15 shows that during the course of simulation, the contact area and deformation index remain statistically stationary except during the initial transience.

Time-averaged contact area and deformation index as functions of $\dot{\gamma}$ and E_s are shown in figure 4.16. The contact area varies from 11 to 40 μm^2 , and L/H varies from 1.07 to 1.5, for the range of shear rate and cell deformability shown in the figure. The contact area and deformation index increase with increasing cell compliance, resulting in increased number of receptor/ligand bonds and hence smoother rolling motion (reduced oscillation in instantaneous velocity). In this figure, we also compare our data with the in vivo measurements of Firrell & Lipowsky [22], based on the best-fit curves given in their paper. The in vivo contact area agrees with our results for more compliant cells, while the in vivo deformation index is higher than our prediction. Also shown is the data from the simulation of Jadhav *et al.* [35] for $E_s = 0.3 \text{ dyn/cm}$. The two simulation data agree qualitatively, but not quantitatively. This difference is most likely due to

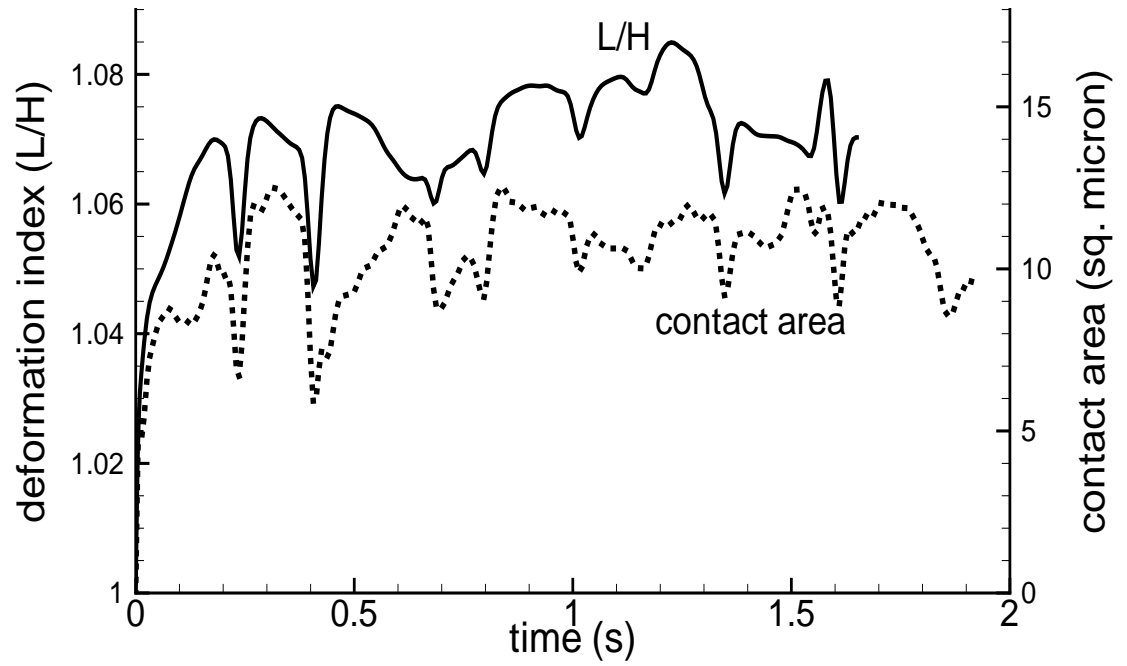


Figure 4.15: History of cell deformation index (L/H) (solid line) and contact area (dotted line) for a cell rolling at $\dot{\gamma} = 100\text{s}^{-1}$, and $E_s = 2.6 \text{ dyn/cm}$. This case is the same as shown in figure 4.4.

cell separation distance and size of the computational domain with respect to the cell size which are presumably not same in the two studies.

We further investigate the effect of cell concentration on cell deformation. Figure 4.17 and 4.18 show the time history of deformation index and contact area for $E_s = 2.6$ and 0.3 dyn/cm respectively. The fluctuations in deformation index and contact area correlate with the steps and pauses shown earlier. Qualitatively, both deformation index and contact area show fewer fluctuations for a compliant cell than for a rigid cell. Together figures 4.17 and 4.18 show that the fluctuations are reduced with increasing cell concentration.

Further, the time-averaged quantities of contact area and deformation index as function of cell concentration are shown in figure 4.19. The nearby cells provide a shielding from the hydrodynamic dispersive force and prevent cell deformation. Hence, the contact area and the deformation index decrease with increasing cell concentration as shown in figures 4.19a and b.

4.4 Biophysical Characteristics

4.4.1 Microvilli and bond dynamics

Next, we investigate the microvilli and bond dynamics during the rolling motion. Figure 4.20 shows the time history of the number of adhesive bonds and tethered microvilli during the rolling motion. The number of bonds and tethered microvilli changes rapidly with time. The figure suggests that these quantities also attain statistically stationary values during the course of the simulation after the initial

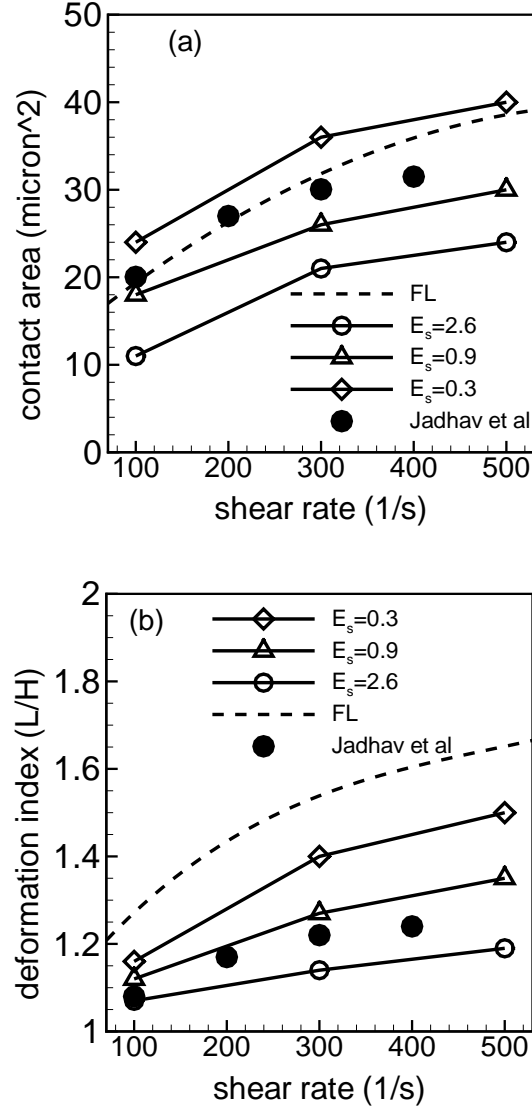


Figure 4.16: Mean contact area and deformation index (L/H) as functions of shear rate and E_s . Solid lines with symbols are the present results: \circ $E_s = 2.6$, \triangle $E_s = 0.9$, and \diamond $E_s = 0.3$ dyn/cm. Dash lines without symbols are in vivo measurements of Firrell & Lipowsky [22] (indicated by FL in the figure), and filled circles are computational results from Jadhav *et al.* [35] for $E_s = 0.3$ dyn/cm.

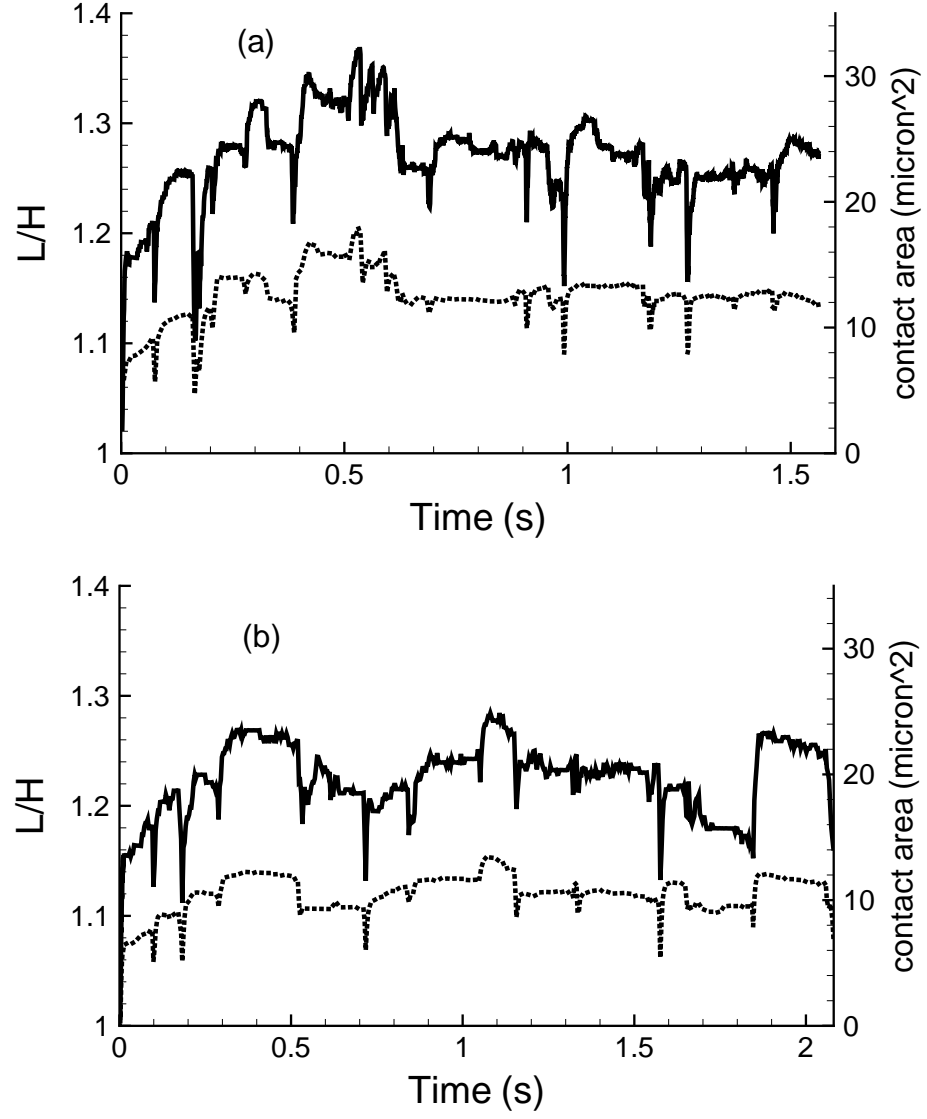


Figure 4.17: Effect of cell concentration on cell deformation for a cell with $E_s = 2.6 \text{ dyn/cm}$. Solid line: contact area. Dotted line: deformation index. $\dot{\gamma} = 300\text{s}^{-1}$. (a) 3 cells/100 μm , and (b) 6 cells/100 μm . This cases are similar to that shown in figure 4.12.

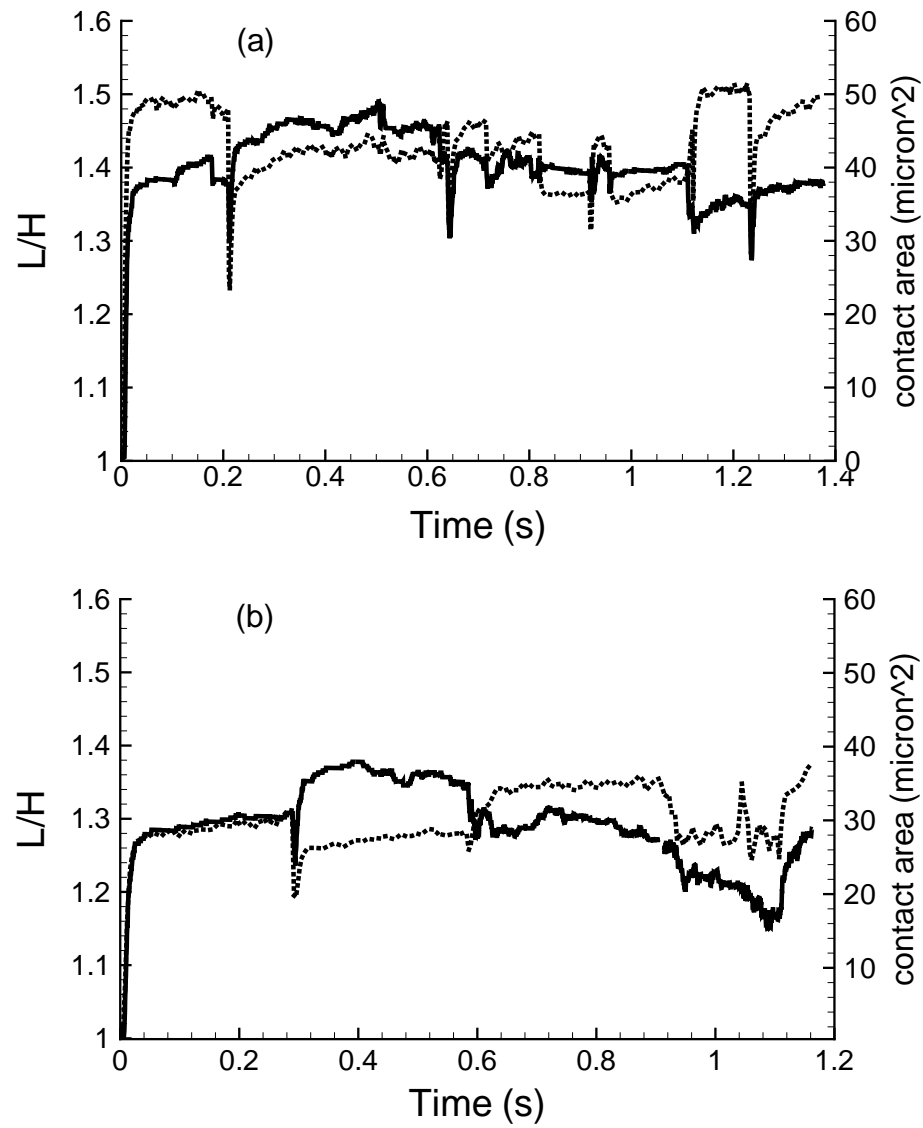


Figure 4.18: Same as figure 4.17 but $E_s = 0.3$ dyn/cm. (a) 1 cell/100 μm , and (b) 6 cells/100 μm .

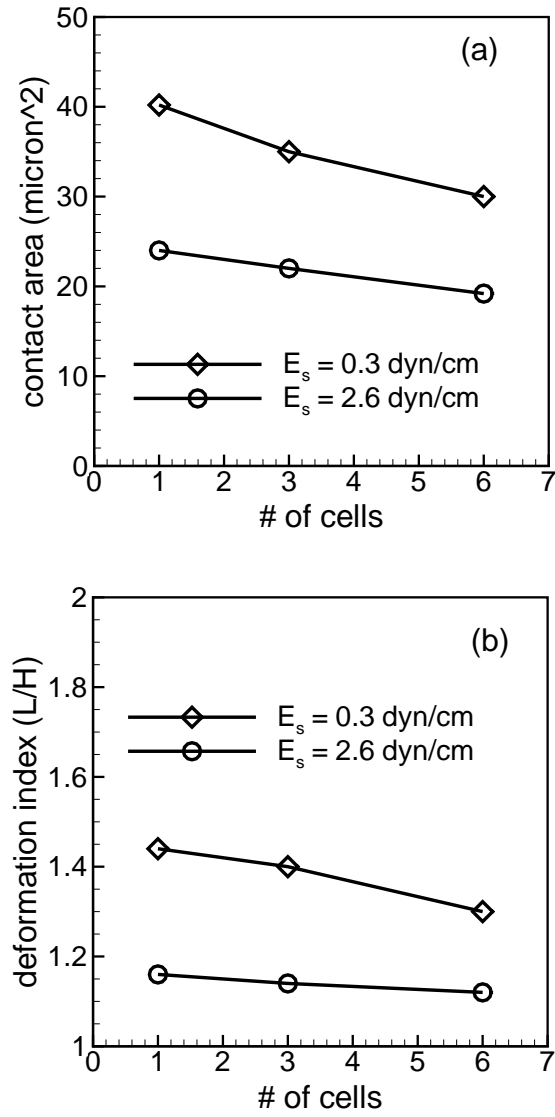


Figure 4.19: Time-averaged contact area and deformation index (L/H) as functions of number of adherent cells/100 micron.

transience is passed. Figure 4.20a and b show the effect of cell deformability ($E_s = 2.6$ dyn/cm and $E_s = 0.3$ dyn/cm respectively) at a constant shear rate of 100s^{-1} . The average number of bonds and tethered microvilli for the compliant cell (figure 4.20b) is higher than the rigid cell (figure 4.20a) due to increased contact area allowing for more microvilli to get engaged. As expected, the fluctuations in the number of bonds and microvilli are lower for the compliant cell. The effect of shear rate is shown in figures 4.20b and c for shear rates of 100s^{-1} and 300s^{-1} , respectively at a constant $E_s = 0.3$ dyn/cm. The fluctuations and the average values increase with increasing shear rate.

The dynamics of microvilli is studied by examining the history of the force on individual microvillus. A representative case at $\dot{\gamma} = 500\text{s}^{-1}$, and $E_s = 0.3$ dyn/cm is considered in figure 4.21a. The microvilli are identified by numbers ‘1’, ‘2’ etc. Strikingly, our simulations show that the force on a microvillus develops in steps. As an illustration, consider microvillus ‘4’ which comes in contact with the substrate and forms adhesion bonds at around $t = 0.03\text{s}$. However, the bonds on microvillus ‘4’ are not stretched until $t = 0.13\text{s}$ as the cell is tethered by microvilli ‘2’ and ‘3’. Hence the force acting on microvillus ‘4’ remains less than 10 pN. At $t = 0.13\text{s}$, microvillus ‘2’ breaks. As the cell begins to roll, bonds in microvilli ‘3’ and ‘4’ are stretched, and the forces on them sharply increase. Subsequently, the cell is tethered by microvillus ‘3’, and the force on it increases to about 350 pN. The force on microvillus ‘4’ also increases to 80 pN due to bond stretching. At around $t = 0.175\text{s}$, microvillus ‘3’ breaks. The cell rolls again, and the bonds in

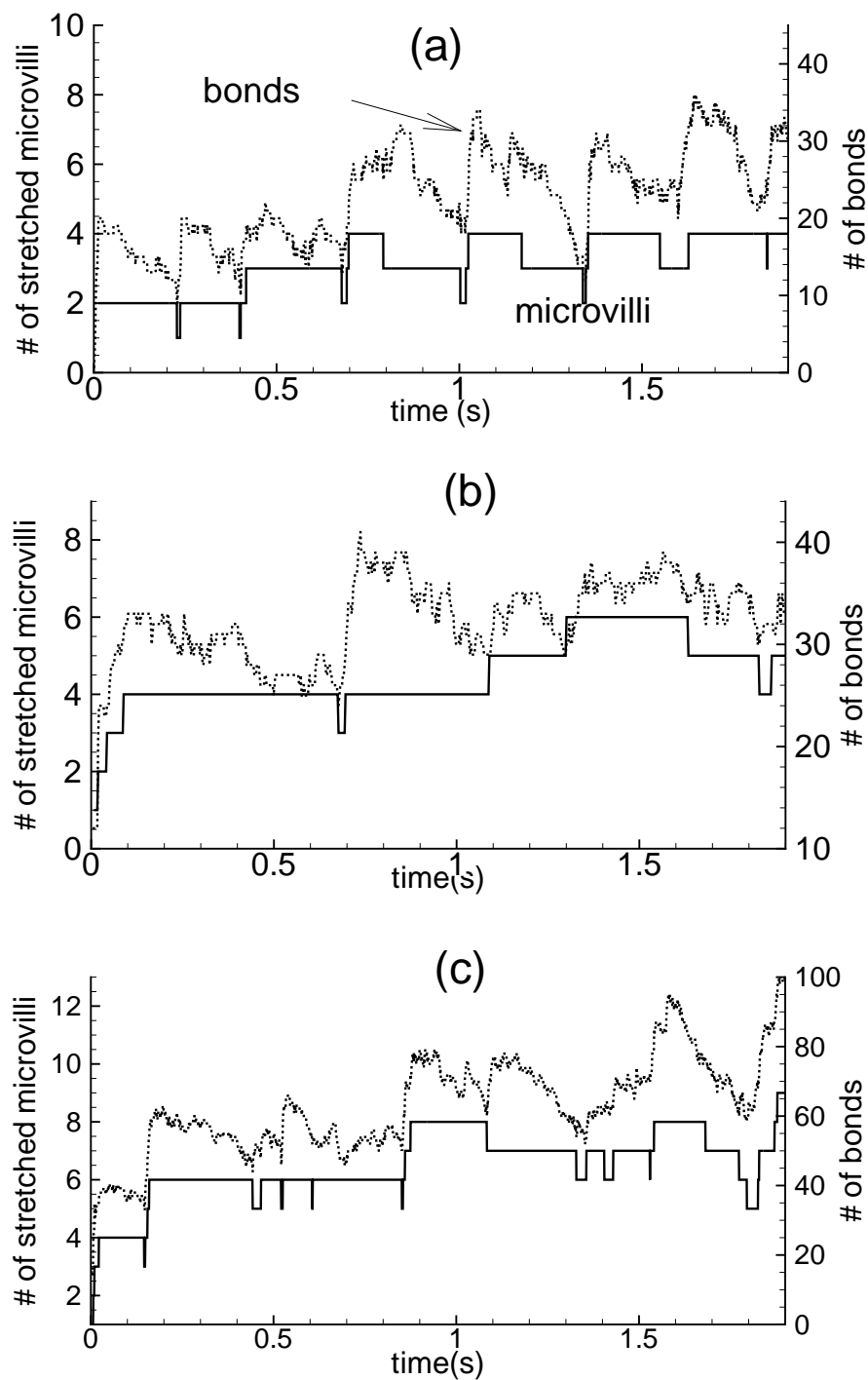


Figure 4.20: History of number of bonds (dotted line) and tethered microvilli (solid line). (a) $\dot{\gamma} = 100\text{s}^{-1}$, $E_s = 2.6\text{ dyn/cm}$, (b) $\dot{\gamma} = 100\text{s}^{-1}$, $E_s = 0.3\text{ dyn/cm}$, and (c) $\dot{\gamma} = 300\text{s}^{-1}$, $E_s = 0.3\text{ dyn/cm}$.

microvillus ‘4’ are stretched further, and the force jumps to 280 pN.

Likewise, the bond dynamics is examined in figure 4.21b. Formation and breakage of individual bond occur throughout the lifetime of a tether. We also observe that during a pause in the rolling motion, individual bonds within the tethered microvillus can break. When one bond breaks, forces on the remaining bonds in the cluster increase in a step-like manner. It also implies that multiple bond breakage, rather than a single event, is necessary for a microvillus tether to break. We also note that for a few bonds, the peak force on individual bond is as high as 50 pN, while for others the force remains below 10 pN. It suggests that, though multiple bonds are present, not all of them are “effective” in tethering the cell. We observe that multiple, rather than single, selectin bonds form per microvillus. When a tethered microvillus breaks and pulls from the substrate, several bonds, varying from 9 to 14, break simultaneously. But breakage of individual bond does not lead to the breakage of the tether, as other bonds quickly stretch to share the load. Simultaneous breakage of multiple bonds can only cause a tether to retract.

The average number of microvilli that form tethers, and the total number of microvilli available within the contact area as functions of shear rate and membrane stiffness are shown in figure 4.22. We consider the number of microvilli as $N_{mv} = 21$ and 155. For $N_{mv} = 155$, the number of microvilli within the contact area increases with increasing shear rate and membrane compliance. For the

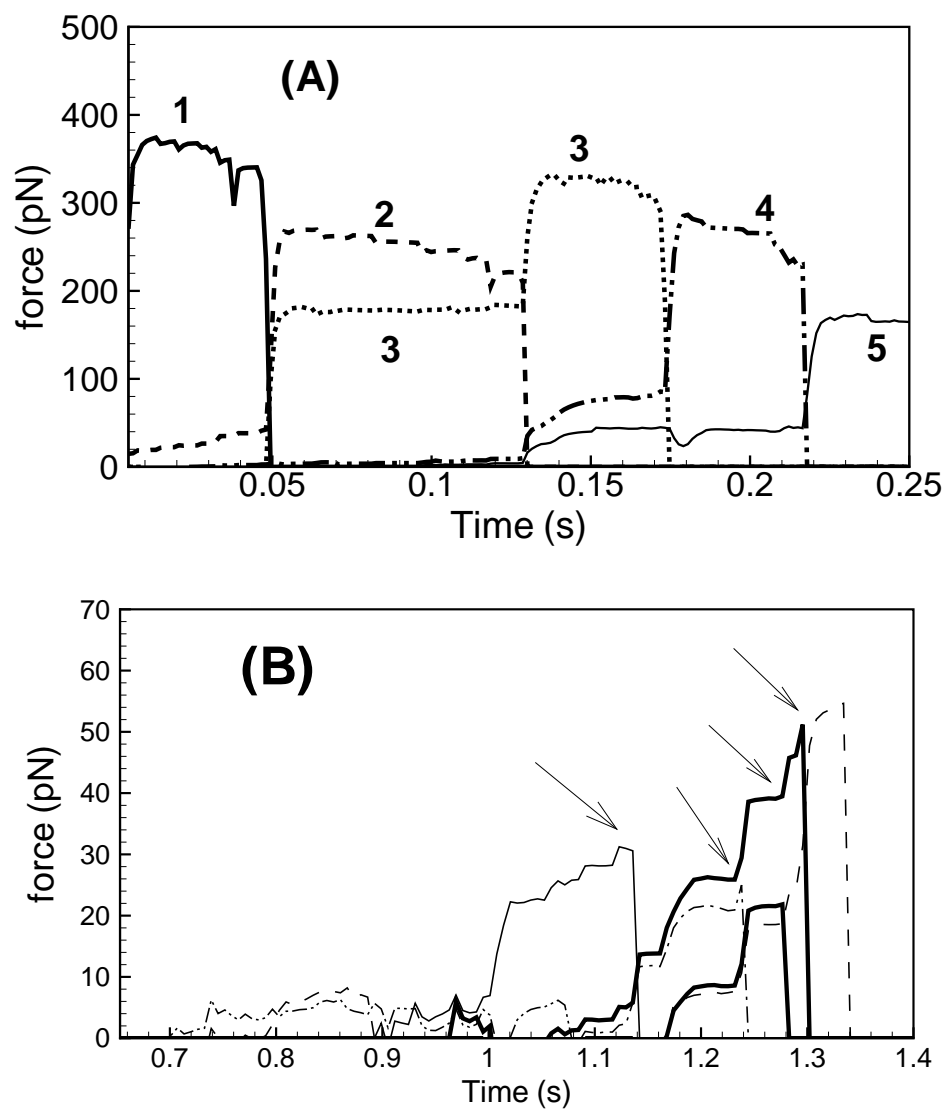


Figure 4.21: (a) Force history of a few microvilli, and (b) force history of a few bonds within a particular microvillus. In (a), microvilli are indicated by number '1', '2' etc. In (b) arrows indicate step increase in a bond force in response to breaking of another bond.

most compliant cell considered here at $\dot{\gamma} = 500\text{s}^{-1}$, nearly 35 microvilli are available in the contact area. However, only 5 of them form tethers. The number of tethers increases slightly with increasing shear rate and membrane compliance. Our simulations predict that leukocyte adhesion is via multiple tethers, varying from 2 to 5 in numbers. These numbers are, however, significantly less than the number of microvilli, often up to 35, which are available within the cell/substrate contact area, and are observed to form bonds. Increasing the shear rate by a factor of five only doubled the number of tethered microvilli from an average value of 2.5 to 5. Though multiple tethers are observed in most of our simulations, we also observe that a single tether is often sufficient to support rolling.

We next examine the average number of selectin bonds formed between a cell and the substrate in figure 4.23. Note that we assume 50 PSGL-1 ligands on each microvillus tip. In contrast, we observe that only about half of them, at most, forms bonds. The force on these bonds ranges from 0–100 pN. However, even less than half of these bonds carry a force > 10 pN. Thus we consider a bond to be ‘stretched’ when the force on it is > 5 pN. The average number of total bonds are in the range of 100–500, and it increases with increasing shear rate and membrane compliance due to increased cell-surface contact area resulting in more bound microvilli. These values agree well with that estimated by Jadhav *et al.* [35]. Remarkably, however, the number of stretched bonds lies in the range 20 to 80 which also increases with increasing shear rate, due to increasing number of tethers, but does not depend on membrane compliance due to the fact that the

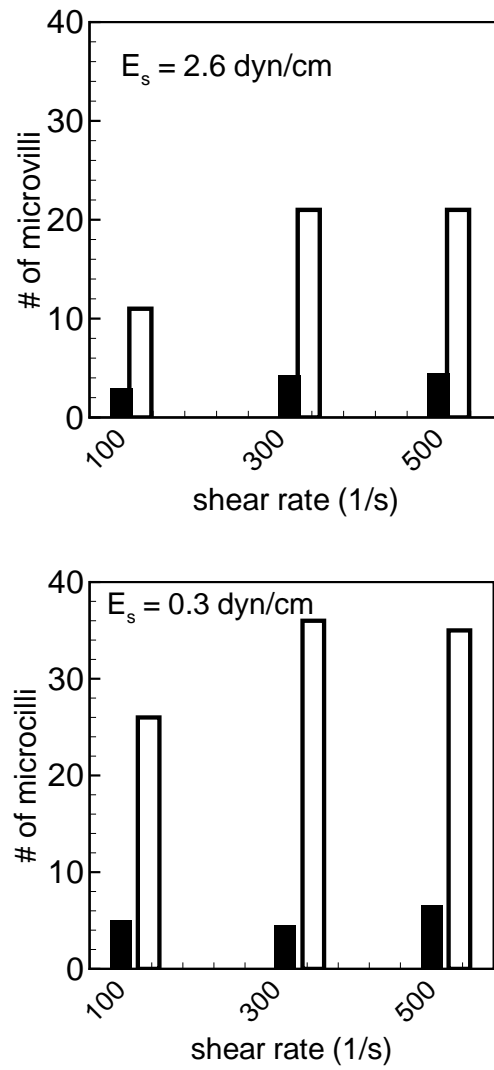


Figure 4.22: Average number of total bound microvilli (open bars) and tethered microvilli (solid bars) as functions of shear rate and cell compliance.

number of tethers did not increase appreciably with increasing cell deformability. Per microvillus, only 9-14 bonds are predicted to be significantly stretched, which agrees well with the measurements of Chen & Springer [14].

Together figures 4.22 and 4.23 show that the number of bonds per microvillus depend on the membrane stiffness and shear rate. The dependence of multiple bonds per microvillus, and the pause time (refer figure 4.10) on cell compliance, are noteworthy in the context of experimental estimation of bond dissociation rates. Bond dissociation rates are often measured based on the pause times obtained from leukocyte rolling in flow chamber. However, cell deformation cannot be easily controlled in such experiments. Assuming single bond dissociation, the Bell model [55] is fit to the measurements to obtain the bond dissociation rate. Direct measurements using atomic force microscopy or laser trap yielded different values than that obtained from flow chamber experiments (Rinko *et al.* [7]; Alon *et al.* [9]; Marshall *et al.* [58]) Our results suggest that two possible reasons for discrepancy are cell deformation and formation of multiple bonds per tether.

The maximum force on a tethered microvillus is shown in figure 4.24a as a function of shear rate and membrane stiffness. This force is obtained before a tether breaks away from the substrate. It ranges from about 80 to 420 pN. The peak force on a tethered microvillus predicted by our simulations is significantly above the force required for tether extrusion (61 pN) measured by Shao *et al.* [53]. Although we have not considered deformation of a microvillus in these cases, such a consideration would reduce the tether force (Caputo *et al.* [29]; Shao *et al.* [53];

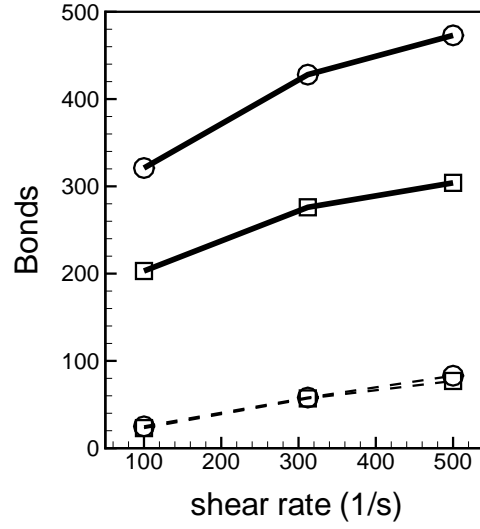


Figure 4.23: Average total bonds (solid lines) and stretched bonds (dash lines). \square — $E_s = 2.6$ and \circ — $E_s = 0.3$ dyn/cm.

Yu *et al.* [54]). In that case, tether extrusion may occur only at higher shear rate and membrane stiffness.

Similarly, the average bond rupture force is shown in figure 4.24b. The maximum and average rupture force of the bond was estimated to be 100 and 60 pN, respectively which are in the same range as measured recently by Marshall *et al.* [58] using atomic force microscopy. They are also in the same range as that obtained by Schmidtke and Diamond ([51], 86 to 172 pN at 100 to 250s⁻¹). We observe that the bond force increases with increasing shear rate and membrane stiffness. Dependence of bond force on the cell deformability is also in agreement with previous in vitro studies using untreated neutrophil, and ligand-coated microbeads (Park *et al.* [11]). The bond force was measured to be 500 pN for microbeads and 124 pN for neutrophil at a shear rate 100s⁻¹ (see also Smith *et*

al. [10]). Significantly reduced bond force for neutrophil compared to that for microspheres was attributed to microvilli elongation. In contrast, microvilli extension was not considered for these simulations. Our result, therefore, suggests that cell deformation also helps reducing the bond force and prolonging the bond lifetime.

It is important to note that the hydrodynamic shear and cell deformation have competing effects on bond dissociation and subsequently on microvilli breakage. Force on an individual bond increases, and hence the bond lifetime decreases, with increasing shear. Despite rapid bond dissociation at a high shear, leukocyte rolling is stabilized by cell deformation via two pathways. First, increased cell/substrate contact area causes more microvilli to be accessible for bond formation. Increased number of tethers with increasing shear alleviates the force on individual bond. The second mechanism is the reduction of the hydrodynamic drag on a deformed cell which also reduces bond force and hence the dissociation rate.

Total adhesion force between the cell and the substrate is shown in figure 4.25 as a function of shear rate and membrane stiffness. The adhesive force obtained in our simulations ranges from about 100 to 750 pN for shear rates 100–500s⁻¹. In comparison, the adhesive force estimated by House & Lipowsky [50], based on in vivo measurements, ranges from 110 to 7610 pN for shear rates 200–2500s⁻¹. The adhesive force increases with increasing membrane stiffness, partly due to increased hydrodynamic drag on less compliant cells. The adhesive force also increases with increasing shear rate. The peak force on the microvillus from our

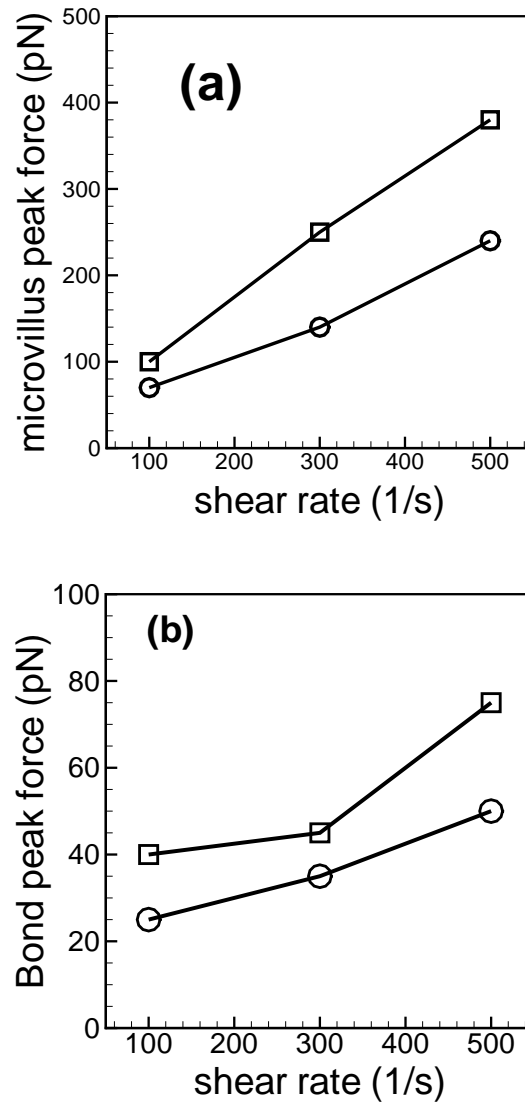


Figure 4.24: Average peak force on (A) microvilli and (B) bond. $-\square-$ $E_s = 2.6$ and $-\circ-$ $E_s = 0.3$ dyn/cm.

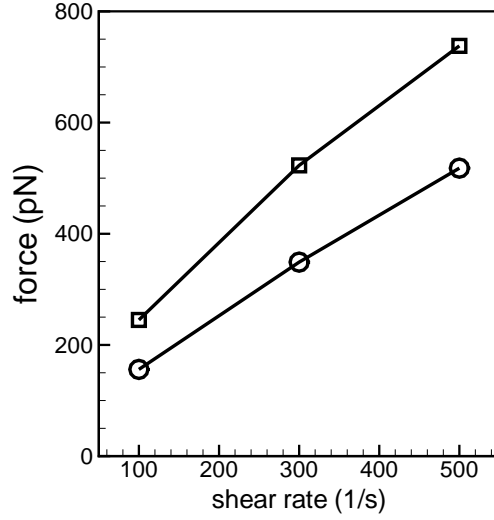


Figure 4.25: Average total adhesion force as a function of shear rate for different membrane stiffness. \square — $E_s = 2.6$ and \circ — $E_s = 0.3$ dyn/cm.

simulations (refer figure 4.24) are comparable to the total adhesive force. This again substantiates the fact that often one tether is sufficient to support rolling.

It is of interest to examine how the adhesive force is distributed within the cell-surface contact area. This is shown in figure 4.26 for a representative case at $\dot{\gamma} = 500\text{s}^{-1}$ and $E_s = 0.3$ dyn/cm. In our simulations, bonds are assumed to form at the microvilli tips only. Hence the distribution of the adhesive force is not continuous, rather discrete. In figure 4.26a, we show the 3D representation of the force on the microvilli along with their location on the cell surface. Figure 4.26a show how the adhesive force is distributed among all 20 microvilli that are present in the contact area. Nearly 90% of the total adhesion force is concentrated in three microvilli (marked by arrows in figure 4.26b) which form tethers in the rear end of the cell. The force on each of these tethered microvilli ranges from 200

to 400 pN, while that on each of the remaining 17 microvilli is in the range 0–20 pN. Our results, therefore, predict that the microvilli in the rear end of the cell would develop tether extrusion, while those in the remaining part of the contact area would at most undergo elastic tension.

4.4.2 Effect of microvilli presentation

We consider two different microvilli distributions, $N_{mv} = 21$ and 155, where N_{mv} is the number of total microvilli on the entire cell surface. The microvilli are randomly distributed on the cell surface.

Figure 4.27a shows average velocity as a function of shear rate, and microvilli distribution. The average velocity increases with decreasing N_{mv} . At $N_{mv} = 21$, the average rolling velocity ranges from about 20 to 112 $\mu\text{m/s}$, whereas at $N_{mv} = 155$, it ranges from 3 to 11 $\mu\text{m/s}$. At lower shear, the rolling velocity does not change significantly with varying N_{mv} but it depends strongly at higher shear. The effect of membrane stiffness with varying microvilli distribution on the rolling velocity is shown in figure 4.27b. At higher N_{mv} , the average velocity does not depend on the membrane stiffness, but at lower N_{mv} , it strongly varies with membrane stiffness.

The average step size of a rolling leukocyte obtained from our simulations is shown in figure 4.28. The step-size strongly depends on N_{mv} . For $N_{mv} = 155$, the average step size is in the range 0.2–0.6 μm , and it does not strongly depend on shear rate. For $N_{mv} = 21$, the step size increases significantly due to more sparse

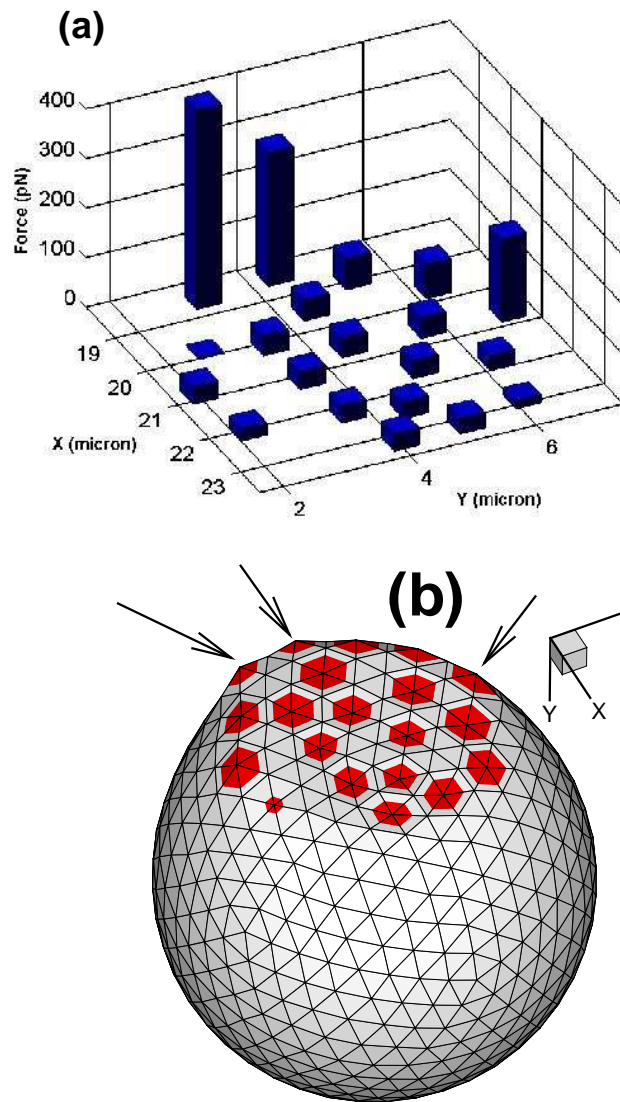


Figure 4.26: (a) Distribution of adhesion force among all bound microvilli in the cell/substrate contact area, and (b) distribution of bound microvilli over the cell surface. The arrows indicate three microvilli forming tethers.

distribution of microvilli. The step size also decreases with increasing shear rate. In vivo measurement by Zhao *et al.* [52] obtained step size of $2\ \mu\text{m}$, while in vitro measurements by Alon *et al.* [56] for L-selectin mediated rolling estimated $3\text{--}4\ \mu\text{m}$. These data, together with our prediction of $0.5\text{--}4\ \mu\text{m}$ step-size for P-selectin mediated rolling suggested that the step-distance is independent of the nature of receptor-ligand complex, and is dependent on the microvilli distribution. Interestingly, on the contrary, our simulations also predict that the average pause time does not depend on the microvilli distribution, but depends on the shear rate and cell deformability (refer figure 4.10).

Figure 4.29 shows the RMS (root-mean-square) of instantaneous rolling velocity as a function of shear rate and N_{mv} . The RMS of the axial velocity shows a strong dependence on shear rate, and microvillus distribution. The RMS increases with increasing shear rate. On the contrary, it decreases with increasing number of microvilli. At $N_{mv} = 155$, the RMS does not change appreciably w.r.t. shear rate, though it shows an increasing trend. At $N_{mv} = 21$, several-folds increase in the RMS is observed at higher shear rate. Hence, the cell rolls more stably with the denser population of microvilli, and at lower shear rate.

We conclude that not only the stochastic formation and breakage of selectin bonds, but also the presentation of the microvilli affects the fluctuating motion of a leukocyte. By considering two different microvilli distributions, here we showed that the average rolling velocity and fluctuations are higher for the sparse distribution. The higher rolling velocity is caused by increasing step size which

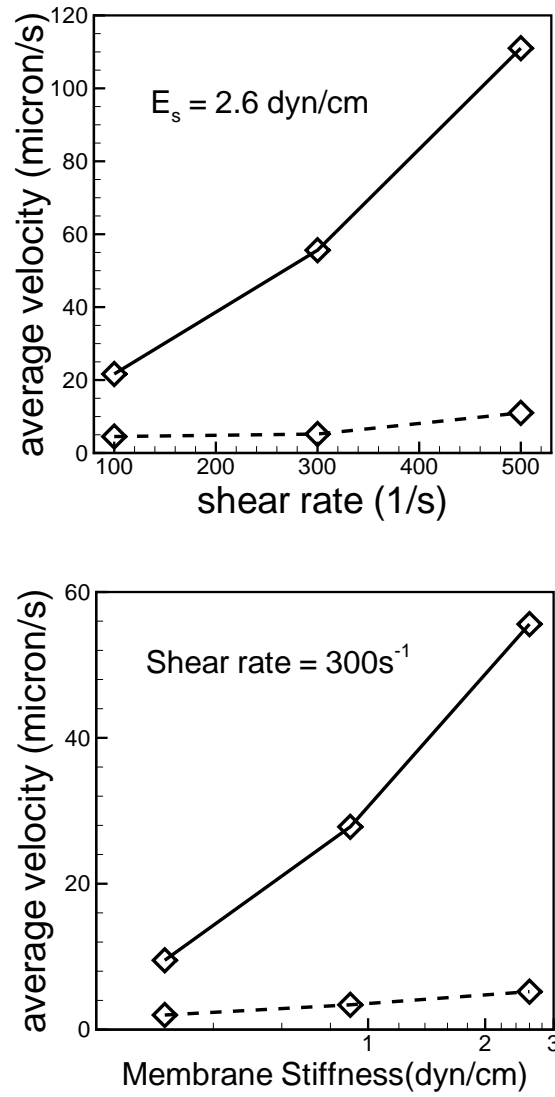


Figure 4.27: Effect of microvilli presentation on the average velocity as a function of (a) shear rate at a constant $E_s = 2.6$ dyn/cm, and (b) membrane stiffness at a constant shear rate of 300s^{-1} . — $N_{mv} = 21$, and - - - - $N_{mv} = 155$

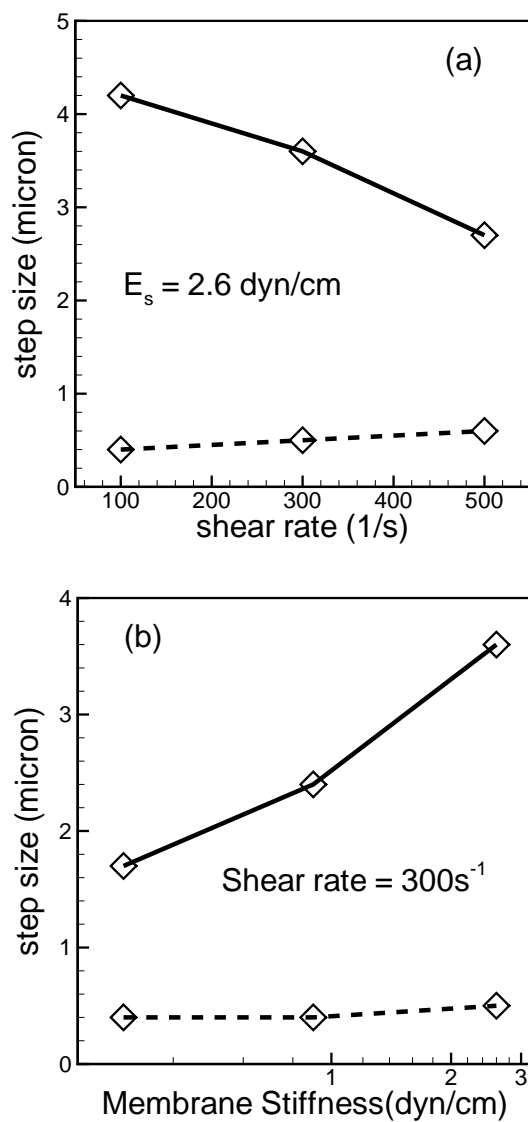


Figure 4.28: Effect of microvilli presentation on step size as a function of (a) shear rate at a constant $E_s = 2.6$ dyn/cm, and (b) membrane stiffness at a constant shear rate of 300s^{-1} . — $N_{mv} = 21$, and - - - - $N_{mv} = 155$

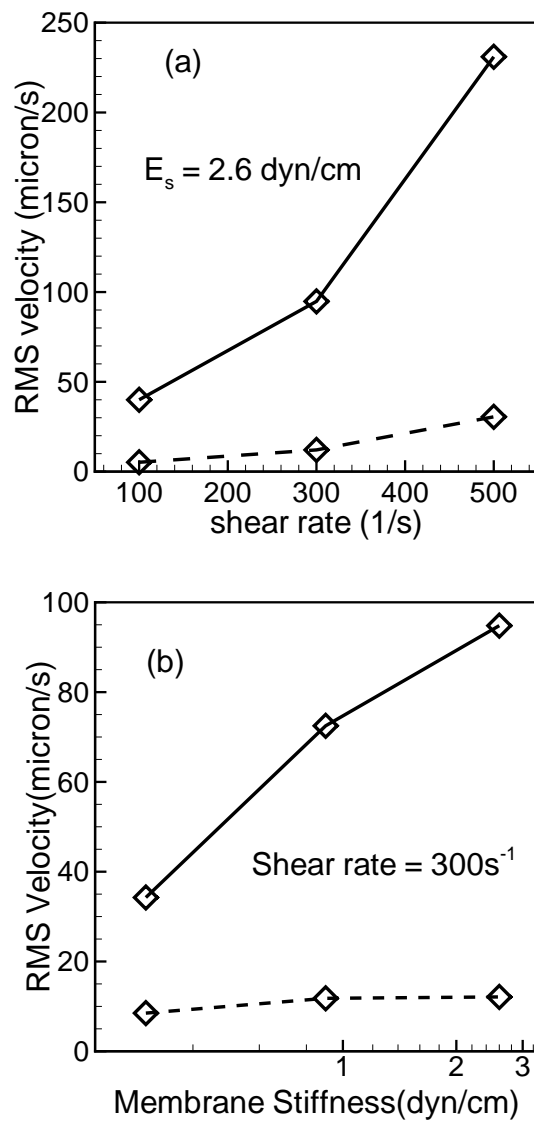


Figure 4.29: Effect of microvilli presentation on the RMS fluctuation of axial velocity as a function of (a) shear rate at a constant $E_s = 2.6$ dyn/cm, and (b) membrane stiffness at a constant shear rate of 300s^{-1} . — $N_{mv} = 21$, and - - - $N_{mv} = 155$.

seems to correlate with the inter-microvilli distance.

Chapter 5

Effect of Leukocyte Adhesion on the Flow Pattern in Microvessels

5.1 Introduction

As discussed in Chapter 1, the leukocyte rolling adhesion causes several changes in the surrounding flow environment. The flow resistance is expected to increase due to the reduced lumen area caused by the leukocyte adhesion. The streamlines surrounding the leukocyte are expected to be deflected, thereby altering the trajectory of the surrounding blood cells. The fluid drag is expected to reduce due to the ‘streamlined’ shape of the leukocyte. While a lot has been learned from the aforementioned computational models in terms of flow resistance and fluid drag, two key features of leukocyte adhesion, such as cell deformation and slow rolling, were neglected therein (Brooks *et al.* [63]; Chapman & Cokelet [67-69]; Das *et al.* [16]; Gaver & Kute [17]). While circulating leukocytes maintain a spherical shape, adherent leukocytes assume the shape of a tear-drop (Dong *et al.* [12]; Damiano *et al.* [23]; Dong & Lei [30]). Deformation of an adherent leukocyte increases the free lumen area and hence reduces the resistance to blood flow. Thus it is likely

that the flow resistance is overpredicted by the model of Chapman & Cokelet [67-69]. Deformation also reduces the shear stress, and the fluid drag acting on the cells, and hence increases the lifetime of the selectin bonds. Therefore, accurate prediction of the flow resistance and fluid drag is important in understanding the mechanics of cell adhesion, and the micro-environment surrounding the cells.

In this chapter, we present results on the simulation of rolling adhesion of multiple deformable leukocytes over P-selectin coated surface in a parabolic shear flow. We consider the effect of leukocyte adhesion on the flow pattern, and compare our results with previous *in vivo* measurements. Then we address the role of cell deformability, cell concentration and rolling velocity on the flow resistance and fluid drag.

5.1.1 Flow pattern

First, we consider the changes in the flow pattern caused by the adherent leukocytes. We compare our results with those of King *et al.* [74] who measured the flow streamlines around adherent leukocytes in post-capillary venules of diameter 20–40 μm . Figures 5.1a and b show the streamlines for 1 and 6 adherent cells, respectively, per 100 μm of vessel length. Quantitative comparison is obtained by computing the average deflection angle of the trajectories of many tracer particles which is defined as (King *et al.* [74])

$$\phi_{avg} = \frac{1}{L} \int \left| \tan^{-1} \left(\frac{\Delta y}{\Delta x} \right) \right| dL \quad (5.1)$$

where L is the arc length of individual trajectory, and Δx and Δy are the incremental displacements in horizontal and vertical directions, respectively. In our simulations, we released about a thousand tracer particles, and tracked their trajectory using second order interpolation and time advancing schemes. The values of ϕ_{avg} obtained from our simulations are shown in figures 5.1c–e as a function of the number of adherent cells, the channel height, shear rate, and E_s . First, consider the effect of channel height as shown in figure 5.1c. The deflection angle decreases with increasing channel height, in agreement with King *et al.*'s [74] measurement. We estimate the values of ϕ_{avg} in two ways: $\phi_{avg,mid}$ which considers only the tracers moving in the XY plane passing through the center of the cell, and $\phi_{avg,whole}$ which is based on all tracers in the entire flow domain. Since the deflection of the streamline is maximum in the central plane, $\phi_{avg,mid}$ is expected to be higher than $\phi_{avg,whole}$. In figure 5.1c, we plot both $\phi_{avg,mid}$ and $\phi_{avg,whole}$ as a function of channel height. For $\phi_{avg,mid}$, our data is in the range 0.1–0.45 (figures 5.1c, d, e), while for $\phi_{avg,whole}$ it is 0.05–0.23. The former is expected to be closer to any experimental measurement of ϕ_{avg} in vessels with circular cross-section which have more blockage than a channel. The values obtained in King *et al.*'s [74] measurements were in the range 0.1–0.8. Hence, our predicted $\phi_{avg,mid}$ values are in closer agreement with the in vivo measurements.

Effect of shear rate and number of adherent cells is shown in figure 5.1d. Similar to in vivo data, our results show increasing trend of ϕ_{avg} with increasing WBC concentration. However, contrary to the in vivo measurements of King *et*

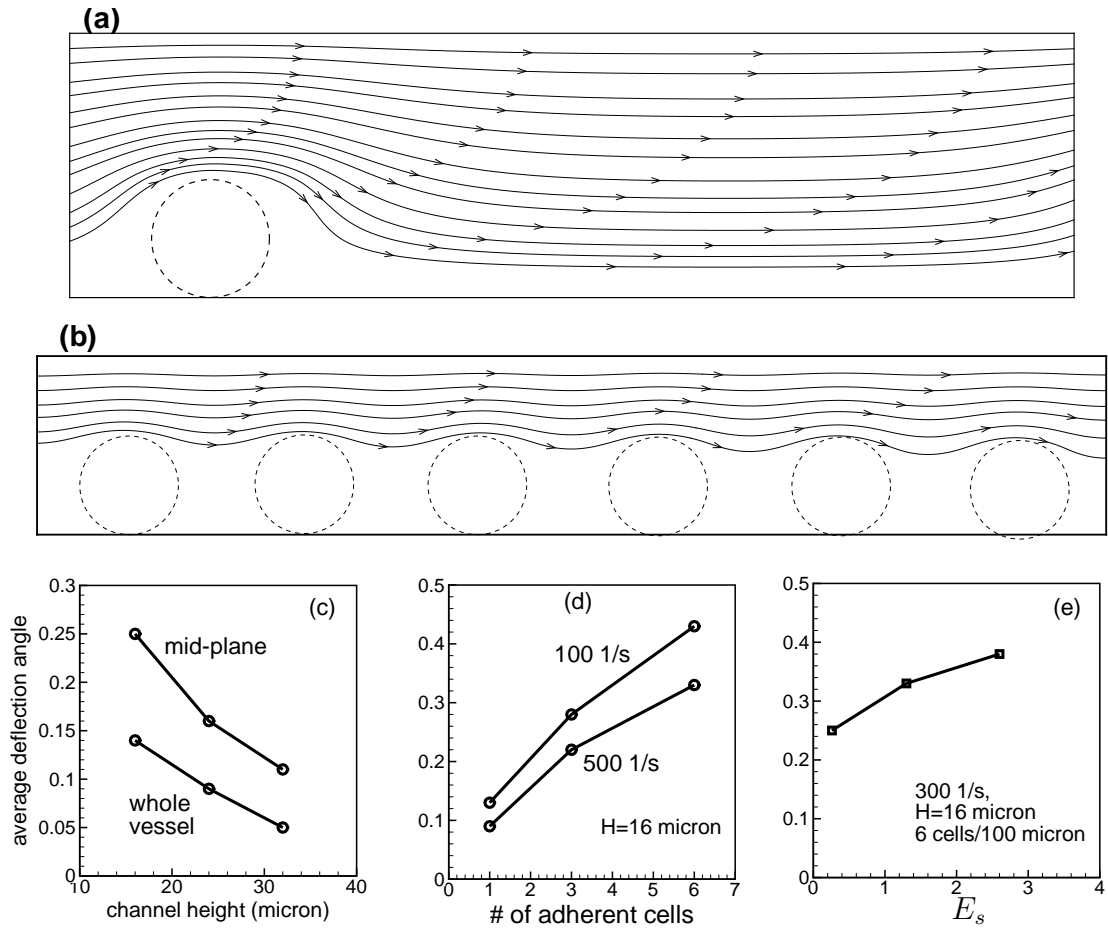


Figure 5.1: Streamlines in 16 μm channel for (a) one and (b) six adherent cells per 100 μm channel length. Average deflection angle of tracers as a function of (c) channel height, (d) number of adherent cells and shear rate, and (e) E_s . In (c) two curves represent data obtained by considering all tracer particles in the whole vessel, and by considering those flowing through the mid-plane passing through the centers of the cells. In (d) two curves represent two different shear rates 100 and 500 s^{-1} .

al.'s [74], we observe a decreasing trend of ϕ_{avg} with increasing shear rate. The discrepancy is likely due to increased cell deformation with increasing shear rate which results in reduced deflection of the streamlines in the simulations. We also show the effect of cell deformability on ϕ_{avg} in figure 5.1e, which shows that ϕ_{avg} increases with increasing membrane stiffness.

Mean fluid velocity profiles are shown in figure 5.2 as a function of E_s , shear rate, vessel size, and number of adherent cells. Also shown is the parabolic velocity profile. Presence of leukocytes reduces the maximum velocity, and causes significant departure from the parabolic profile. The velocity profile is asymmetric across the channel. The maximum velocity decrease, and the asymmetry increases with increasing cell rigidity, increasing number of adherent cells, decreasing shear rate, and decreasing channel height. The location of maximum velocity moves increasingly towards the opposite wall resulting in higher wall shear stress with decreasing cell deformability, decreasing shear rate, increasing cell concentration, and decreasing channel height.

5.1.2 Flow resistance and fluid drag

Next we present the flow resistance due to rolling leukocytes. We consider microchannels of height 10, 16 and 25 μm , and length 100 μm , and the number of rolling leukocytes varying from one to ten per 100 μm of channel length. The flow resistance is calculated using the relation

$$R = \Delta P / Q \quad (5.2)$$

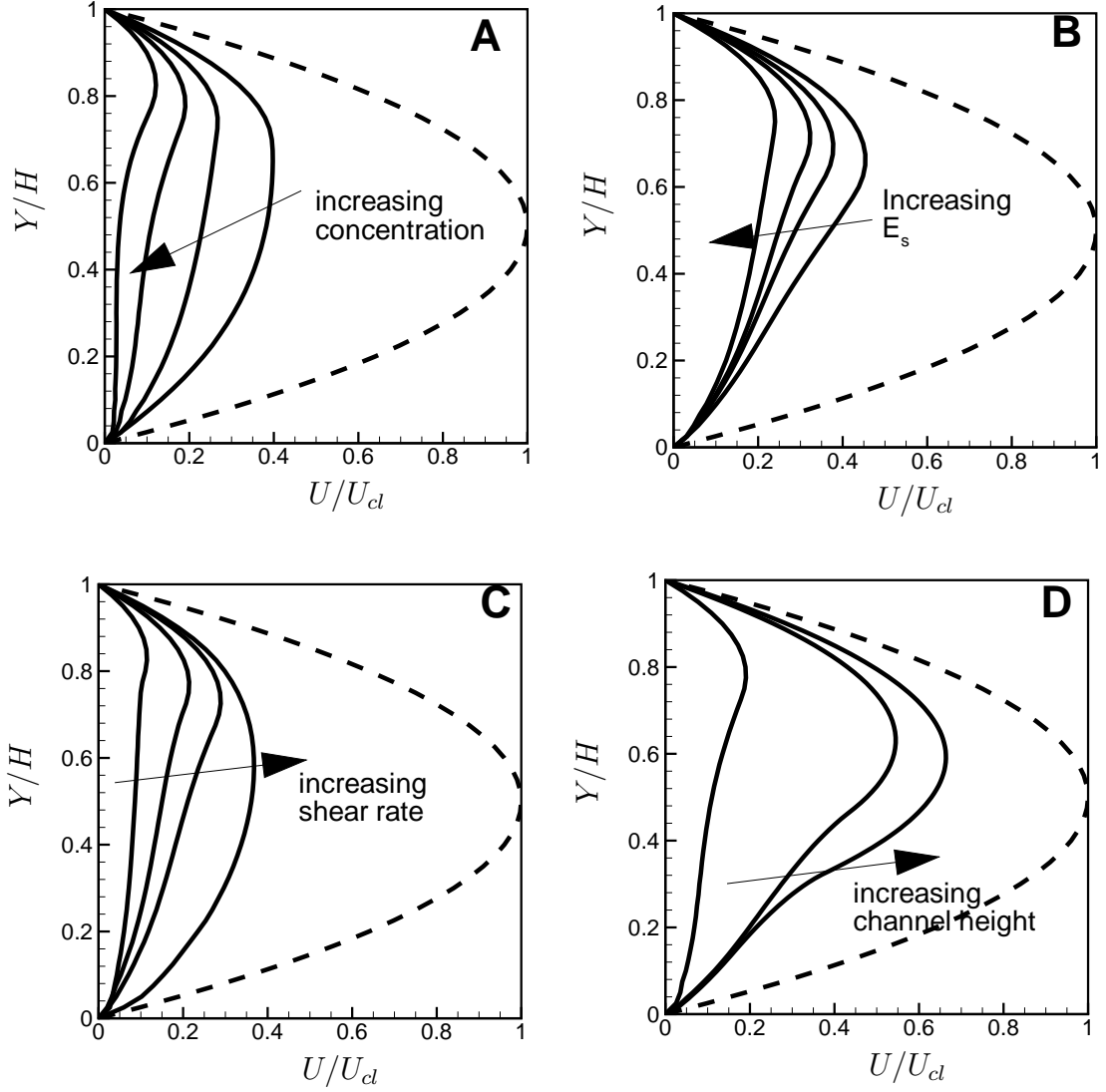


Figure 5.2: Mean fluid velocity across the channel as a function of (A) number of adherent cells, (B) E_s , (C) shear rate, and (D) channel height. Dash line is the parabolic velocity in absence of the cells, and solid lines are the results with the cells. The arrows indicate the direction in which the relevant parameter increases. In (A) the number of cells increases as 1, 2.5, 5, 10 per 100 μm length in a 10 μm channel at 300s^{-1} shear rate and $E_s = 0.9 \text{ dyn/cm}$. In (B) E_s increases as 0.05, 0.15, 0.3, 0.9 dyn/cm in a 10 μm channel at 300s^{-1} shear rate. In (C) shear rate increases as 50, 100, 300, 500s^{-1} . In (D) channel height increases as 10, 16, and 25 μm .

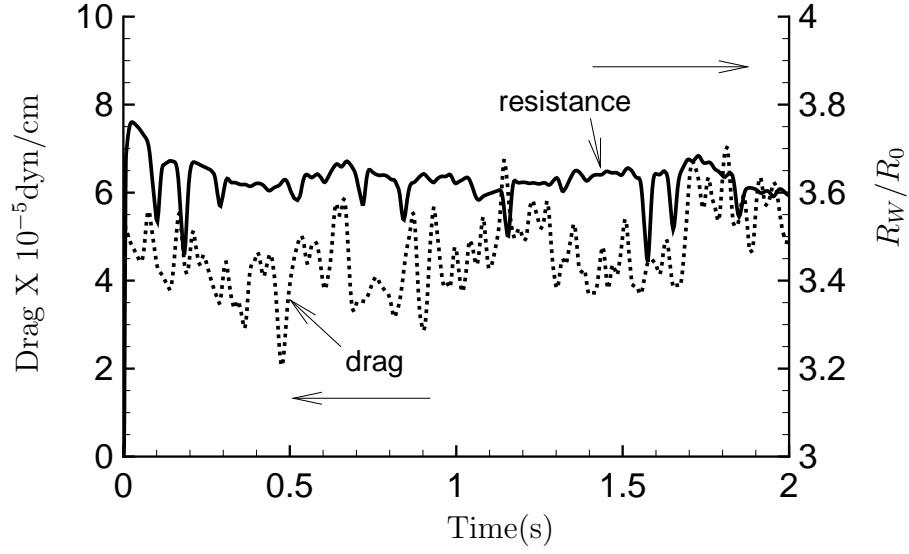


Figure 5.3: Instantaneous fluid drag (dotted line, left axis), and relative flow resistance (solid line, right axis) for a representative case of 6 WBC/100 μm length of a 16 μm channel and $E_s = 2.6 \text{ dyn/cm}$.

where ΔP is the pressure drop over the length of the vessel, and Q is the flow rate. In absence of the cells, the resistance is denoted by R_0 , while that in presence of the adherent cells is denoted by R_W . We consider the relative resistance defined as R_W/R_0 . The fluid drag is computed by integrating the pressure and viscous stresses over the cell surface and taking the X component.

The history of R_W/R_0 and fluid drag for one representative simulation is presented in figure 5.3 to show that these quantities also attain quasi-steady value in our simulations. As expected, large fluctuations in fluid drag and relative resistance are observed during the course of the leukocyte rolling motion. The fluid drag shows more fluctuations compared to R_W/R_0 : the rms fluctuations is 91% of the mean for the fluid drag, whereas it is 42% for R_W/R_0 .

The time-averaged values of R_W/R_0 for all simulation runs are presented in figure 5.4 for 10–25 μm channels. The symbols in this figure represent the values obtained in the present simulations. Our results are compared with the computational modeling of Chapman & Cokelet [67-69] who modeled adherent leukocytes as rigid static spheres truncated at the base. The in vivo measurements obtained by House & Lipowsky [50] are also shown. For a given number of cells, multiple values of R_W/R_0 , as obtained by our simulations, are due to variation in cell deformability, and will be explored later.

We note in figure 5.4, that R_W/R_0 increases with increasing number of adherent cells, in agreement with the prediction by Chapman & Cokelet [69] and in vivo measurements by House & Lipowsky [50]. However, the computed values of R_W/R_0 from our IBM simulation are often significantly less than those obtained by Chapman & Cokelet [69]. The difference increases with increasing number of leukocytes, and with decreasing channel height. For example, in the 10 μm vessel, Chapman & Cokelet [69] predicted $R_W/R_0 \approx 15$ for 5 adherent cells per 100 μm length. Our results predict that R_W/R_0 ranges from 6.5 to 13, depending on cell deformation. In figure 5.4c, we also show the in vivo data obtained by House & Lipowsky [50] for 25 μm vessel (shown by a dash line), which are in good agreement with our prediction.

Next we consider the effect of E_s on the flow resistance as shown in figure 5.5 for 10 μm channel, and in figure 5.6 for 16 and 25 μm channels. We compare our results with those of Chapman & Cokelet [69] which are shown by dash

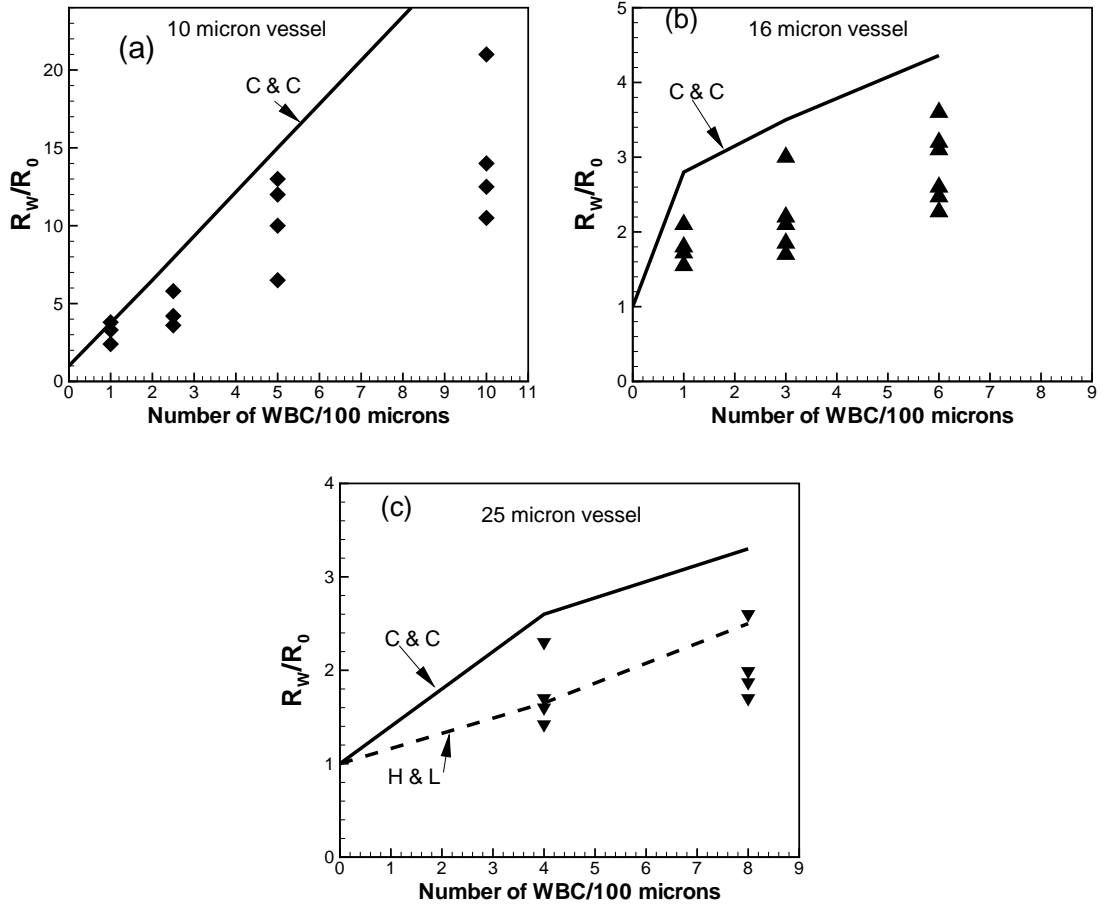


Figure 5.4: Relative resistance R_W/R_0 in 10, 16 and 25 μm channels for various number of adherent cells per 100 μm length. The solid line is the result from Chapman & Cokelet [69] (indicated by C & C here and in subsequent figures), the dash line is the in vivo result of House & Lipowsky [50] (indicated by H & L here and in subsequent figures). The symbols represent the present result. Multiple values of R_W/R_0 for a given number of adherent cells are due to the variation in shear rate, E_s and rolling velocity. Here R_W/R_0 is the ratio of the flow resistance with and without the adherent leukocytes. Data from all computation are shown to emphasize the recurring theme of the paper, that is, R_W/R_0 is dependent not only on the number of adherent cells, but also on shear rate, E_s and rolling velocity.

lines. Again, our results predict significantly lower values of the flow resistance due to adherent leukocytes compared to those predicted by Chapman & Cokelet. As an example, Chapman & Cokelet [69] predicted $R_W/R_0 \approx 4$ and 15, for 1 and 5 adherent cells, respectively, per 100 μm vessel length. In contrast, our predicted values range from 1.8 to 2.6, and 5.5 to 8.3. Our model predicts that a compliant cell elongates more in the flow direction, and attains a ‘tear-drop’ shape. Consequently, free luminal area increases resulting in reduced flow resistance. In comparison to the 3D modeling of Chapman & Cokelet [67-69], who modeled leukocytes as rigid spheres, our results predict much lower values of flow resistance, often reduced by a factor of two. In contrast, our results show closer agreement with the in vivo data of House & Lipowsky [50]. In Chapman & Cokelet [67-69], the cell-wall contact area and the L/H ratio were specified as input parameters as 12.57 μm^2 and 1.075, respectively. In our model, the cell shape, and the contact area were obtained as parts of the solution. In all of our simulations we obtained higher contact area and lower cell height, and hence more free lumen area than those assumed in Chapman & Cokelet. Hence our simulation, unlike Chapman & Cokelet’s result, predict that R_W/R_0 strongly depends on cell deformability, and decreases with decreasing membrane stiffness. In figure 5.5a, we note that as E_s varies from 1.57 to 0.025 dyn/cm, R_W/R_0 decreases by nearly 70% for 5 cells/100 μm . The dependence of R_W/R_0 on E_s appears to be more at higher cell concentration.

Effect of shear rate on R_W/R_0 is shown in figure 5.5b. The flow resistance

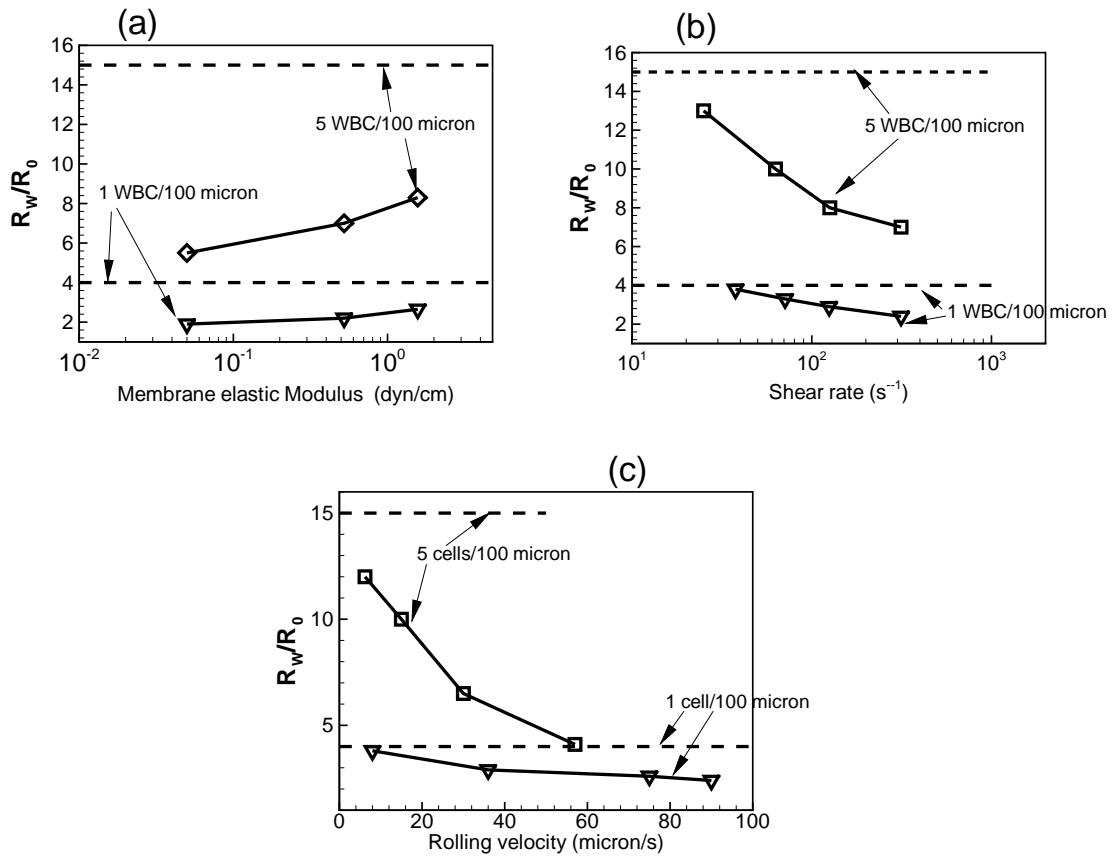


Figure 5.5: Effect of E_s , number of adherent cells, shear rate, and rolling velocity on R_w/R_0 . The channel height is $10 \mu\text{m}$. Dash lines without symbols are results of Chapman & Cokelet. Lines with symbols are the present results.

decreases by a factor of two as the shear rate increases from 25 to 310s^{-1} . The dependence of R_W/R_0 on the shear rate is more prominent at higher cell concentration. Interestingly, our prediction of R_W/R_0 approaches that of Chapman & Cokelet at lower shear rates when cell deformation is reduced.

We consider another set of simulations in figure 5.5c where the reaction rates k_r^0 and k_f^0 are varied to obtain different rolling velocity while shear rate, and E_s are kept fixed at 300s^{-1} and 0.5 dyn/cm , respectively. This way, the cell deformation is maintained constant, but the rolling velocity is changed. The figure shows that R_W/R_0 depends on the leukocyte rolling velocity irrespective of cell deformation. R_W/R_0 drops by a factor of 3 (from 12 to 4), as the rolling velocity increases from 6 to $57\text{ }\mu\text{m/s}$. As the rolling velocity approaches zero, our results approach those of Chapman & Cokelet [69]. These simulations predicted that the flow resistance also depends on the rolling velocity, and it decreases with increasing rolling velocity. The discrepancy between the present results and those of Chapman & Cokelet [67-69] could also arise due to rolling cells versus static cells considered in the two cases. The non-zero rolling velocity results into a reduced flow resistance as less energy is spent by the surrounding fluid with increasing rolling velocity. It should be noted that Chapman & Cokelet considered flow in circular tube, whereas we consider flow through channels. The choice of this geometry is because of its relative simplicity in using the IBM technique. This geometric difference definitely affects the result, though while comparing our results with those of Chapman & Cokelet, we have considered

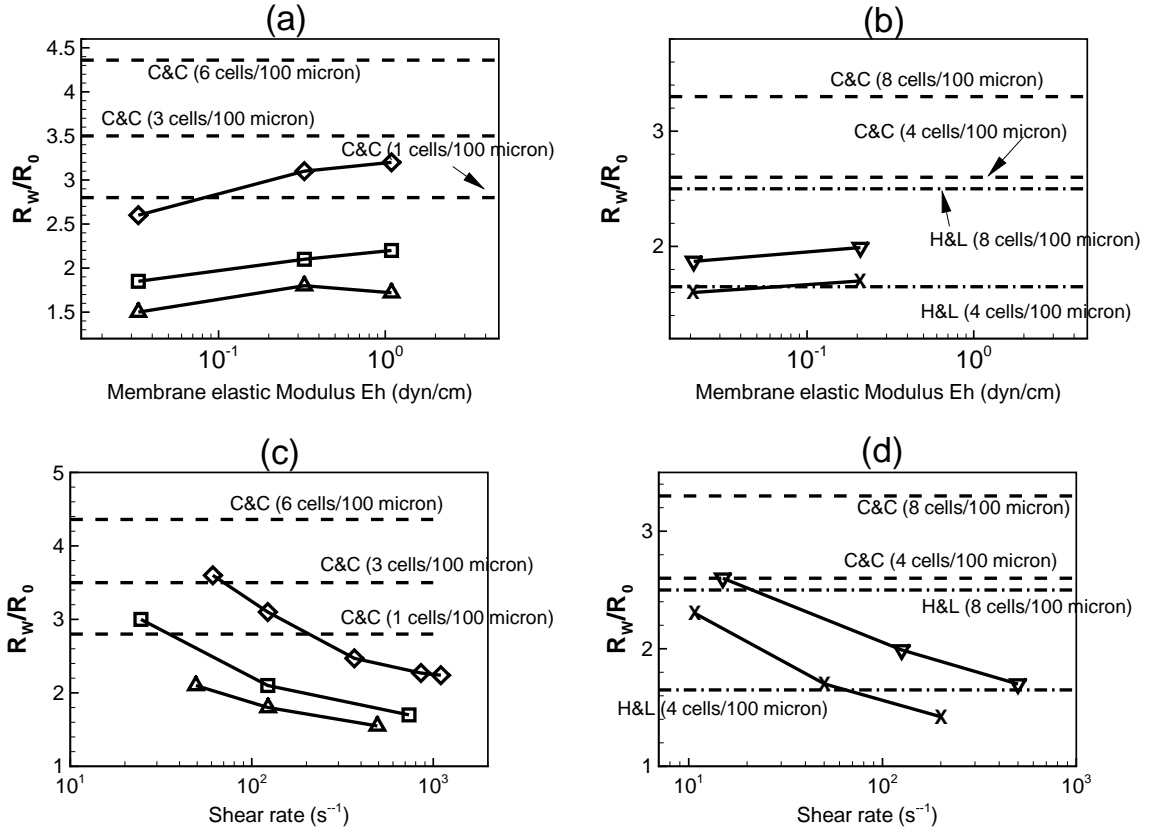


Figure 5.6: Same as in figure 5.5 but for 16 μm , and 25 μm channels. Dash lines and dash-dot lines without symbols are results of Chapman & Cokelet, and in vivo measurements of House & Lipowsky, respectively. Lines with symbols are the present results: Δ – 1 WBC, \square – 3 WBC, \diamond – 6 WBC in 16 μm vessel, ∇ – 8 WBC, and \times – 4 WBC in 25 μm vessel, per 100 μm length.

hydrodynamically equivalent area in the two cases.

Results for 16 and 25 μm vessels are shown in figure 5.6. Overall, similar observation as that in figure 5.5 (for 10 μm vessel) can be made here. The values of R_w/R_0 as predicted by our IBM simulations are much lower than those predicted by Chapman & Cokelet [69]. The difference is often as high as 100%. We also compare our results with the in vivo data of House & Lipowsky [50] in 25 μm vessel. For four adherent cells per 100 μm length, our results match very

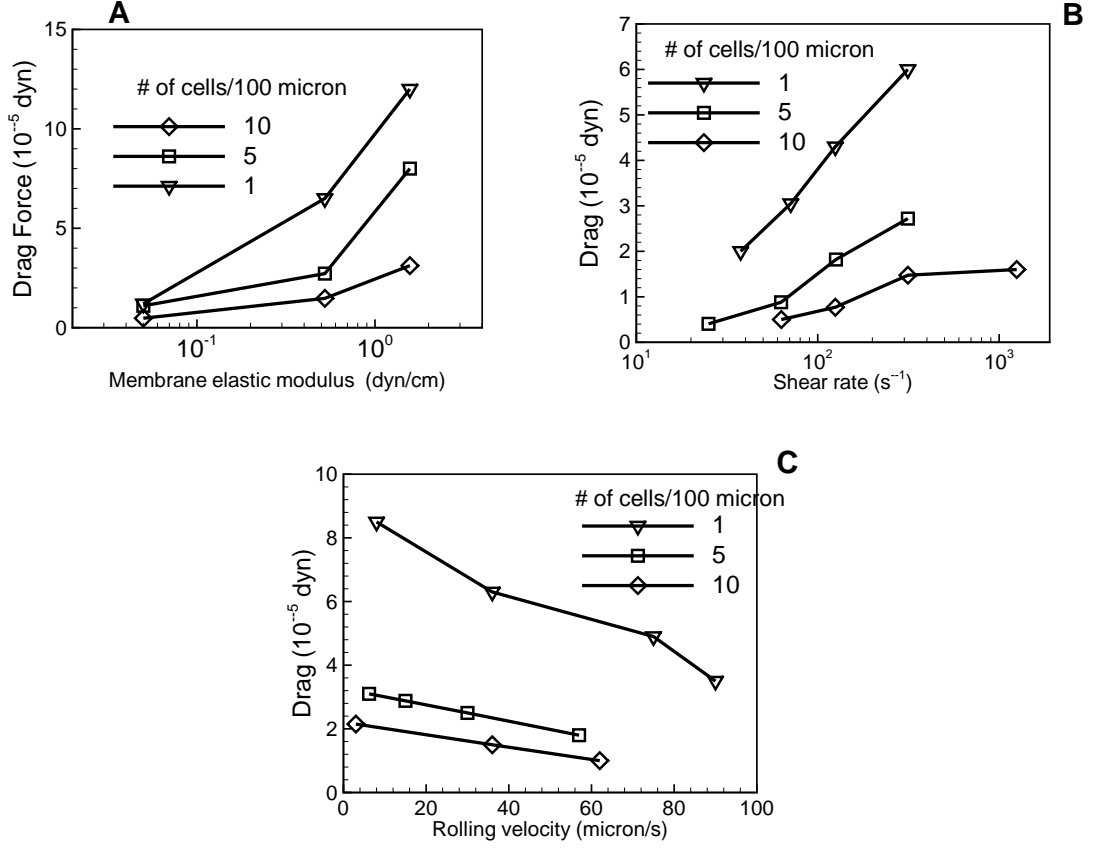


Figure 5.7: Fluid drag as a function of E_s , shear rate and rolling velocity for different number of adherent cells in a 10 μm channel. ∇ – 1 WBC, \square – 5 WBC, and \diamond – 10 WBC per 100 μm length.

well with that of House & Lipowsky. For eight cells, our results under-predict the flow resistance compared to that measured by House & Lipowsky.

The fluid drag acting on an adherent cell is shown in figure 5.7 as a function of shear rate, rolling velocity, and leukocyte concentration. Only data for 10 μm channel are shown. The drag obtained in our simulation is in the range $0.5\text{--}12 \times 10^{-5}$ dyn, which is comparable to previous in vivo measurements by House and Lipowsky [50] ($1.1\text{--}76.1 \times 10^{-5}$ dyn), Schmid-Schonbein *et al.* [1] ($0.4\text{--}23.4 \times 10^{-5}$ dyn), 2D computational modeling by Dong and co-workers [12,30,31]

($1.3\text{--}2.3\times 10^{-5}$ dyn), and 3D computational modeling by Khismatullin & Truskey ([34,35], $1\text{--}2\times 10^{-5}$ dyn for $20\text{ }\mu\text{m}$ channel at 8 dyn/cm^2 wall shear stress). Our predicted drag values are lower than those of Brooks & Tozeren [63] and Chapman & Cokelet [67-69] who considered rigid static spheres. Brooks & Tozeren predicted fluid drag 2×10^{-4} dyn which is an order of magnitude higher than that obtained in our simulations. Chapman & Cokelet predicted 34.5×10^{-5} dyn on a single rigid cell adherent in $10\text{ }\mu\text{m}$ vessel, which is also higher than the maximum drag obtained by us (12×10^{-5} dyn in figure 5.7a). The discrepancy is again due to cell deformation and rolling considered in our cases.

Figure 5.7 shows that fluid drag increases with decreasing number of cells, increasing membrane stiffness, increasing shear rate, and decreasing rolling velocity. An order of magnitude increase in drag (1.1 to 12×10^{-5} dyn) is observed as E_s increases from 0.05 to 1.57 dyn/cm (figure 5.7a). We further note that the rate of decrease of drag with decreasing E_s is not uniform, and the curves in figure 5.7a seem to approach a plateau toward lower values of E_s as the cell deforms more. This can be understood by looking at the normal and shear stress contributions to the total drag separately. Contribution from the normal stress to the total drag is much lower than that from the shear stress (also observed by Brooks & Tozeren [63]). As the cell elongates further, the maximum value of the shear stress, which occurs on the cell membrane farthest from the bottom surface, decreases resulting in a decrease in the drag. However, at the same time, more surface area is exposed to the fluid stress, resulting in a slow decrease in drag.

The decrease in fluid drag with an increase in adherent leukocytes is in agreement with the results of Chapman & Cokelet [67-69] and Brooks & Tozeren [63]. For a cell of $24\text{ }\mu\text{m}$ diameter, Brooks & Tozeren predicted about 24% decrease in drag as the spacing between the cells decreases from 80 to $30\text{ }\mu\text{m}$. Chapman & Cokelet predicted nearly 50% decrease when leukocytes nearly touched each other. In comparison, our results in figure 5.7a showed a decrease in drag by a factor of 4 as the number of adherent leukocytes increased from one to ten per $100\text{ }\mu\text{m}$ length in a $10\text{ }\mu\text{m}$ channel. However, we also observed that the decrease in fluid drag (and hence shear stress on leukocyte surface) in presence of multiple leukocytes is dependent on cell deformability. Relative change in drag w.r.t cell concentration is more prominent for rigid cells than compliant cells. This observation in figure 5.7a is consistent with the results in figure 4.14a which showed that the reduction of rolling velocity w.r.t cell concentration is also more significant for rigid cells than for compliant cells.

Chapter 6

Conclusions of Thesis and Directions of Future Work

6.1 Summary of the thesis

Three-dimensional computational modeling and simulations are presented on the rolling motion of a deformable cell on an adhesive surface in shear flow. The problem is motivated primarily by the adhesive rolling motion of white blood cells in response to inflammation in the body, as well as similar motion by cancer cells (leading to cancer metastasis) and stem cells (stem cell homing). The methodology is based on an immersed boundary method to predict cell deformation, and a Monte Carlo simulation to model random formation and breakage of adhesion bonds between a cell and a substrate. The cells are modeled as ‘capsules’, that is liquid drops surrounded by elastic membranes that follow the neo-Hookean law for deformation. The adhesion bonds are assumed to behave as elastic springs under external loading. As such, the technique retains the multiscale and multiphysics nature of the problem. The technique allows us to resolve the complex coupling between the hydrodynamics, the deformation dynamics of the cell, and the biophysics of the adhesion bonds. In the thesis, we addressed the sequence

of events that are encountered in the multistep process of cell rolling, namely, the initial arrest of the cell, followed by its deformation and spreading on the substrate, and subsequent quasi-steady rolling motion. The major results from the thesis are summarized as follows.

First, we studied the hydrodynamic lift and drag acting on a free-flowing cell near a wall in shear flow. We hypothesized that the hydrodynamic lift plays a major role in dictating cell capture/escape. The lift is shown to increase with increasing cell deformability. We then studied the initial capture and subsequent spreading of a cell onto a substrate. We showed that a deformable cell takes longer time to flatten onto the substrate than a relatively rigid cell. We presented phase diagrams for cell capture/escape in terms of the critical bond strength ψ_c as a function Ca , ζ , and κ . The cell is captured on to the surface for $\psi > \psi_c$, and it escapes the surface otherwise. Unlike the lift which saturates with increasing Ca , the critical bond strength increases at a faster rate with increasing Ca . This result, which would not be obtained if the adhesion were modeled using force potential, was explained using the finite-rate bond kinetics, and the hydrodynamic lift. Continued simulations beyond the initial capture show that the cells roll on the adhesive surface in a ‘stop-and-go’ manner due to the stochastic nature of the formation and breakage of the adhesion bonds. The time-averaged rolling velocity decreases with increasing Ca . It also decreases with increasing ψ , but then reaches an asymptotic value. The asymptotic rolling velocity (corresponding to that at higher ψ) decreases with increasing Ca . The maximum rolling velocity

is also shown to decrease with increasing Ca . Finally, we provide a qualitative phase diagram in ψ - Ca plot showing the three regimes of escape, fast rolling, and slow rolling (firm adhesion). Qualitatively, the results can be summarized as follows: a relatively rigid cell can be captured at a lower adhesion strength, but would require much higher adhesion force to bring the cell to firm adhesion. A more deformable cell can be captured only at a higher adhesion strength, but once captured it would firmly adhere with a small increase in the adhesion strength.

We then specifically consider the ‘slow rolling’ of leukocytes as it is the case in inflammatory response. We consider P-selectin/PSGL-1 as the receptor/ligand pair. Thus the biophysical parameters are kept constant, while the shear rate and the elastic modulus of the cell membrane are varied. The simulations are continued for at least one second of leukocyte rolling during which the instantaneous quantities such as cell deformation index, cell/substrate contact area, and fluid drag remain statistically stationary. The characteristic ‘stop-and-go’ motion of rolling leukocytes, and the ‘tear-drop’ shape of adherent leukocytes as observed in experiments are reproduced by the simulations. We first consider the role of cell deformation and cell concentration on rolling characteristics. We observe that compliant cells roll slower and more stably than rigid cells. Comparison with experimental measurements (in vitro and in vivo) is presented. Our simulations agree with previous in vivo observation that the hydrodynamic interactions between nearby leukocytes affect cell rolling, and that the rolling velocity decreases inversely with the separation distance, irrespective of cell deformability. We also

find that cell deformation decreases, and the cells roll more stably with reduced velocity fluctuation, as the cell concentration is increased. However, the effect of nearby cells on the rolling characteristics is found to be more significant for rigid cells than compliant cells. Microvilli presentation is shown to affect rolling characteristics by altering the step size, but not pause times. Our simulations predict a significant sideways motion of the cell arising purely due to receptor/ligand interaction, and discrete nature of microvilli distribution. We then studied the biophysical characteristics of the adhesion bonds during the rolling process. Adhesion is seen to occur via multiple tethers, each of which forms multiple selectin bonds, but often one tether is sufficient to support rolling. The adhesion force is concentrated in only 1–3 tethered microvilli in the rear-most part of a cell. We also observe that the number of selectin bonds that hold the cell effectively against hydrodynamic shear is significantly less than the total adhesion bonds formed between a cell and the substrate. The force loading on individual microvillus and selectin bond is not continuous, rather occurs in steps. Further, we find that the peak force on a tethered microvillus is much higher than that measured to cause tether extrusion.

Next, we considered the effect of adherent cells on the surrounding flow pattern; specifically we addressed the changes in tracer dispersion in presence of adherent cells as the cell deformability and concentration are altered. We then address the effect of cell deformability and rolling velocity on the flow resistance

due to, and the fluid drag on, adherent leukocytes. While several earlier computational works have addressed this problem, two key features of leukocyte adhesion, such as cell deformation and rolling, were often neglected. Our results suggest that neglecting cell deformability and rolling velocity may significantly overpredict the flow resistance and drag force. Increasing the cell concentration is shown to increase the flow resistance and reduce the fluid drag. The reduced drag then results in slower and more stable rolling of the leukocytes with longer pause time and shorter step distance. But the increase/decrease in the flow resistance/fluid drag due to the increase in the cell concentration is observed to be more significant in case of rigid cells than compliant cells.

6.2 Future directions

Ever since the discovery of leukocyte rolling during inflammation in the 1980's (Schmid-Schonbein *et al.* [1]), the subject has gained increasing attention. The interest has also been fueled in recent days by the need to understand similar rolling motion performed by cancer cells and stem cells. Given the importance and complexity of the problem, it is impossible to model the entire adhesion cascade in one thesis. In terms of modeling, specifically, we have not addressed the elongation of the microvilli. It has been shown in experiments that microvilli deformation (Shao *et al.* [53]) and cell deformation both occur simultaneously.

Future work should consider inclusion of models to account for the microvilli deformation. In this thesis, we only addressed the motion of a single cell (or, multiple cells in synchronized motion). In vivo, however, there are cells interacting continually. It has been proposed that an already adherent leukocyte can trigger adhesion of more free-flowing leukocytes (Kunkel *et al.* [79]). Such a homotypic interaction between neighboring leukocytes may be an important topic of future research. Further, leukocytes in vivo are continually bombarded by fast-moving erythrocytes (Munn *et al.* [80]). It is not clear how the motion of the erythrocytes affects the rolling motion of the leukocytes. Further, in the thesis, we addressed tracer dispersion in presence of adherent leukocytes. The erythrocytes are also expected to disperse by the adherent leukocytes (Freund *et al.* [81]). This process has also applications in sickle cell disease, diabetes mellitus and malignant malaria, where red blood cells lose their deformability and occlude the narrow blood vessels in presence of the adherent leukocytes (Frenette [71]). Such problems, with direct applications to microhemodynamic disorders, can be addressed within the present computational framework.

References

- [1] G.W. SCHMID-SCHONBEIN, S. USAMI, R. SKALAK, and S. CHIEN. The interaction of leukocytes and erythrocytes in capillary and post-capillary vessels. *Microvascular Research*, 19:45–70, 1980.
- [2] M.A. LICHTMAN, and E. A. KEARNEY. The filterability of normal and leukemic human leukocytes. *Blood Cells*, 2:491–506, 1976.
- [3] E. EVANS, and B. KUKAN. Passive material behavior of granulocytes based on large deformation and recovery after deformation tests. *Blood*, 64:1028–1035, 1984.
- [4] H.P. TING-BEALL, D. NEEDHAM and R.M. HOCHMUTH. Volume and osmotic properties of human neutrophils. *Blood*, 81:2774–2780, 1993.
- [5] T.A. SPRINGER. Traffic signals on endothelium for lymphocyte recirculation and leukocyte emigration. *Annu. Rev. Physiol.*, 57:827–872, 1995.
- [6] M.B. LAWRENCE, and T.A. SPRINGER. Leukocytes roll on a selectin at physiologic flow rates: distinction from and prerequisite for adhesion through integrins. *Cell*, 65:859–873, 1991.
- [7] L.J. RINKO, M.B. LAWRENCE, and W.H. GUILFORD. The molecular mechanics of P- and L-selectin lectin domains binding to PSGL-1. *Biophysical Journal*, 86:544–554, 2004.
- [8] M.B. KIM, and I.H. SARELIUS. Role of shear forces and adhesion molecule distribution on P-selectin-mediated leukocyte rolling in postcapillary venules. *Am J physiol Heart Circ Physiol.*, 287:H2705–11, 2004.
- [9] R. ALON, D.A. HAMMER, and T.A. SPRINGER. Lifetime of the P-selectin-carbohydrate bond and its response to tensile force in hydrodynamic flow. *Nature*, 374:539–542. Erratum, 1995, *Nature*, **376**, pp. 86, 1995.
- [10] M.J. SMITH, E.L. BERG, and M.B. LAWRENCE. A direct comparison of selectin-mediated transient, adhesive events using high temporal resolution. *Biophysical Journal*, 77:3371–83, 1999.
- [11] E.Y. PARK, M.J. SMITH, E.S. STROPP, K.R. SNAPP, J.A. DIVIETRO, W.F. WALKER, D.W. SCHMIDTKE, S.L. DIAMOND, and M.B. LAWRENCE. Comparison of PSGL-1 microbead and neutrophil rolling: microvillus elongation stabilizes P-selectin bond clusters. *Biophysical Journal*, 82:1835–47, 2002.

- [12] C. DONG, J. CAO, E.J. STRUBLE, and H.H. LIPOWSKY. Mechanics of leukocyte deformation and adhesion to endothelium in shear flow. *Ann. Biomed. Eng.*, 27:298–312, 1999.
- [13] T. YAGO, A. LEPPANEN, H. QIU, W.D. MARCUS, M.U. NOLLERT, C. ZHU, R.D. CUMMINGS, and R.P. McEVER. Distinct molecular and cellular contributions to stabilizing selectin-mediated rolling under flow. *Journal of Cell Biology*, 158:787–99, 2002.
- [14] S. CHEN, and T.A. SPRINGER. An automatic braking system that stabilizes leukocyte rolling by an increase in selectin bond number with shear. *Journal of Cell Biology*, 144:185–200, 1999.
- [15] S. D. RODGERS, R. T. CAMPHAUSEN, and D. A. HAMMER. Sialyl Lewis(x)-mediated, PSGL-1-independent rolling adhesion on P-selectin. *Biophysical Journal*, 79:694–706, 2000.
- [16] B. DAS, P.C. JOHNSON, and A.S. POPEL. Computational fluid dynamic studies of leukocyte adhesion effects on non-Newtonian blood flow through microvessels. *Biorheology*, 37:239–258, 2000.
- [17] D.P. GAVER, and S.M. KUTE. A theoretical model study of the influence of fluid stresses on a cell adhering to a microchannel wall. *Biophysical Journal*, 75:721–733, 1998.
- [18] O. J. McCARTY, N. TIEN, B. S. BOCHNER, and K. KONSTANTOPOULOS. Exogenous eosinophil activation converts PSGL-1-dependent binding to CD18-dependent stable adhesion to platelets in shear flow. *Am. J. Physiol. Cell Physiol*, 284:C1223–1234, 2003.
- [19] T.N. THOMPSON, P.L.L. CELLE, and G.R. COKELET. Perturbation of red cell flow in small tubes by white blood cells. *Pflugers Arch.*, 413:372–77, 1989.
- [20] R.E. BRUEHL, T.A. SPRINGER, and D.F. BAINTON. Quantization of L-selectin distribution on human leukocyte microvilli by immunogold labeling and electron microscopy. *Journal of Histochem Cytochem*, 44:835–44, 1996.
- [21] U.H. VON ADRIAN, S.R. HASSLEN, R.D. NELSON, S.L. ERLANDSEN, and E.C. BUTCHER. A central role for microvillus receptor presentation in leukocyte adhesion under flow. *Cell*, 82:989–99, 1995.
- [22] J.C. FIRRELL, and H.H. LIPOWSKY. Leukocyte margination and deformation in mesenteric venules of rat. *Am J. Physiol*, 256:1667–1674, 1989.
- [23] E.R. DAMIANO, J. WESTHEDIDER, A. TORZEN, K. Ley. Variation in the velocity, deformation, and adhesion energy density of leukocytes rolling within venules. *Circ. Res.*, 79:1122–30, 1996.

- [24] A.J. GOLDMAN, R.G. COX, and H. BRENNER. Slow viscous motion of a sphere parallel to a plane wall. 2. Couette flow. *Chem. Eng. Sci.*, 22:653–660, 1967.
- [25] D.A. HAMMER, and S.M. APTE. Simulation of cell rolling and adhesion on surfaces in shear flow: general results and analysis of selectin-mediated neutrophil adhesion. *Biophysical Journal*, 63:35–57, 1992.
- [26] K.C. CHANG and D.A. HAMMER. Adhesive Dynamics Simulations of Sialyl-Lewis^x/E-selectin-Mediated Rolling in a Cell-Free System. *Biophysical Journal*, 79:1891–1902, 2000.
- [27] K.C. CHANG, D.F.J. TEES, and D.A. HAMMER. The state diagram for cell adhesion under flow: leukocyte rolling and firm adhesion. *PNAS*, 97:11262–11267, 2000.
- [28] S. K. DODDI. Three-dimensional computational modeling and simulation of biological cells and capsules. PhD thesis. *Rutgers University*, 2008.
- [29] K.E. CAPUTO and D.A. HAMMER. Effect of Microvillus Deformability on Leukocyte Adhesion Explored Using Adhesive Dynamics Simulations. *Biophysical Journal*, 89:187–200, 2005.
- [30] C. DONG, and X. LEI. Biomechanics of cell rolling: shear flow, cell-surface adhesion, and cell deformability. *J. Biomech. Eng.*, 33:35–43, 2000.
- [31] X. LEI, M.B. LAWRENCE, and C. DONG. Influence of cell deformation on leukocyte rolling adhesion in shear flow. *J. Biomech. Eng.*, 121:634–664, 1999.
- [32] N.A. N DRI, W. SHYY, and R. TRAN-SON-TAY. Computational modeling of cell adhesion and movement using a continuum-kinetics approach. *Biophysical Journal*, 85:2273–2286, 2003.
- [33] D.B. KHISMATULLIN, and G.A. TRUSKEY. Three-dimensional numerical simulation of receptor-mediated leukocyte adhesion to surfaces: Effects of cell deformability and viscoelasticity. *Phys. of Fluids*, 17:031505, 2005.
- [34] D.B. KHISMATULLIN, and G.A. TRUSKEY. A 3D numerical study of the effect of channel height on leukocyte deformation and adhesion in parallel-plate flow chambers. *Microvasc. Res.*, 68:188–202, 2004.
- [35] S. JADHAV, C.D. EGGLETON, and K. KONSTANTOPOULOS. A 3-D Computational Model Predicts that Cell Deformation Affects Selectin-Mediated Leukocyte Rolling. *Biophysical Journal*, 88:96–104, 2005.
- [36] C.D. EGGLETON, and A.S. POPEL. Large deformation of red blood cell ghosts in simple shear flow. *Physics of Fluids*, 10:1834–1845, 1998.

- [37] C.S. PESKIN, and McQUEEN. A 3-dimensional computational method for blood-flow in the heart. 1. Immersed elastic fibers in a viscous incompressible fluid. *Journal of Computational Physics*, 81:372–405, 1989.
- [38] TRYGGVASON, B. BUNNER, A. ESMAEELI, N. AL-RAWAHI, W. TAUBER, J. HAN, S. NAS, and Y. JAN. A Front Tracking Method for the Computations of Multiphase Flow. *Journal of Computational Physics*, 169:708–759, 2001.
- [39] S.O. UNVERDI, and G. TRYGGVASON. A Front-tracking Method for viscous, incompressible multi-fluid flows. *Journal of Computational Physics*, 100:25–37, 1992.
- [40] R. MITTAL and G. IACCARINO. Immersed Boundary Methods. *Annual Review of Fluid Mechanics*, 37:239–261, 2005.
- [41] C. DONG, and R. SKALAK. Leukocyte deformability: finite element modeling of large viscoelastic deformation. *Journal of Theoretical Biology*, 158:173–193, 1992.
- [42] C.DONG, R. SKALAK, K.L. SUNG, G.W. SCHMID-SCHONBEIN, and S. CHEIN. Passive deformation analysis of human leukocytes. *Journal of Biomech. Eng.*, 110:27–36, 1988.
- [43] J.M. CHARRIER, S. SHRIVASTAVA, and R. WU. Free and constrained inflation of elastic membranes in relation to thermoforming-non-axisymmetric problems. *Journal of Strain Analysis*, a24:55–74, 1989.
- [44] S. SHRIVASTAVA, and J. TANG. Finite element analysis of non-linear viscoelastic membranes with reference to thermoforming. *Journal of Strain Analysis*, 28:31–35, 1993.
- [45] M. DEMBO. On peeling an adherent cell from a surface,” Lectures on Mathematics in the Life Sciences. *Some Mathematical Problems in Biology*, 26:51–77, 1994.
- [46] P. BAGCHI, and S. BALACHANDAR. Steady planar straining flow past a rigid sphere at moderate Reynolds numbers. *Journal of Fluid Mechanics*, 466:365–407, 2002.
- [47] S. RAMANUJAN, and C. POZRIKIDIS. Deformation of liquid capsules enclosed by elastic membranes in simple shear flow: large deformations and the effect of fluid viscosities. *Journal of Fluid Mechanics*, 361:117–143, 1998.
- [48] J. HAPPEL, and H. BRENNER. Low Reynolds Number Hydrodynamics: With special applications to particulate media (mechanics of fluids and transport processes). Published by Springer, 1983.

- [49] V. RAMACHANDRAN, M. WILLIAMS, T. YAGO, D.W. SCHMIDTKE, and R.P. McEVER. Dynamic alterations of membrane tethers stabilize leukocyte rolling on P-selectin. *PNAS*, 101:13519–13524, 2004.
- [50] S.D. HOUSE, and H.H. LIPOWSKY. Leukocyte-endothelium adhesion: microhemodynamics in mesentery of the cat. *Microvasc. Res.*, 34:361–379, 1987.
- [51] D.W. SCHMIDTKE, and S.L. DIAMOND. Direct observation of membrane tethers formed during neutrophil attachment to platelets or P-selectin under physiological flow. *Journal of Cell Biol.*, 149:721–729, 2000.
- [52] Y. ZHAO, S. CHEIN, R. SKALAK, and H.H. LIPOWSKY. Leukocyte rolling in rat mesentery venules: distribution of adhesion bonds and the effects of cytoactive agents. *Ann. Biomed. Eng.*, 29:360–372, 2001.
- [53] J.Y. SHAO, H.P. TING-BEALL, and R.M. HOCHMUTH. Static and dynamic lengths of neutrophil microvilli. *PNAS*, 95:6797–6802, 1998.
- [54] Y. YU, and J.Y. SHAO. Simultaneous tether extraction contributes to neutrophil rolling stabilization: a model study. *Biophysical Journal*, 92:418–429, 2007.
- [55] G.I. BELL. Models for the specific adhesion of cells to cells. *Science*, 200:618–627, 1978.
- [56] R. ALON, S. CHEN, K. PURI, E.B. FINGER, and T.A. SPRINGER. The kinetics of L-selectin tethers and the mechanics of selectin-mediated rolling. *Journal of Cell Biol.*, 138:1169–1180, 1997.
- [57] U.S. SCWARZ, and R. ALON. L-selectin-mediated leukocyte tethering in shear flow is controlled by multiple contacts and cytoskeletal anchorage facilitating fast rebinding events. *PNAS*, 101:6940–6945, 2004.
- [58] B.T. MARSHALL, K.K. SARANGAPANI, J. WU, M. B. LAWRENCE, R.P. McEVER, and C. ZHU. Measuring molecular elasticity by atomic force microscope cantilever fluctuations. *Biophysical Journal*, 90:681–692, 2006.
- [59] E.F. KRASIK, and D.A. HAMMER. A semianalytic model of leukocyte rolling. *Biophysical Journal*, 87:2919–2930, 2004.
- [60] K.B. ABBITT, and G.B. NASH. Rheological properties of the blood influencing selectin-mediated adhesion of flowing leukocytes. *Am. J. Physiol. Heart Circ. Physiol.*, 285:H229–H240, 2003.
- [61] D. BARTHES-BIESEL. Motion of a spherical microcapsule freely suspended in a linear shear flow. *Journal of Fluid Mechanics* 100:831–853, 1980.

- [62] S.K. BHATIA, M.R. KING, and D.A. HAMMER. The state diagram for cell adhesion mediated by two receptors. *Biophysical Journal*, 84:2671–2690, 2003.
- [63] S.B. BROOKS, and A. TOZEREN. Flow past an array of cells that are adherent to the bottom plate of a flow channel. *Computers and Fluids*, 25:741–757, 1996.
- [64] K.E. CAPUTO, D. LEE, M.R. KING, and D.A. HAMMER. Adhesive dynamics simulations of the shear threshold effect for leukocytes. *Biophysical Journal*, 92:787–797, 2007.
- [65] K.S. CHANG, and W.L. OLBRICHT. Experimental studies of the deformation of a synthetic capsule in extensional flow. *Journal of Fluid Mechanics*, 250:587–608, 1993.
- [66] S. K. DODDI, and P. BAGCHI. Lateral migration of a capsule in a plane Poiseuille flow in a channel. *Int. J. Multiphase Flow*, in press, 2008.
- [67] G.B. CHAPMAN, and G.R. COKELET. Model studies of leukocyte-endothelium-blood interactions. I. The fluid flow drag force on the adherent leukocyte. *Biorheology*, 33:119-138, 1996.
- [68] G.B. CHAPMAN, and G.R. COKELET. Model studies of leukocyte-endothelium-blood interactions. II. Hemodynamic impact of leukocytes adherent to the wall of post-capillary vessels. *Biorheology*, 34:37-56, 1997.
- [69] G.B. CHAPMAN, and G.R. COKELET. Flow resistance and drag forces due to multiple adherent leukocytes in postcapillary vessels. *Biophysical Journal*, 74:3292–3301, 1998.
- [70] M. DEMBO, D.C. TORNEY, K. SAXMAN, and D.A. HAMMER. The reaction-limited kinetics of membrane-to-surface adhesion and detachment. *Proc. R. Soc. London*, 234:55–83, 1988.
- [71] P.S. FRENETTE. Sick cell vasoocclusion: heterotypic, multicellular aggregations driven by leukocyte adhesion. *Microcirculation*, 11:167-177, 2004.
- [72] Q. JIN, C. VERDIER, P. SINGH, N. AUBURY, R. CHOTARD-GHODSNIA, and A. DUPERRAY. Migration and deformation of leukocytes in pressure driven flows. *Mech. Res. Comm.*, 34:411-422, 2007
- [73] H.C. KAN, H.S. UDAYKUMAR, W. SHYY, and R. TRAN-SON-TAY. Hydrodynamics of a compound drop with application to leukocyte modeling. *Physics of Fluids*, 10:760–773, 1998.
- [74] M.R. KING, D. BANSAL, M.B. KIM, and I.H. SARELIUS. The effect of hematocrit and leukocyte adherence on flow direction in the microcirculation. *Annals Biomedical Engg*, 32:803–814, 2004.

- [75] M.R. KING, and D.A. HAMMER. Multiparticle adhesive dynamics: hydrodynamic recruitment of rolling leukocytes. *em PNAS*, 98:14919-12924, 2001.
- [76] M.R. KING, and D.A. HAMMER. Hydrodynamic recruitment of rolling leukocytes in vitro. *Biophysical Journal*, 84:4182-4193, 2003.
- [77] M.R. KING, V. HEINRICH, E. EVANS, and D.A. HAMMER. Nano-to-micro scale dynamics of P-selectin detachment from leukocyte interfaces. III. Numerical simulation of tethering under flow. *Biophysical Journal*, 88:1676-1683, 2005.
- [78] M.R. KING, M.B. KIM, I.H. SARELIUS, and D.A. HAMMER. Hydrodynamic interactions between rolling leukocytes in vivo. *Microcirculation*, 10:401-409, 2003.
- [79] E.J. KUNKEL, J.E. THOMAS, and K. LEY. Role of primary and secondary capture for leukocyte accumulation in vivo. *Circulation Research*, 82:30–38, 1998.
- [80] L.L. MUNN, R.J. MELDER, and R.K. JAIN. Role of erythrocytes in leukocyte-endothelial interactions: mathematical modeling and experimental validation. *Biophysical Journal*, 71:466–478, 1996.
- [81] J.B. FREUND. Leukocyte margination in a model microvessel. *Physics of Fluids*, 19:23301, 2007.